Technical University of Munich
School of Engineering and Design
Deutsches Geodätisches Forschungsinstitut (DGFI-TUM)
Prof. Dr.-Ing. habil. Florian Seitz

Transformation of global Thermospheric Density grids generated from the NRLMSISE-00 Model into a Multi-dimensional B-spline Representation

Liu, Shuxian

Master's Thesis

Study Program: Geodesy and Geoinformation

Supervisors: Prof. Dr.-Ing. habil. Michael Schmidt
Deutsches Geodätisches Forschungsinstitut (DGFI-TUM)
Technical University of Munich

M.Sc. Julian Zeitlhöfler
Deutsches Geodätisches Forschungsinstitut (DGFI-TUM)
Technical University of Munich

11/10/2022

Declaration of Authorship

I confirm that this Master's thesis is my own work and I have documented all sources and material used.

This thesis was not previously presented to another examination board and has not been published.

_____ _____

Place and date Signature

Abstract

The knowledge of the thermospheric density is of great importance to determine the air drag acceleration perturbing on the Low-Earth Orbiting (LEO) satellites. Generally, the thermospheric density is computed from the empirical thermosphere models such as the NRLMSISE-00 model which, however, has limited accuracy. In order to improve the empirical model and further improve the accuracy of Precise Orbit Determination (POD) of LEO satellites, new observations from geodetic techniques such as Satellite Laser Ranging (SLR) can be incorporated to perform the numerical integration of the satellite orbit. In this study, the empirical NRLMSISE-00 model is transformed into B-spline representations which allow the data incorporation within the context of 2-D, 3-D, and 4-D. The resolutions in different dimensions are $2.5^\circ \times 5^\circ$ in latitude and longitude, 20 km in height, and 5 min in time. Exclusively the trigonometric B-splines are deployed in the longitudinal direction in the global modeling, the endpoint-interpolating polynomial B-splines are applied to model the thermospheric density in latitude, height, and time in the global modeling, and all dimensions in the regional modeling. In the case of global modeling, the resolution levels are chosen as $J_1 = 4$ dependent on latitude, $J_2 = 3$ dependent on longitude, and $J_3 = 4$ dependent on height.

The modeling result shows, the relative difference of 10^{-3} for the estimated neutral densities are acquired in 2-D and 3-D representation. But the 3-D B-spline transformation outperforms the 2-D since the standard deviation (STD) values of 3-D modeling are smaller than those of 2-D modeling by a factor of 2. And the STDs of B-spline coefficients and the estimated neutral densities are latitude-dependent and height-dependent with values decreasing from the polar region to the equator and from lower altitudes to high altitudes but always with values of 4-order smaller than the original observations. With respect to the result of 4-D modeling, it performs much better than that of 2-D and 3-D modeling since only a small region is involved in the B-spline transformation.

In addition, one of the most important challenges in this study is the handling of height-dependent modeling due to its exponential decay in the vertical dimension, which is solved desirably, on one hand, by the serious choice of vertical sampling interval and the level of B-splines in height based on the pre-test of modeling the single vertical density profile, and on the other hand, by the introduction of the logarithmic model and appropriate weighting strategy dependent on the altitude.

Keywords: thermosphere; neutral density; NRLMSISE-00 model; B-spline representation; multi-dimensional modeling

Acknowledgements

First of all, I would like to give my heartfelt thanks to my supervisor, Professor Schmidt, for his kindness, illuminating guidance and profound knowledge. Working on a very busy schedule, he still gives my thesis careful reading and detailed comments. Without his keen insights and constant encouragement, it would not have been finished.

I also express my great appreciation to Julian Zeitlhöfler who has given me a lot of careful help in terms of data preparation, algorithm implementation, etc. His patience and research experience helped me develop many new ideas.

Finally, my cordial thanks also go to my family member and friends who love and care me and whom I love and care.

Contents

List of Figures

List of Tables

List of Algorithms

Acronyms

1 Introduction

1.1 Motivation

The Precise Orbit Determination (POD) of satellites is a fundamental prerequisite of a range of geo-scientific applications such as remote sensing, satellite gravity missions, and satellite altimetry. For example, the orbit with an accuracy of a few millimeters for Low-Earth Orbiting (LEO) satellites is essential for the accurate monitoring of the sea level change; the determination of the precise position of Global Navigation Satellite System (GNSS) satellites in space is a prerequisite for achieving Precise Point Positioning (PPP). In POD of a satellite, the different kinds of perturbations acting on it need to be represented or/and modeled as well as possible in order to compute the satellite's position in the force fields.

However, even today, it is still a great challenge to model the non-gravitational acceleration acting on the satellites, which comprises within the equation of motion of the satellite the direct radiation pressure, the pressure due to Earth's albedo and infrared radiation, drag-like parts due to the thermospheric drag and the solar wind pressure as well as other effects. For satellites at high altitudes like the GNSS satellites, the direct solar radiation pressure is the major non-gravitational effect. For LEO satellites below 1000 km, however, the atmospheric drag mainly depending on the thermospheric density is the largest non-gravitational perturbation [Walker, 1987] and thus, a major problem in the POD of these satellites. Consequently, the knowledge and study of the thermospheric density are of crucial importance for the POD of LEO satellites.

The thermosphere is a layer of the Earth's atmosphere that is directly above the mesosphere and below the exosphere (Fig. 1.1). It extends from about 90 km to between 500 and 1000 km above the Earth's surface. Normally, thermospheric densities at LEO satellite positions are calculated by empirical atmosphere models such as the Jacchia-Bowman 2008 (JB2008) model [Bowman et al., 2008], the COSPAR International Reference Atmosphere 1986 (CIRA86) model [Fleming et al., 1990], Naval Research Laboratory Mass Spectrometer Incoherent Scatter Radar Extended 2000 (NRLMSISE-00) model [Picone et al., 2002] and the Drag Temperature Model 2013 (DTM2013) [Bruinsma, 2015] which are generally driven by globally defined space weather parameters such as the F10.7 index reflecting the solar activity. In this study, the NRLMSISE-00 model is selected to globally determine thermospheric densities, considering 1) its advantages in height coverage and the time span as well as the precision; and 2) the consistency of model usage in our "Development of High-precision Thermosphere Models for Improving Precise Orbit Determination of Low-Earth Orbiting Satellites (TIPOD)" project at DGFI-TUM, which is the framework of this study.

In fact, all the empirical atmosphere models have limited accuracy. However, today, the information from different geodetic observation techniques such as Satellite Laser Ranging (SLR) can be used to precisely determine the satellite orbits and thus, to improve neutral densities obtained from the empirical atmosphere models. SLR provides highly accurate travel time measurements of laser pulses reflected at laser retro-reflector arrays (RRA) mounted on the

satellite surface which has been emitted from telescopes on the Earth's surface [Panzetta et al., 2018]. Due to the high accuracy (how close a given set of observations are to their true value) and precision (how close the observations are to their mean value) of such measurements as well as its sensitivity to the perturbation acceleration acting on the satellite, it is highly appropriate in further investigations to use SLR observations to improve empirical thermosphere models and further to improve the precision of satellite orbits. For the improvement of empirical thermosphere models, our approach in the TIPOD project, i.e. combining the background information from the empirical thermosphere model and the measurements from geodetic observing techniques, is generally based on a fully dynamic POD of the selected spherical satellites using the DGFI Orbit and Geodetic parameter estimation Software (DOGS) [Bloßfeld, 2015].

Basically, the empirical NRLMSISE-00 model can be evaluated at any spatial point and at any time moment. Hence, the evenly or unevenly distributed grids representing thermospheric densities can be derived from the thermosphere model, which is rather intuitive and readable. In the next step, different procedures can be applied such as data assimilation or transforming the model into another representation which allows to incorporate new observations from SLR in order to improve the empirical thermosphere model. One option for such a model transformation is the application of a statistical approach, e.g., the Principal Component Analysis (PCA) to the model under investigation, i.e., NRLMSISE-00. An alternative is the representation of the model in form of a purely mathematical approach, e.g., a multi-dimensional B-spline model [Schmidt et al., 2015]. Between these, the latter approach transforms the empirical atmosphere model into a set of B-spline coefficients which largely saves storage and is convenient to transmit. Additionally, it allows for the optimal handling of heterogeneously distributed observations and data gaps. On the other hand, B-spline modeling has never been applied to thermospheric densities even if it already has many applications with good achievements in ionosphere-related research [Zeilhofer, 2008; Goss et al., 2019; Zeitler et al., 2021], hence, it is significantly meaningful and valuable to investigate and apply the B-spline approach under the circumstance of thermosphere considering the different characteristics of ionosphere and thermosphere in terms of density magnitudes and density distribution in particular in height dependency. As a subpart in the framework of the TIPOD project, the work in this study is significant to providing highly precise multi-dimensional B-spline models of the thermosphere, and more accurate thermospheric density data at the satellite's orbit followed by better improvement for the empirical thermosphere model, as a consequence, the more precise orbit for the satellite is more likely to be determined.

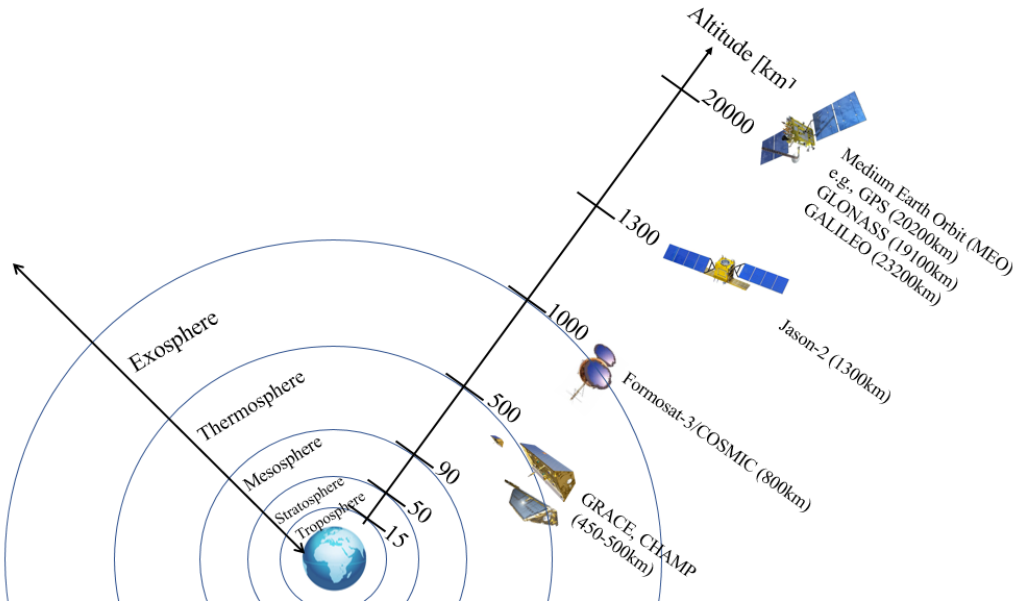

Figure 1.1: The atmosphere structure

1.2 State of the art

In the past, various thermosphere models have been developed with output parameters comprising density and temperature by taking into account the complex interactions between the atmosphere and the solar as well as the geomagnetic activity. In general, thermosphere models can be categorized into empirical and physical ones.

The first category is identified with empirical models based on long-term observations, which play several indispensable roles in atmospheric research, data analysis, specification, and prediction, particularly in upper atmospheric research. For example, there are the NRLMSISE-00 model [Picone et al., 2002] and its follow-up, the Naval Research Laboratory Mass Spectrometer Incoherent Scatter Radar (NRLMSIS) 2.0 model [Emmert et al., 2021], the JB2008 model [Bowman et al., 2008], the DTM2013 model [Bruinsma, 2015], and the CH-Therm2018 model [Xiong et al., 2018]. Generally, the empirical models provide a condensed representation of the historical record of observations and thereby serve as benchmarks for testing new observations and techniques. For over a decade, the Mass Spectrometer Incoherent Scatter Radar (MSIS)-class models describe the atmospheric composition, total mass density, and temperature. The acronym MSIS derives from the space-based mass spectrometer and ground-based Incoherent Scatter Radar (ISR) measurements on which the model was originally based [Emmert et al., 2021]. In this class, the first developed MSIS-86 [Hedin, 1987] model ranges upward from 90 km, followed by Mass Spectrometer Incoherent Scatter Radar Extended (MSISE)-90 [Hedin, 1991] extending from the ground to the exobase; and the NRLMSISE-00 empirical model retains the calling sequence and arguments of MSISE-90 and earlier MSIS models, which is a major upgrade of the MSISE-90 model in the thermosphere. This release was focused primarily on the thermosphere and included the assimilation of new middle thermosphere O_2 data, more recent ISR measurements, mass density data derived from satellite orbit decay, and the introduction of an anomalous oxygen component that accounts for additional mass in the upper thermosphere attributed to a hot population of atomic oxygen and atomic oxygen ions. The latest NRLMSIS 2.0 assimilates extensive new (since 2000) measurements and can be regarded as a whole-atmosphere empirical model. For

Jacchia-Bowman (JB)-class, JB2008 model is developed as an improved revision to the JB 2006 model which is based on Jacchia's diffusion equations. The DTM2013 is a semi-empirical model describing the temperature, density, and composition of the Earth's thermosphere. The CH-Therm-2018 model of the thermospheric mass density is derived from 9-year (from August 2000 to July 2009) accelerometer measurements from the CHAllenging Mini-satellite Payload (CHAMP) satellite at altitudes from 460 to 310 km. In conclusion, for calculating total mass density, the NRLMSISE-00 model is comparable to or even better than the JB-class models since numerous orbital drag and accelerometer data sets have been included in generating the model [Picone et al., 2002].

The other type of model is the physical model which fundamentally considers the physical coupling processes between the neutral thermosphere and the charged ionosphere. An example is the Thermosphere-Ionosphere-Electrodynamics General Circulation Model (TIE-GCM) developed by the National Center of Atmospheric Research (NCAR). It provides a comprehensive, three-dimensional (3-D), non-linear representation of the coupled thermosphere and ionosphere system [Qian et al., 2014].

In addition to the development of thermosphere models which are based on slightly different input data sets and thus, may lead to rather different results, there are many studies focusing on the comparison or the improvement of empirical thermosphere models with external geodetic measurements. Doornbos et al. [2007] used the Doppler Orbitography by Radiopositioning Integrated on Satellite (DORIS), SLR and radar altimeter data of the European Remote Sensing Satellite (ERS)-2 and Envisat to evaluate the performance of density model calibration. A reduction from 23.5% to 17.1% Root Mean Square (RMS) error was found by analyzing estimated density scale factors after adjusting the NRLMSISE-00 model using 10 parameters per day, which means these scale factors allow the reduction of long-period density model errors using tracking data. Flanagan [2015] determined the air drag coefficients of the Atmospheric Neutral Density Experiment (ANDE)-2 satellites over their life spans by using SLR data of the ANDE-2 satellites in union with gas-surface interaction equations. These drag coefficients are then used to determine the atmospheric densities experienced by these satellites over various days so that inaccuracies in the atmospheric models can be observed. Panzetta et al. [2018] tested four thermospheric models, namely CIRA86, NRLMSISE-00, JB2008 and DTM2013 by performing POD of a spherical satellite called ANDE-Pollux over a period of 49 days using SLR observations to this satellite by estimating scale factors of density values from these models. As a consequence, information on the discrepancies between the various models and the true density can be derived from SLR measurements. Rudenko et al. [2018] used SLR observations to two ANDE-2 satellites, that is ANDE-Castor and ANDE-Pollux, as well as Special Purpose INexpensive Satellite (SpinSat) with altitudes between 248 km and 425 km to calibrate the CH-Therm-2018 model, as well as four other empirical models of thermospheric density, namely namely CIRA86, NRLMSISE-00, JB2008 and DTM2013. Zeitler et al. [2021] brought together thermospheric density corrections for the NRLMSISE-00 model in terms of scale factors derived from SLR and accelerometer measurements. From their comparison, a rather similar behavior with correlations of up to 80% was noticed.

However, the representation of neutral densities with B-splines is totally new for the thermosphere, although B-spline modeling has been applied to the ionosphere at DGFI-TUM for a long period: Schmidt et al. [2011] presented an approach for modeling Vertical Total Electron Content (VTEC) generally depending on space and time defining the 3-D system of base functions as tensor products of trigonometric B-spline functions for the longitude and two sets of endpoint-interpolating B-spline functions for latitude and time, respectively. And they also compared this approach to a spherical harmonic expansion with similar resolution and show

how data gaps influence the accuracy of VTEC maps even in areas with good data coverage. Schmidt et al. [2015] gave a detailed overview of the mathematical modeling of ionospheric parameters such as the electron density by means of B-spline expansions. In Goss et al. [2020], a two-step model (TSM) is introduced comprising a global model as the first step and a regional model as the second step. The TSM provides both, a global and a regional VTEC map at the same time.

The B-spline technique is developed extremely robust, however, due to the exponential decay of thermospheric densities with increasing height, it is a challenging task to model neutral densities dependent on height as accurately as possible. Consequently, the handle of height-dependent modeling for thermospheric density using B-spline expansions is a critical topic, also a valuable study direction in the future.

1.3 Goals and contributions

In this study, the B-spline representation is applied first to the thermospheric densities computed globally from the NRLMSISE-00 model on a spatial grid at defined time moments. Afterwards, two-dimensional (2-D) models depending on latitude and longitude at given discrete heights and time moments are generated. In the next step, these models are extended to a 3-D representation depending on latitude, longitude, and height. Finally, this approach is generalized to a four-dimensional (4-D) model representing the thermospheric density in latitude, longitude, height, and time. Additionally, the empirical model NRLMSISE-00 is transformed with respect to the thermospheric density into a multi-dimensional B-spline model within a period of varying solar activity, e.g., within a year in which at least one major solar event took place.

Therefore, the global neutral density data from 23/11/2014 to 14/03/2016 covering 64 GPS weeks (called "64 GPS-week data") generated from the NRLMSISE-00 model is used to investigate the variation of thermospheric densities, which contains St. Patrick's storm day on 17 March 2015. Moreover, two small datasets are selected in order to perform the B-spline modeling of thermospheric densities, which are 23/11/2014 - 30/11/2014, and 15/03/2015 - 22/03/2015, called the "quiet period" and the "storm period", respectively. In addition, the B-spline modeling results are evaluated and analyzed in terms of the modeling differences to the model-derived "true" neutral densities, modeling precision, and computational time. The specific contents are as follows:

(1) The supporting theoretical background in the framework of the TIPOD project, including the equation of motion of satellites, the principle for the improvement of empirical thermosphere models, the brief introduction of SLR technique and POD software DOGS, as well as the description of NRLMSISE-00 model.

(2) The pre-analysis of so-called "64 GPS-week data" used in this study by means of Continuous Fourier Transform (CFT), in particular the spectral content of empirical NRLMSISE-00 model.

(3) The principles of B-spline expansions to model thermospheric densities with the use of polynomial B-spline and trigonometric B-spline basis functions in one-dimensional (1-D), 2-D, 3-D, and 4-D cases.

(4) The introduction of the experiment including data characteristics, experiment procedures, and evaluation approaches.

(5) The analysis and discussion of the modeling result.

1.4 Outline of the thesis

According to the study contents explained above, there are in total 7 chapters in this thesis: Chapter 1 firstly gives the introduction of the research background and significance, as well as the description of various thermosphere models and empirical thermosphere model-based studies, from which the modeling approach used in this study is introduced. In Chapter 2, the theoretical background in the framework project TIPOD is described and explained mainly including the perturbations acting on LEO satellites and the use of SLR measurements. Chapter 3 describes the drivers of the NRLMSISE-00 model to compute thermospheric densities in detail, and the procedures of data acquisition and preparation, as well as the results of data pre-analysis by means of CFT. In Chapter 4, it explains the generation and characteristics of two kinds of 1-D B-spline basis functions - polynomial and trigonometric B-splines, which can be extended to higher-dimensional modeling in similar ways. Chapter 5 gives the experiment implementation including algorithm test and real data modeling parts, and the evaluation approach is provided in order to assess the accuracy and reliability of modeling results. And the experiment results and relative discussion are presented and analyzed in Chapter 6, followed by the summary and outlook of this thesis in the final Chapter 7.

2 Project background

2.1 Theoretical background

The equation of motion of a satellite refers to its total acceleration or the second derivative of the satellite's position vector $\mathbf{r}_{sat}(t)$ with respect to time t, that is,

$$\frac{d^2\mathbf{r}_{sat}(t)}{dt^2} = \mathbf{a}_{sat} = \mathbf{a}_G + \mathbf{a}_{NG}, \tag{2.1}$$

where the total acceleration of the satellite $\mathbf{a}_{sat}$ is expressed as the sum of the gravitational acceleration $\mathbf{a}_G$ and the non-gravitational acceleration $\mathbf{a}_{NG}$.

In the satellite orbit determination, the assessment of the non-gravitational perturbations is one of the major problems since they are caused by the interactions between the satellite surface and its environment which depends on the specific physical parameters of the satellites. Specifically, $\mathbf{a}_{NG}$ consists of the acceleration caused by solar radiation pressure (SRP) $\mathbf{a}_{srp}$, the acceleration caused by Earth radiation pressure (ERP) $\mathbf{a}_{erp}$, the aerodynamics acceleration $\mathbf{a}_{aero}$ due to the atmosphere and other acceleration effects $\mathbf{a}_{others}$, such as the radiation pressure of the Moon [Doornbos, 2012], satellite thermal emission:

$$\mathbf{a}_{NG} = \mathbf{a}_{srp} + \mathbf{a}_{erp} + \mathbf{a}_{aero} + \mathbf{a}_{others}. \tag{2.2}$$

Amongst these non-gravitational perturbations, the aerodynamic acceleration is the largest one for LEO satellites with altitudes lower than 1000 km which is around the maximum height of the thermosphere, thus, the aerodynamic perturbations represent the main error source within a LEO satellite POD. The aerodynamic acceleration is expressed as

$$\mathbf{a}_{aero} = \frac{1}{2}\,\frac{A_{ref}}{m}\,\mathbf{c}_{aero}\,\rho_M\,{v_{rel}}^2 \tag{2.3}$$

where A_{ref} is the effective cross-sectional area of the satellite interacting with the atmosphere, m is the satellite mass, $\mathbf{c}_{aero}$ denotes the dimensionless aerodynamic coefficient vector depending on the geometry and orientation of the satellite, ρ_M is the thermospheric neutral density, and v_{rel}=$|\mathbf{v}_{rel}|$ represents the velocity of the satellite relative to the atmosphere [Doornbos, 2012]. The relative velocity vector $\mathbf{v}_{rel}$ reads as the sum

$$\mathbf{v}_{rel} = \mathbf{v}_{r,i} + \mathbf{v}_{r,c} + \mathbf{v}_{r,w} \tag{2.4}$$

of the inertial velocity vector $\mathbf{v}_{r,i}$ of the satellite along the orbit, the velocity vector $\mathbf{v}_{r,c}$ caused by the rotation of the atmosphere and the velocity vector $\mathbf{v}_{r,w}$ caused by winds in the atmosphere.

In the project TIPOD, SLR tracking measurements are used to implement the POD of LEO satellites in order to improve the calculated thermospheric density based from NRLMSISE-00.

The spherical LEO satellites are tracked by SLR. They are ideally affected only by one component of the total aerodynamic perturbation, that is, the atmospheric drag. The drag acceleration is always pointing in opposite direction to the relative velocity vector $\mathbf{v}_{rel}$ in Eq. (2.4) and leads to a deceleration of the satellite. Consequently, the spacecraft loses kinetic energy due to the atmosphere friction which results in a decrease of the semi-major axis (orbit decay) and the eccentricity (orbit becomes more circular) [Vallado, 2001]. For a perfectly spherical satellite, the other two components of the aerodynamic perturbation, namely the lift and the side acceleration, disappear because the normal of a sphere is always parallel to the drag direction. In general, the air drag acceleration is obtained from

$$\mathbf{a}_{drag} = \frac{1}{2}\,\frac{A_{ref}}{m}\,c_D\,\rho_M\,{v_{rel}}^2\,\mathbf{x}, \tag{2.5}$$

where c_D is the dimensionless aerodynamic drag coefficient describing the interaction of the atmosphere with the satellite surface, and the unit vector $\mathbf{x} = \mathbf{v}_{r,i}/\,|\mathbf{v}_{r,i}|$ is introduced representing the along-track component of the aerodynamic acceleration. In the literature, the term $\frac{A_{ref}}{m}c_D$ is called the satellite-specific ballistic coefficient.

2.2 Satellite Laser Ranging

With the information from SLR which is the most accurate technique to determine the geocentric position of LEO satellites among the modern space geodetic techniques since it provides instantaneous sub-cm level measurements of the satellite range from the observation telescope on the Earth surface [Panzetta et al., 2018], the observation equation of one-way range measurement ρ together with its error e_ρ is formulated as

$$\rho + e_\rho = ||\mathbf{r}_{sat}(t_M + \Delta t) - \mathbf{r}_{sta}(t_M + \Delta t)|\,| + \Delta\rho, \tag{2.6}$$

where on the right-hand side only the geometrical distance ρ between the retro-reflector on the satellite and the observation telescope is expressed and all the remaining corrections are contained in the term $\Delta\rho$ [Bloßfeld, 2015]. In Eq. (2.6), $\mathbf{r}_{sat}$ is the position vector of the satellite's Center of Mass (CoM) in the Geocentric Celestial Reference System (GCRS), $\mathbf{r}_{sta}$ is the position vector of the station converted from the International Terrestrial Reference System (ITRS) to GCRS using Earth orientation parameters, t_M means the time epoch of reflection of the laser pulse at the satellite, and Δt means the time bias of the measurement [Zeitler et al., 2021].

Since we want to improve the thermospheric neutral density, a scale factor is introduced [Panzetta et al., 2018; Rudenko et al., 2018; Zeitler et al., 2021]. Therefore, Eq. (2.5) is extended by the time-dependent scale factor $f_{s,SLR} = f_{s,SLR}(t)$, such that the modified drag acceleration is expressed as

$$\mathbf{a}_{drag} = \frac{1}{2}\,f_{s,SLR}\,\frac{A_{ref}}{m}\,c_D\,\rho_M\,{v_{rel}}^2\,\mathbf{x}. \tag{2.7}$$

In general, for LEO satellites with the spherical shape which are much frequently used in SLR, we can assume that the quantities A_{ref}, m, c_D and v_{rel} have been determined precisely, the scale factor $f_{s,SLR}$ thus can be interpreted as a pure scaling of the thermospheric density ρ_M generated by the empirical thermosphere model [Zeitler et al., 2021]. Under such cases, the scale factors in time dependency, also the estimated thermospheric densities having absorbed the scaling can be generated through performing the POD of LEO satellites using SLR measurements.

2.3 DGFI Orbit and Geodetic Parameter Estimation Software

At DGFI-TUM, the POD of satellites is performed by the DGFI Orbit and Geodetic Parameter Estimation Software - DOGS [Bloßfeld, 2015] which is used to process geodetic observations like SLR, DORIS, and Very Long Baseline Interferometry (VLBI) as well as their combination at various levels of the Gauss-Markov model. The orbit computation (OC) component of DOGS enables four modi, such as (1) orbit computation, (2) simulation of observations, (3) generation of normal equations, and (4) parameter correction. In the TIPOD project, the last modus is used where the numerical integration of a satellite orbit is performed together with adjusting a set of model parameters to the SLR observations applying an iterative least squares estimation.

Numerical integration is applied for orbit determination for the solution of the equations of motion as shown in Eq. (2.1) and of the variational equations. This requires on one hand the knowledge of all acting forces on the satellite with the same accuracy level and on the other hand numerical stability of the orbit integration. The mathematical realization of the numerical integration using Cowell or Encke method [Brouwer, 1937] can be done by various methods. Generally, polynomials are approximated to a time series of sample values. Then arbitrary orbit points can be interpolated or extrapolated. A commonly well-known single-step approach is the Runge-Kutta method [Butcher, 1996]. Here a Taylor series with a specific order is used as extrapolation function. A special attribute of single-step methods is that only the last integration step is used for extrapolation.

3 Thermospheric density computation

In our numerical investigations, we apply in the sequel the empirical thermosphere model NRLMSISE-00, which describes the neutral temperature and densities from the Earth's surface to the lower exosphere (0-1000 km). This model is the basis for computing thermospheric neutral densities in this study, which provides the thermospheric density grids used for applying B-spline transformation within the context of different dimensions.

3.1 Drivers of NRLMSISE-00 model

The model possesses an extensive underlying database covering several decades, it is therefore driven by various data sets such as accelerometer and orbit-derived density data, inferred temperature from incoherent scatter radar, ultraviolet (UV) occultation measurements, and globally defined space weather parameters such as solar radio flux at a wavelength of 10.7 cm (F10.7) and magnetic activity indices (Kp), as well as other parameters such as local time and position. Specifically, a variety of parameters are needed as inputs of computation functions with calculating the output variables listed in Table 3.1. At altitudes above 500 km, the contributions from "anomalous oxygen" are included to account for the contribution of non-thermospheric species to satellite drag at high altitudes and permit the user to compute both the "thermospheric mass density" (or total neutral mass density) provided by past generations of MSIS and an "effective" mass density, which denotes the sum of the thermospheric mass density and the anomalous oxygen contribution at altitudes near the exobase [Picone et al., 2002]. NRLMSISE-00 model takes statistical variability into account while interpolating, or extrapolating, the underlying data sets to estimate composition, temperature, and density for times, where geophysical conditions and locations are not covered by the database. Therefore, the NRLMSISE-00 model can be evaluated at any time and geographical position.

3.2 Thermospheric density grids

According to the routine of thermospheric density computation, the multi-dimensional thermospheric density data from NRLMSISE-00 model can be determined in the investigation period. Generally, the study of the empirical model NRLMSISE-00 is reasonable to include a period of varying solar activity, i.e, include high and low solar activity since the performance of the thermosphere model shall be observed as well during the solar event like the St. Patrick's storm day on 17 March 2015. As the first super geomagnetic storm of solar cycle 24 (2008-2019), the Disturbance Storm-Time (Dst) index of the St. Patrick's storm day is less than -200 categorized as the major (intense or great) storm [Wu et al., 2016], thus, the year 2015 is selected as the main investigated period in this study. More specifically, the neutral density dataset between 23/11/2014 - 14/03/2016 is computed and prepared which in total covers 64 full GPS weeks, thus, called "64 GPS-week data" in this thesis.

Table 3.1: Drivers of the empirical NRLMSISE-00 model

INPUTS	Description
IYD	YEAR AND DAY AS YYDDD
SEC	UT(SEC)
ALT	ALTITUDE(KM)
GLAT	GEODETIC LATITUDE(DEG)
GLONG	GEODETIC LONGITUDE(DEG)
STL	LOCAL APPARENT SOLAR TIME
F107A	81 day AVERAGE OF F10.7 FLUX (centered on day DDD)
F107	DAILY F10.7 FLUX FOR PREVIOUS DAY
AP	MAGNETIC INDEX(DAILY)
MASS	MASS NUMBER
D(1)	HE NUMBER DENSITY(CM-3)
D(2)	O NUMBER DENSITY(CM-3)
D(3)	N2 NUMBER DENSITY(CM-3)
D(4)	O2 NUMBER DENSITY(CM-3)
D(5)	AR NUMBER DENSITY(CM-3)
D(6)	TOTAL MASS DENSITY(GM/CM3)
D(7)	H NUMBER DENSITY(CM-3)
D(8)	N NUMBER DENSITY(CM-3)
D(9)	Anomalous oxygen NUMBER DENSITY(CM-3)
T(1)	EXOSPHERIC TEMPERATURE
T(2)	TEMPERATURE AT ALT

In the first step of data acquisition and preparation, the generated thermospheric densities from NRLMSISE-00 model shall have a dense temporal structure which is mainly determined by the characteristics of this study, that is, we are not able to define appropriate resolution in different dimensions before we investigate the spatio-temporal content of the NRLMSISE-00 model using the neutral densities computed based on it. Therefore, the relatively dense resolution in time like several minutes can provide adequate data to make a first impression on the estimated densities, also on the empirical thermosphere model. In this study, the thermospheric density data with the sampling interval of 5 min is firstly computed which can also be used to extract the data with other resolutions like 10 min, 30 min, etc.

For the spatial resolution of thermospheric density data, the homogeneous spacing in latitude and longitude is chosen very frequently in numerical modeling and investigations because it is easy to generate homogeneously distributed data from a model compared to the inhomogeneous data, and it is the best way for the numerical data to cover the global Earth. Therefore, a grid spacing of 2.5°x5° in latitude and longitude is used which is a common pair of sampling adopted in a grid-like global representation like ionosphere [Goss et al., 2019]. However, the determination of resolution in height dependency for the thermospheric densities needs to be seriously considering the exponential expansion of them as a function of altitude at a specific grid point. Similarly, the thermospheric density layers at each 5 m are generated in order to rebuild the exponential distribution as close as possible to the realistic profile, and also to guarantee an adequate test dataset. Additionally, with respect to the height range, the densities between 0 km and 1000 km are generated initially.

Figure 3.1 gives an exemplary graph that contains 9 subfigures presenting the spatial distribution of thermospheric densities derived from the NRLMSISE-00 model at different altitudes at one specific time moment. It can be seen that although the maps at different heights have similar global distributions except for the map at 200 km, their magnitudes differ significantly. In order to observe the decaying behavior of thermospheric densities along the height, Fig. 3.2 illustrates two density profiles at the (-30°, 0°) grid point corresponding to two epochs within the quiet period and within the storm period, respectively. Obviously, the exponential decaying can be found in the NRLMSISE-00 model which is consistent with the theoretical knowledge of the thermosphere. Moreover, two outputs of thermospheric density in Fig. 3.2 present different performances, in particular in the upper thermosphere, with faster decaying speed for the profile during the quiet period than that during the storm period. It proves that space weather activity has a visible influence on the thermospheric density.

Figures 3.1 and 3.2 leave an initial impression on the thermospheric densities from the empirical NRLMSISE-00 model. Firstly, the density profile as a function of altitude turns at around 200 km and decays slower than the density below 200 km. Besides, starting from 300 km to its upper, the global densities distribute differently compared to density maps below 300 km. By taking the impression above and the height range of the thermosphere as well as the orbit height of LEO satellites into account, the neutral densities between 300 and 1000 km are used for further B-spline transformation.

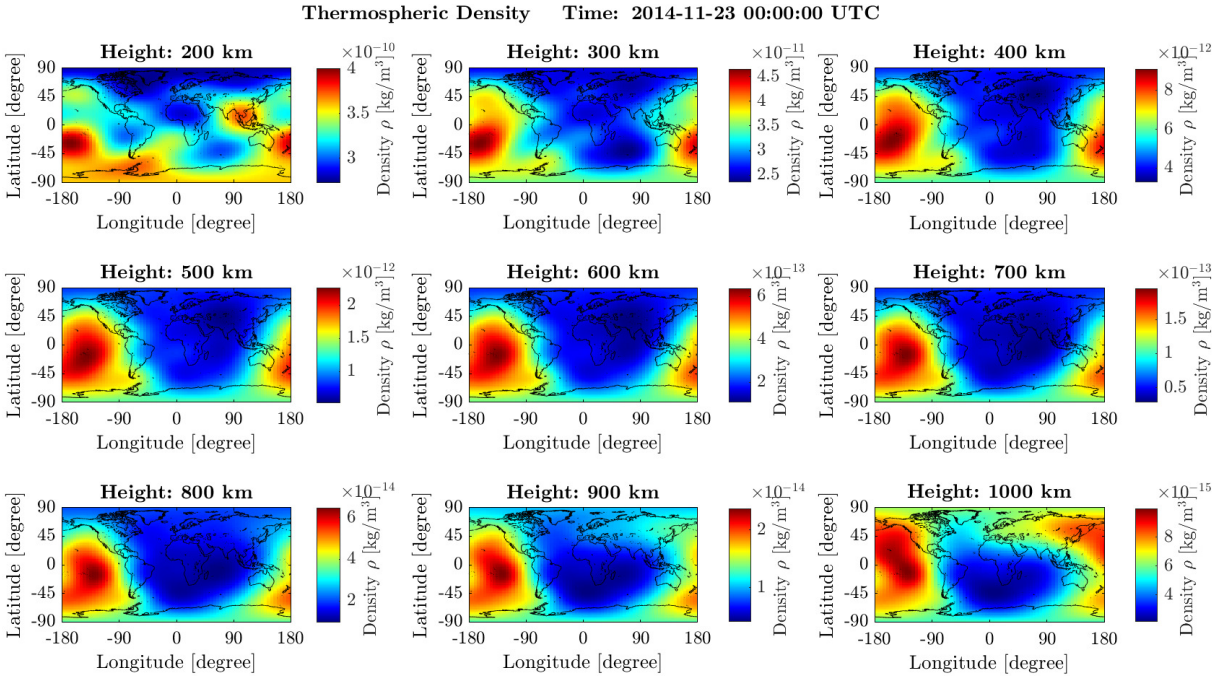

Figure 3.1: Thermospheric density maps at different altitudes with the resolution of 2.5°x5° in latitude and longitude derived from the NRLMSISE-00 model at the defined time moment.

3.3 Data pre-analysis

The pre-analysis of thermospheric density data is indispensable, in particular, the frequency content, prior to the B-spline transformation of multi-dimensional density grids. For analyzing the spectral contents contained in the NRLMSISE-00 thermosphere model, Fourier

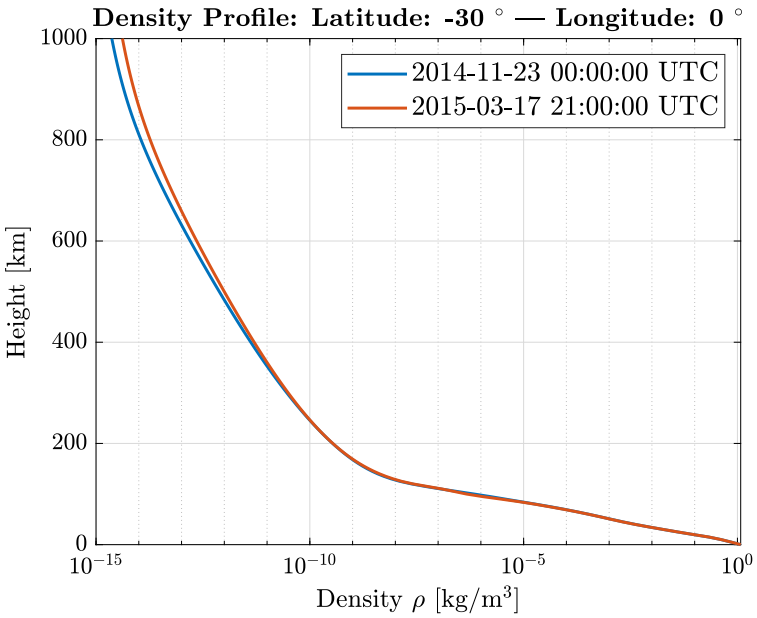

Figure 3.2: Exemplary sketch of thermospheric density from NRLMSISE-00 model as a function of altitude at one specific grid point with the resolution of 5m.

analysis is a powerful tool to transform the density signal from the time domain to the frequency domain. Considering CFT can help to generate spectral information of a signal at any reasonable assigned frequency, which is a distinguished advantage compared to Fast Fourier Transform (FFT), it is used to detect the distinct frequency information with the time series of thermospheric densities of a long period. In CFT Equation (3.1), $F(w)$ represents the Fourier Transform of the corresponding time-dependent function $f(t)$ as

$$F(w) = \int_{-\infty}^{+\infty} f(t)\, e^{-i2\pi wt}\, dt, \tag{3.1}$$

where w is the frequency one would like to investigate, t is the time, and $i = \sqrt{-1}$. This expression means that the signal along the entire time axis is needed for deriving the Fourier transform calculated at an individual frequency w.

Since a real signal is usually given within the finite time interval $t \in [t_1, t_2]$, the Eq. (3.1) can be written as

$$F(w) = \int_{t_1}^{t_2} f(t)\, e^{-i2\pi wt}\, dt. \tag{3.2}$$

Then the amplitude spectrum $A(w)$ can be derived from corresponding $F(w)$ through the formula

$$A(w) = \frac{2\sqrt{S_{ff}(w)}}{t_2 - t_1} = \frac{2\sqrt{F(w) \cdot F^*(w)}}{t_2 - t_1}. \tag{3.3}$$

with the same unit of the original signal $f(t)$. And S_{ff} denotes the Fourier spectrum.

With the method described above, Fig. 3.3 presents the time series of thermospheric density at 500 km in the study period and the corresponding amplitude spectrum derived by CFT. For the periods below one month to be investigated, the spacing of 10 min is adopted, while the interval of one day is selected for the period above one month. It can be observed in Fig.

3.4 that there are four regional peaks in the amplitude spectrum: 24 h, 12 h, 8 h, 6 h with amplitudes of 2.94e-13 kg/m^3, 6.06e-14 kg/m^3, 5.37e-15 kg/m^3, 9.40e-15 kg/m^3, respectively. The peak at 24 h is apparently caused by the day-night behavior, however, the appearance of the other three peaks at 12 h, 8 h, and 6 h is not concerning the physical reason. Generally, the real signal in nature does not perfectly conform to harmonic functions but is composed of a set of harmonic components. As a consequence, the frequency such as half-day, 1/3 day, and 1/4 day is probably detected by Fourier transform. Amongst the four peaks, the period of 24 h is dominating with the largest amplitude. The similar results appear in the time series at remaining attitudes as well, and it is worth mentioning that the amplitudes of one regional peak at different attitudes, e.g. 24 h, also apply to exponential decaying, which can be observed in Fig. 3.5.

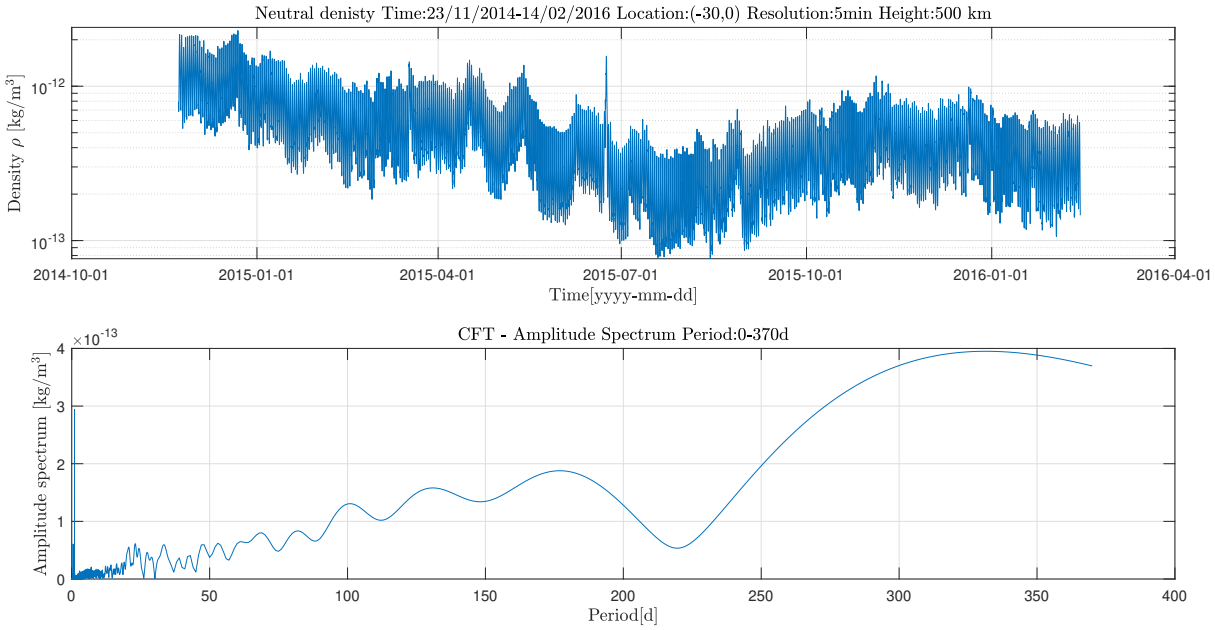

Figure 3.3: An example of amplitude spectrum derived by CFT (bottom) of the series of thermospheric density (top) in the investigation period.

However, in Fig. 3.3 a period around 340 d can be found which is not far from the annual period. It shows the variation of thermospheric densities containing the annual period, but it is not exactly 365 d in the investigation period. This is because this so-called "64 GPS-week data" only covers one complete annual period, which results in the desired annual period not being perfectly detected by CFT. This reason is proved by a small test: a periodical signal exclusively containing sine functions with 2 cycles in the assigned time domain is generated, which is transformed by CFT. As a result, the period with the highest amplitude in the frequency domain deviates from 2π which is the assigned basis period in the original test signal (see Fig. 3.6). However, the result is nearly 6.28 when the signal is repeated to 10 cycles (see Fig. 3.7). It means only 2 cycles are not enough to detect the basis frequency successfully. Similarly, for acquiring the peak at the annual period in the real neutral density series, longer-term data is required. As shown in Fig. 3.8 which illustrates a 15-year series of thermospheric density also at 500 km and at (-30°, 0°) in latitude and longitude and the corresponding result derived by CFT, apart from four regional peaks at 24 h, 12 h, 8 h, and 6 h which have been found in the "64 GPS-week data", the annual and semi-annual frequency can also be observed in the long-term density series. However, the largest amplitude still appears on the daily period and is the most dominating frequency component existing in the

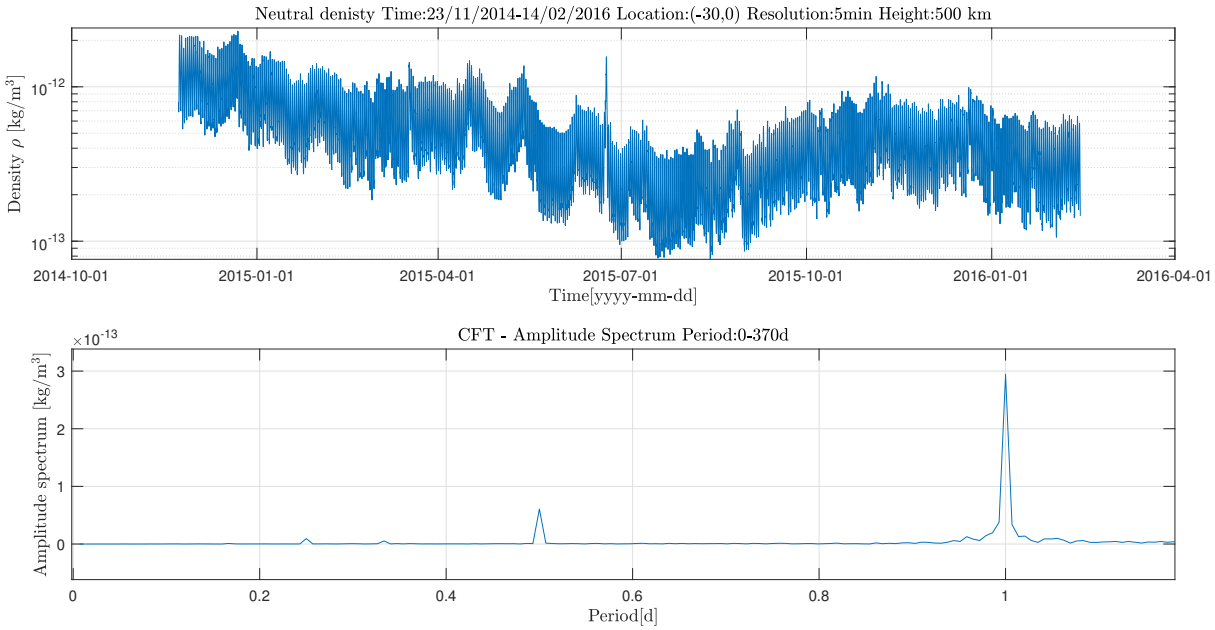

Figure 3.4: Local enlarged view of amplitude spectrum derived by CFT (bottom) of the series of thermospheric density (top) in the investigation period.

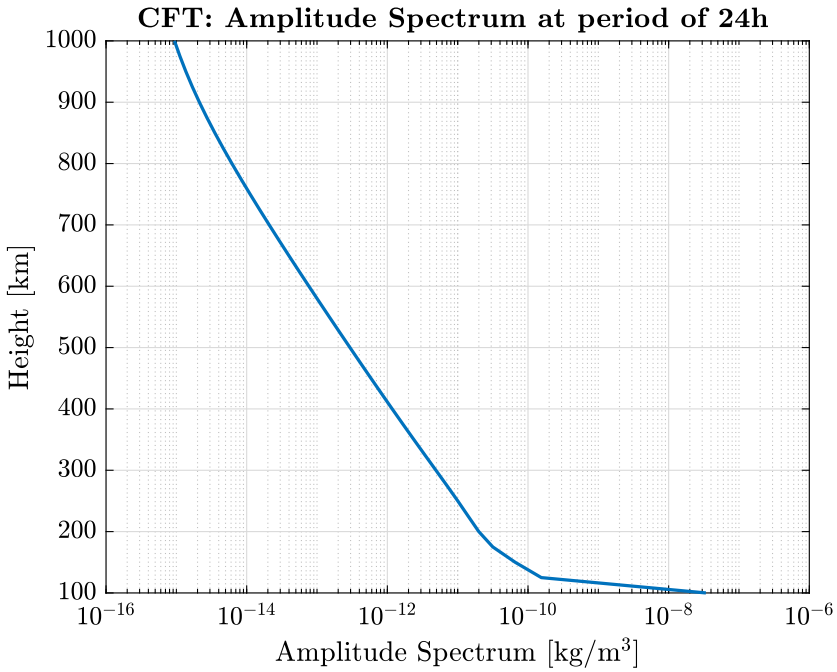

Figure 3.5: The amplitude spectrum at the period of 24 h derived by CFT as a function of altitude.

thermosphere NRLMSISE-00 model.

Nevertheless, the test results in Fig. 3.6 and Fig. 3.7 only prove that the signal with more repeating cycles can be used to detect the basis frequency better than that with fewer repeating cycles. It is not proper to suppose, the result in Fig. 3.6 is wrong because the period of 6.54 is also close to 2π. When it comes to the time series of thermospheric density and the Fourier transform in Fig. 3.3 which is also fine, it can be concluded that the annual variation in the investigation period is not exactly one year, and the annual period is not that distinct due to the short-term time series of neutral densities.

Furthermore, considering that 6 h is the minimum period found in the thermospheric density series, it is appropriate to generate the thermosphere model represented by B-splines with the temporal resolution of 1 h, which is a compromise between the computational work and the great description of density variations with time.

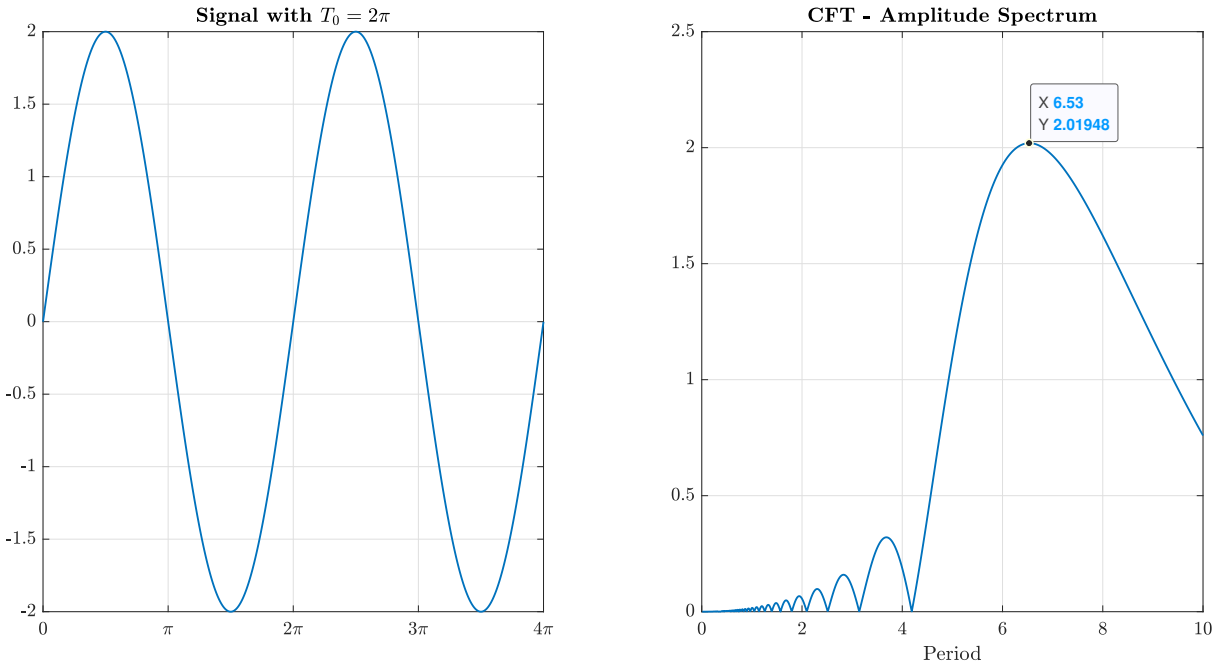

Figure 3.6: A CFT test (right) performed on a periodical sin signal with basis period of 2π repeating 2 cycles (left).

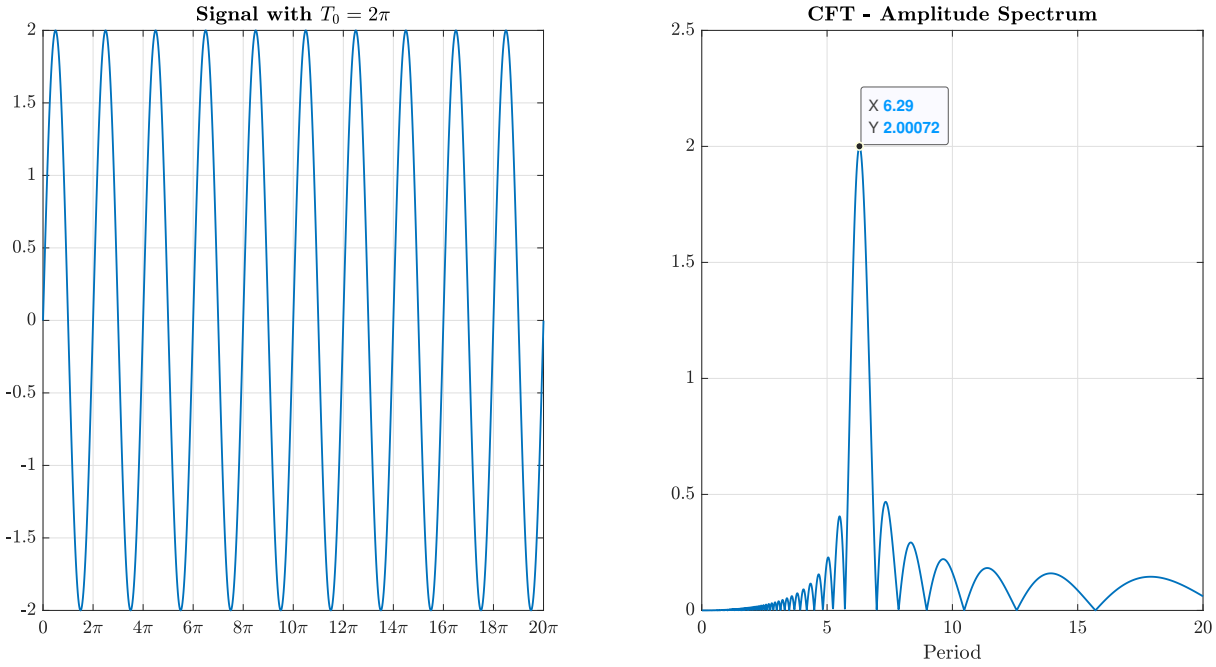

Figure 3.7: A CFT test (right) performed on a periodical sin signal with basis period of 2π repeating 10 cycles (left).

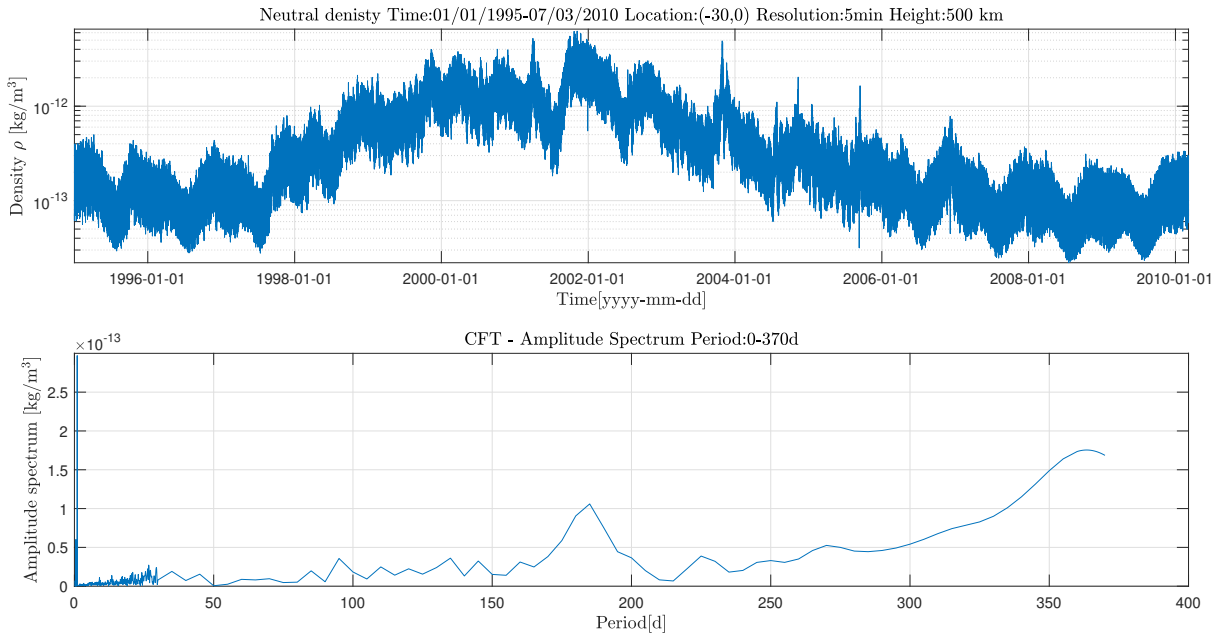

Figure 3.8: An example of amplitude spectrum derived by CFT (bottom) of the 15-year series of thermospheric density (top).

4 Thermospheric density modeling approach - B-spline modeling

In this study, we rely on B-splines as basis functions for thermosphere modeling. The main characteristics of this approach are primarily defined by the disadvantages of other parametrization techniques such as Spherical Harmonics (SH): 1) The basis functions are compactly supported, namely, only non-zero in a local environment on the sphere to allow for the modification of present data or incorporation of new data into the model without causing a global effect. 2) The representation is continuous within the modeling region. [Limberger, 2015] By combining the one-dimensional basis functions by means of tensor products, multidimensional models can be constructed easily.

4.1 B-splines

For this purpose, polynomial and trigonometric B-splines with local support have been selected as appropriate basis function candidates for representing the thermospheric information derived from the empirical NRLMSISE-00 model in the space. In contrast to SH, which are defined on a sphere and related to latitude and longitude via the associated Legendre polynomials, B-spline basis functions are commonly defined in the Euclidean space $\mathbb{R}^2$ and therefore need to be constrained in case of global spherical modeling. However, since space observations for thermosphere modeling are typically available with heterogeneous distribution and quality, the feature of compact support clearly outweighs the issue of applying global constraints [Limberger, 2015]. Furthermore, B-splines can be used to generate a Multi-scale representation (MSR) [Schmidt et al., 2015; Schmidt, 2007a]. In the following sections, two kinds of basis functions, namely normalized quadratic polynomial B-splines and normalized periodic trigonometric B-splines are described.

4.1.1 Normalized Polynomial Quadratic B-splines

In the following, the normalized polynomial quadratic B-splines $N_{J,k}^n(x)$ with degree $n = 2$ of resolution level $J_1 \in \mathbb{N}_0$ and shift $k_1 = 0, 1, ..., K_{J_1} - 1$ identifying a specific spline function is applied to model the latitude-dependent variations of thermospheric density within a bounded interval, that is,

$$\phi_{k_1}^{J_1}(\varphi) := N_{J_1,k_1}^2(\varphi) \tag{4.1}$$

where $\phi_{k_1}^{J_1}(\varphi)$ is the 1-D scaling function depending on latitude φ.

Specifically speaking, a total of $K_{J_1} = 2^{J_1} + 2$ B-splines are located along a meridian depending on the latitude $\varphi \in [-90°, 90°]$. The model resolution is controlled by the level, i.e., the higher

J_1, the finer the signal structures that can be resolved. To construct the K_{J_1} B-spline functions, the sequence

$$\underbrace{-90^\circ = \phi_0^{J_1} = \phi_1^{J_1} = \phi_2^{J_1}}_{\text{Boundary multiplicity}} \underbrace{< \phi_3^{J_1} < ... <}_{\text{Internal sequence}} \underbrace{\phi_{K_{J_1}}^{J_1} = \phi_{K_{J_1}+1}^{J_1} = \phi_{K_{J_1}+2}^{J_1} = 90^\circ}_{\text{Boundary multiplicity}} \tag{4.2}$$

of knot points $\phi_{k_1}^{J_1}$ is established, where, at the boundaries, multiple knots have to be linked to a specific coordinate point. The consideration of multiple knot points at the poles is called "endpoint-interpolating" and ensures the closing of the modeling interval. The constant difference between two consecutive knots $\phi_{k_1}^{J_1}$ and $\phi_{k_1+1}^{J_1}$ for $k_1 = 2, ..., K_{J_1} - 1$ amounts to $180^\circ/2^{J_1}$ [Goss et al., 2019]. Referring to Schumaker and Traas [1991] and Stollnitz et al. [1995] the normalized quadratic polynomial B-spline can be computed with the recursive relation

$$N_{J_1,k_1}^n(\varphi) = \frac{\varphi - \varphi_{k_1}^{J_1}}{\varphi_{k_1+n}^{J_1} - \varphi_{k_1}^{J_1}} N_{J_1,k_1}^{n-1}(\varphi) + \frac{\varphi_{k_1+n+1}^{J_1} - \varphi}{\varphi_{k_1+n+1}^{J_1} - \varphi_{k_1+1}^{J_1}} N_{J_1,k_1+1}^{n-1}(\varphi) \tag{4.3}$$

with $n = 1, 2$ from the initial values

$$N_{J_1,k_1}^0(\varphi) = \begin{cases} 1 & \text{if} \quad \varphi_{k_1}^{J_1} \leq \varphi < \varphi_{k_1+1}^{J_1} \quad \text{and} \quad \varphi_{k_1}^{J_1} < \varphi_{k_1+1}^{J_1} \\ 0 & \text{others,} \end{cases} \tag{4.4}$$

where in Eq.4.3 a factor is set to zero if the denominator is equal to zero.

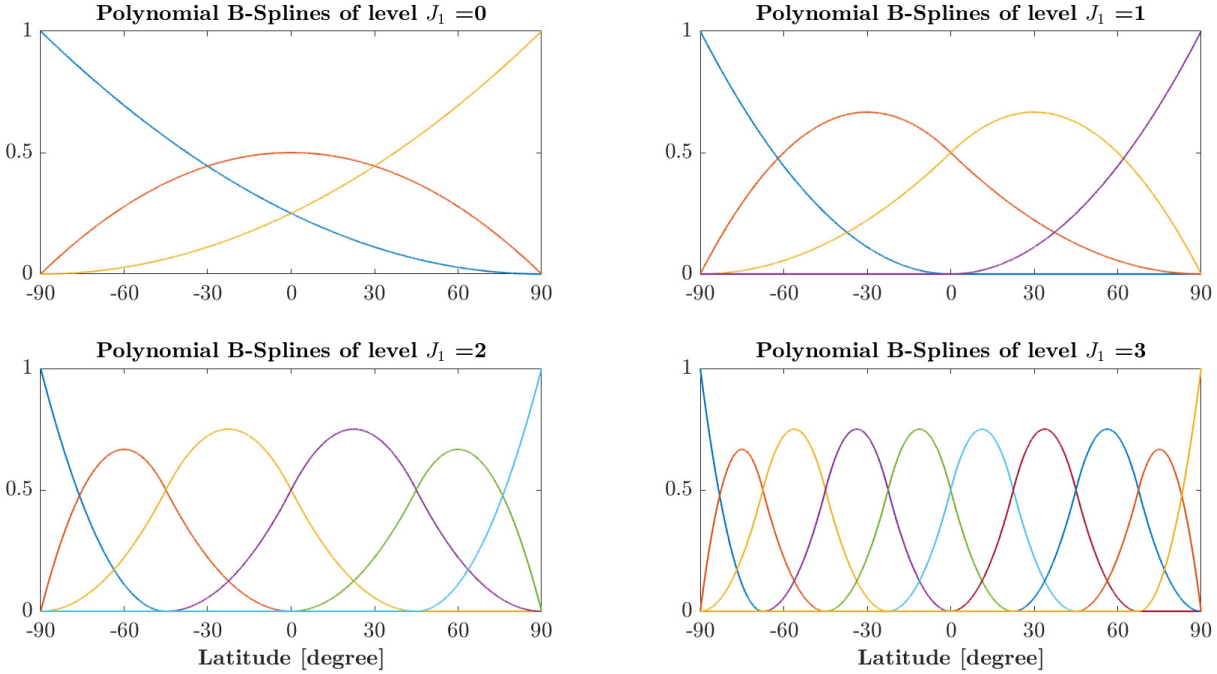

Figure 4.1: Normalized quadratic polynomial B-splines with different levels $J_1 = 0, 1, 2, 3$ and accordingly different numbers of B-splines $K_{J_1} = 3, 4, 6, 10$

.

Fig. 4.1 provides examples of endpoint-interpolating polynomial B-spline functions of degree $n = 2$ regarding different levels $J_1 = 0, 1, 2, 3$. The number of splines varies with J_1 where the subplots are related to $J_1 = 0 \rightarrow K_0 = 3$ (top-left), $J_1 = 1 \rightarrow K_1 = 4$ (top-right), $J_1 = 2 \rightarrow$

$K_2 = 6$ (bottom-left) and $J_1 = 3 \rightarrow K_3 = 10$ (bottom-right). Special features of polynomial B-splines are in particular given by the endpoint-interpolation, i.e., adaptation of the splines to a bounded interval, and localization, i.e., they are different from zero only within a small subinterval of length $\delta_{J_1} \approx 3 \cdot h_{J_1}$ where

$$h_{J_1} = \frac{180^\circ}{2^{J_1} + 1} \tag{4.5}$$

means the approximate distance between two consecutive B-splines along the meridian [Schmidt et al., 2011].

It can be clearly seen from the plots, that the first two and last two splines are different with respect to the interior spline functions contributing to the endpoint-interpolation in the bounded interval. A comparison of all four figures demonstrates how the B-spline support interval changes with J_1, i.e., the higher the level the smaller the influenced area and the sharper the peaks. From Fig. 4.1 it becomes visible that always three adjacent splines are overlapping, i.e., a single data point contributes to the determination of exactly three B-spline coefficients [Limberger, 2015]. As the level J_1 determines the total number K_{J_1} of B-splines, the increasing J_1 can be used to model the finer structures of density variations. Therefore, the model resolution is defined by J_1 and should be adapted to the input data density to overcome data gaps. For the case of homogeneous data sampling, the selection of the level J_1 relates to the sampling interval $\Delta\varphi$ of the input data in latitude dependency according to [Schmidt et al., 2011]

$$\Delta\varphi < h_{J_1}. \tag{4.6}$$

Combining Eq. 4.5 and Eq. 4.6, the inequality constraint

$$J_1 \leq \log_2 \left(\frac{180^\circ}{\Delta\varphi} - 1\right) \tag{4.7}$$

is solved.

4.1.2 Normalized Trigonometric B-splines

In the modeling of variations of thermospheric densities in longitudinal direction, we apply trigonometric B-splines $T^3_{J_2,k_2}(\lambda)$ of order 3 with the resolution level $J_2 \in \mathbb{N}_0$ and shift $k_2 = 0, 1, ..., K_{J_2} - 1$, that is,

$$\phi^{J_2}_{k_2}(\lambda) := T^3_{J_2,k_2}(\lambda) \tag{4.8}$$

where $\phi^{J_2}_{k_2}(\lambda)$ is the 1-D scaling function depending on longitude λ.

To be more specific, the total number $K_{J_2} = 3 \cdot 2^{J_2}$ of trigonometric B-splines are located along the parallels of the chosen spherical coordinate system within the interval $\lambda \in [0^\circ, 360^\circ)$. For constructing K_{J_2} B-spline functions, the sequence of knot points

$$0^\circ = \lambda^{J_2}_0 < \lambda^{J_2}_1 < ... < \lambda^{J_2}_{k_2} < ... < \lambda^{J_2}_{K_{J_2}-1} < 360^\circ \tag{4.9}$$

with additional knots

$$\lambda^{J_2}_{K_{J_2}+i} = \lambda^{J_2}_i + 360^\circ \quad \text{for} \quad i = 0, 1, 2 \tag{4.10}$$

for considering the periodicity is established. Consequently, the first and the last two B-spline functions within the interval $[0^\circ, 360^\circ)$ are completed by the so-called "wrapping around" effect. This constraint allows trigonometric B-splines to be defined in two different ways:

1. Following Schumaker and Traas [1991], Jekeli [2005] and Limberger [2015] periodic trigonometric B-splines can be calculated by a recurrence relation similar to Eq. (4.3). Thereby, additional constraints have to be introduced to force the periodicity of the series coefficients.
2. The second option was introduced by Lyche and Schumaker [2000] and used by Schmidt et al. [2011], Schmidt et al. [2015] and Goss et al. [2019]. It will be described in the following in more detail.

Similar to the polynomial B-splines, the distance between two consecutive knots $\lambda_{k_2}^{J_2}$ and $\lambda_{k_2+1}^{J_2}$ for $k_2 = 0, 1, ..., K_{J_2} - 1$ reads

$$h_{J_2} = \frac{360^\circ}{K_{J_2}} = \frac{120^\circ}{2^{J_2}}. \tag{4.11}$$

Following Lyche and Schumaker [2000], the functions are defined as

$$M_{J_2,k_2}(\lambda) = T^3_{J_2,k_2}(\lambda) = T^3_{h_{J_2}}(\lambda - \lambda_{k_2}^{J_2}) \tag{4.12}$$

with setting $h_{J_2} = h$ and $\lambda - \lambda_{k_2}^{J_2} = \Theta$ for the sake of simplification, thus, the function $T^3_{h_{J_2}}(\lambda - \lambda_{k_2}^{J_2}) = T^3_h(\Theta)$ can be computed via

$$T^3_h(\Theta) = \begin{cases} \dfrac{\sin^2(\Theta/2)}{\sin(h/2)\sin(h)} & \text{for} \quad 0 \le \Theta < h \\ \dfrac{1}{\cos(h/2)} - \dfrac{\sin^2((\Theta-h)/2) + \sin^2((2h-\Theta)/2)}{\sin(h/2)\sin(h)} & \text{for} \quad h \le \Theta < 2h \\ \dfrac{\sin^2((3h-\Theta)/2)}{\sin(h/2)\sin(h)} & \text{for} \quad 2h \le \Theta < 3h \\ 0 \quad \text{others.} \end{cases} \tag{4.13}$$

Finally, the basis functions are obtained as

$$\phi_{k_2}^{J_2}(\lambda) = \begin{cases} M_{J_2,k_2}(\lambda) & \text{for} \quad k_2 = 0, ..., K_{J_2} - 3 \\ M_{J_2,k_2}(\lambda) + M_{J_2,k_2}(\lambda - 360^\circ) & \text{for} \quad k_2 = K_{J_2} - 2, K_{J_2} - 1. \end{cases} \tag{4.14}$$

As can be seen from Fig. 4.2 which provides examples of trigonometric B-spline functions regarding different levels $J_2 = 0, 1, 2, 3$. The number of splines varies with J_2 where the subplots are related to $J_2 = 0 \rightarrow K_0 = 3$ (top-left), $J_2 = 1 \rightarrow K_1 = 6$ (top-right), $J_2 = 2 \rightarrow K_2 = 12$ (bottom-left) and $J_2 = 3 \rightarrow K_2 = 24$ (bottom-right), the length of the non-zero subinterval of a B-spline function is given as $\delta_{J_2} = 3 \cdot h_{J_2} = 360^\circ / 2^{J_2}$. Similarities to the polynomial B-spline functions can be found in the local support and the overlap of three splines at each point along x-axis. The main difference is related to the boundary splines where, in contrast to the endpoint-interpolation of polynomial splines, the periodicity is visible. Although different colors have been chosen for each function, it can be clearly seen that every sub-spline at one boundary is continued at the opposite boundary. For instance in the top-left illustration for $J_2 = 0$, the yellow spline on the right can be connected with the yellow spline on the left without any discontinuation. Similar to the polynomial B-splines, the choice of the level J_2 depends on the sampling interval $\Delta\lambda$ of input data in the longitudinal direction. Parallel to Eq. 4.6, the inequal constraint $\Delta\lambda < h_{J_2}$ needs be fulfilled. Solving the inequality above together with Eq. 4.11, we obtain

$$J_2 \le \log_2 \left(\frac{120^\circ}{\Delta\lambda}\right). \tag{4.15}$$

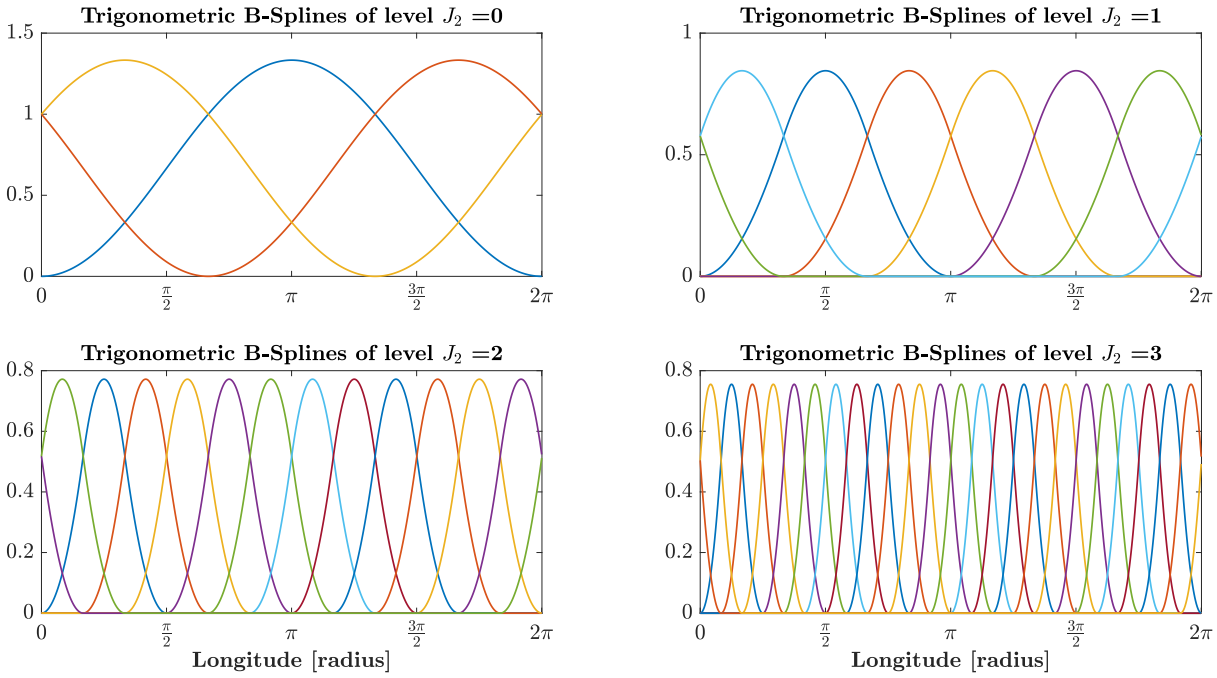

Figure 4.2: Trigonometric B-splines with different levels $J_2 = 0, 1, 2, 3$ and accordingly different number of B-splines $K_{J_2} = 3, 6, 12, 24$.

4.1.3 B-spline tensor products

The earth sphere S can be defined as

$$R_S := \{(\varphi, \lambda) : -90^\circ \leq \varphi \leq 90^\circ \quad \text{and} \quad 0 \leq \lambda < 2\pi\} \tag{4.16}$$

with coordinates φ (unit: degree) and λ (unit: radius) in an angular system mapped on a rectangle R_S in a 2-D space $\mathbb{R}^2$. In order to represent multidimensional information on the rectangular modeling surface as introduced in Eq. (4.16), tensor products of B-spline basis functions shall be applied in an orthogonal coordinate system. Details about tensor product techniques for surface modeling can, e.g., be found in Dierckx [1984]; Meyling and Pfluger [1987]; Zeilhofer [2008].

For a 2-D case representation, the approximation function s can be constructed from

$$s(x_1, x_2) = \sum_{k_1=0}^{K_{J_1}-1} \sum_{k_2=0}^{K_{J_2}-1} d_{k_1,k_2}^{J_1,J_2} \, \phi_{k_1}^{J_1}(x_1) \, \phi_{k_2}^{J_2}(x_2), \tag{4.17}$$

where tensor products of two linearly independent 1-D B-spline functions $\phi_{k_1}^{J_1}$ and $\phi_{k_2}^{J_2}$ have been introduced together with the corresponding series coefficients $d_{k_1,k_2}^{J_1,J_2}$. It should be noticed that $\phi_{k_1}^{J_1}$ and $\phi_{k_2}^{J_2}$ may differ but can also be of the same type.

Firstly, the 2-D basis is generated from the combination of polynomial and trigonometric B-spline functions, which is generally corresponding to the case of global modeling on the Earth. Therefore, the basis is defined as

$$x_1 \to \phi_{k_1}^3(\varphi) \quad \text{and} \quad x_2 \to \phi_{k_2}^2(\lambda) \tag{4.18}$$

for different levels $J_1 = 3$ and $J_2 = 2$ with endpoint-interpolation in the x_1 (latitude) and continuity in the x_2 (longitude) direction. Figure 4.3 shows the support area for $\phi_4^3(\varphi)$ and $\phi_7^2(\lambda)$ in this spline constellation. The right subplot additionally shows the 3-D shape of a 2-D tensor B-spline product basis related to the emphasized splines of the left graph.

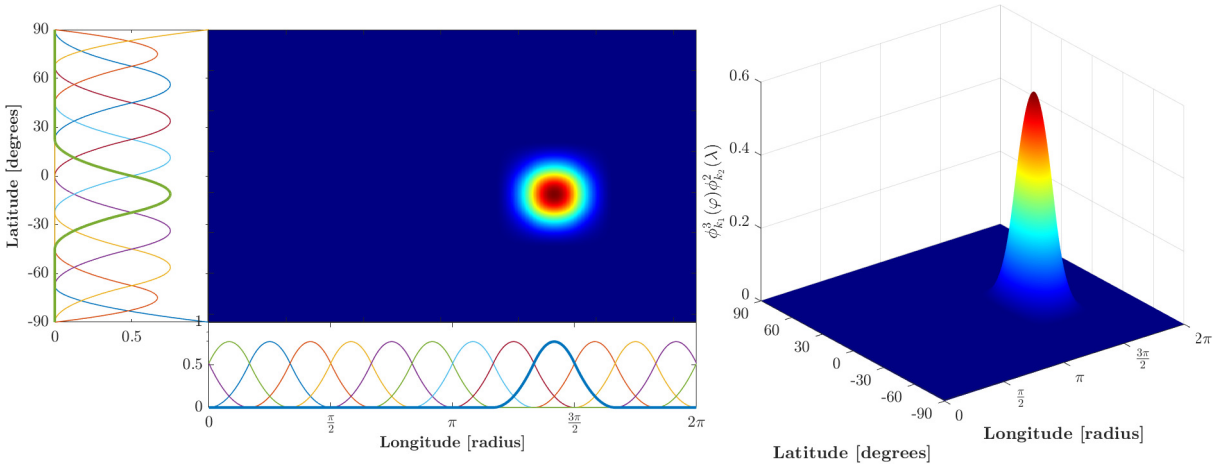

Figure 4.3: Combination of polynomial B-splines with level $J_1 = 3$ and trigonometric B-splines with level $J_2 = 2$. A specific spline combination identified by $k_1 = 4$ and $k_2 = 7$ has been highlighted and plotted in the center part of the left subplot. Accordingly, a 3-D representation of the tensor product is given on the right-hand side.

For each additional dimension, a new set of basis functions can be incorporated, i.e., the B-spline expansion can easily be adapted to higher or lower dimensions by means of the tensor product technique. For example, a 3-D modeling basis is accordingly defined as

$$s(x_1, x_2, x_3) = \sum_{k_1=0}^{K_{J_1}-1} \sum_{k_2=0}^{K_{J_2}-1} \sum_{k_3=0}^{K_{J_3}-1} d_{k_1,k_2,k_3}^{J_1,J_2,J_3} \, \phi_{k_1}^{J_1}(x_1) \, \phi_{k_2}^{J_2}(x_2) \, \phi_{k_3}^{J_3}(x_3). \tag{4.19}$$

Further details about B-spline expansions for multidimensional modeling are, for instance, published by Schmidt et al. [2015]. These generally derived formulations for basis representations with normalized quadratic polynomial B-splines and normalized periodic trigonometric B-splines, individual and combined in tensor products, will now be adapted for thermosphere modeling.

4.2 Thermosphere modeling with B-splines

Different function characteristics are crucial to select a suitable set of basis functions. It has been shown that polynomial B-splines are rather convenient for regional modeling applications due to the endpoint-interpolation while trigonometric B-splines are preferable for global modeling. A more concrete formulation for thermosphere modeling is provided and tensor products of 1-D B-spline scaling functions for the multidimensional representation in the spatio-temporal domain are introduced.

4.2.1 Two-dimensional thermosphere modeling

The thermospheric density depending on latitude and longitude is firstly considered at a certain time moment and a specific altitude. This signal is transformed into a B-spline representation in terms of a 2-D tensor products of two 1-D basis functions depending on latitude and longitude. The 2-D thermospheric density signal $Q(\varphi,\lambda)$ plus the error $e(\varphi,\lambda)$ can be represented as the series expansion [Schmidt, 2007b]

$$Q(\varphi,\lambda)+e(\varphi,\lambda)=\sum_{k_1=0}^{K_{J_1}-1}\sum_{k_2=0}^{K_{J_2}-1} d_{k_1,k_2}^{J_1,J_2}\,\phi_{k_1,k_2}^{J_1,J_2}\,(\varphi,\lambda) \tag{4.20}$$

in terms of 2-D basis functions

$$\phi_{k_1,k_2}^{J_1,J_2}(\varphi,\lambda)=\phi_{k_1}^{J_1}(\varphi)\,\phi_{k_2}^{J_2}(\lambda) \tag{4.21}$$

as the tensor product of of two 1-D basis functions $\phi_k^J(x)$ depending on $x\in\{\varphi,\lambda\}$ with unknown series coefficients $d_{k_1,k_2}^{J_1,J_2}$. $\phi_k^J(x)$ is of resolution level $J\in\mathbb{N}_0$ $(J\in\{J_1,J_2\})$ and shift $k\in\mathbb{N}_0$ $(k\in\{k_1,k_2\})$ [Liang, 2017].

According to the discussion above, the polynomial and trigonometric B-splines as basis functions in latitudinal and longitudinal directions are applied to form a 2-D tensor product with unknown B-spline coefficients of number which depends on resolution levels J_1 and J_2. According to Table 4.1 in Goss et al. [2019] which shows numerical values for the B-spline levels J_1 and J_2, and the corresponding required input data sampling interval $\Delta\varphi$ and $\Delta\lambda$. If the global sampling intervals $\Delta\varphi$ and $\Delta\lambda$ are known, the two level values J_1 and J_2 can be calculated from Eqs. (4.7) and (4.15). A 2.5° x 5° resolution in latitude and longitude used in thermospheric density grids matches the level values $J_1\leq 6$ and $J_2\leq 4$. However, the final choice for two resolution levels J_1 and J_2 shall be discussed based on the knowledge of ionosphere modeling.

In the ionosphere modeling, most of the Global Ionosphere Models (GIM) are based on series expansions in terms of SH with a maximum degree of $n_{max}=15$. This value fits a block size of about $12^\circ\times 12^\circ$ on the sphere Ω_H with radius $R_H=R_E+H$, where H is the single-layer height and R_E is the radius of the Earth [Goss et al., 2019]. In contrast, a grid spacing of $2.5^\circ\times 5^\circ$ corresponds to a maximum SH degree of around $n=36$. As a matter of fact, a reliable computation of the corresponding SH series coefficients requires a global input data coverage of the same spatial sampling. Due to the limitation of observation distribution, the maximum degree $n_{max}=15$ is generally used in SH. Referring to Goss et al. [2019], based on $n_{max}=15$, we obtain the assumptions $J_1=4$ (for $n_{max}=17$) and $J_2=3$ (for $n_{max}=12$) for the two B-spline levels J_1 and J_2, which can be seen as the spectrally closest representation to the current International GNSS Service (IGS) solutions.

Therefore, based on the experience in ionosphere modeling, $J_1=4$ and $J_2=3$ are chosen for 2-D thermospheric density modeling in this thesis. For $J_1=4$ and $J_2=3$, the modeling system has $K_{J_1}=18$ polynomial B-splines and $K_{J_2}=24$ trigonometric B-splines, thus, totally $K_{J_1}\cdot K_{J_2}=324$ B-spline coefficients.

In the next step, the unknown B-spline coefficients are estimated in the linear adjustment system with thermospheric densities as input observations and 2-D tensor products in the

Table 4.1: Numerical values for the B-spline levels J_1 and J_2, the input data sampling intervals $\Delta\varphi$ and $\Delta\lambda$ by evaluating the inequalities from Eq. (4.7) and Eq. (4.15); the left part of the table presents the numbers along a meridian (Eq. (4.7)), and the right part presents the numbers along the equator and its parallels according to Eq. (4.15).

Latitude							Longitude						
J_1	1	2	3	4	5	6	J_2	1	2	3	4	5	6
$\Delta\varphi$	60°	36°	20°	10.5°	5.45°	2.85°	$\Delta\lambda$	60°	30°	15°	7.5°	3.75°	1.875°

design matrix. For this purpose, Eqs. (4.20) and (4.21) need to be rewritten in vector and matrix notation. We introduce the $K_{J_1} \times 1$ vector

$$\boldsymbol{\phi}_{J_1}(\varphi) = \begin{bmatrix} \phi_0^{J_1}(\varphi) & \phi_1^{J_1}(\varphi) & \cdots & \phi_{K_{J_1}-1}^{J_1}(\varphi) \end{bmatrix}^T, \tag{4.22}$$

the $K_{J_2} \times 1$ vector

$$\boldsymbol{\phi}_{J_2}(\lambda) = \begin{bmatrix} \phi_0^{J_2}(\lambda) & \phi_1^{J_2}(\lambda) & \cdots & \phi_{K_{J_2}-1}^{J_2}(\lambda) \end{bmatrix}^T \tag{4.23}$$

and the $K_{J_1} \times K_{J_2}$ coefficient matrix

$$\mathbf{D}_{J_1,J_2} = \begin{bmatrix} d_{0,0}^{J_1,J_2} & d_{0,1}^{J_1,J_2} & \cdots & d_{0,K_{J_2}-1}^{J_1,J_2} \\ d_{1,0}^{J_1,J_2} & d_{1,1}^{J_1,J_2} & \cdots & d_{1,K_{J_2}-1}^{J_1,J_2} \\ \vdots & \vdots & \ddots & \vdots \\ d_{K_{J_1}-1,0}^{J_1,J_2} & d_{K_{J_1}-1,1}^{J_1,J_2} & \cdots & d_{K_{J_1}-1,K_{J_2}-1}^{J_1,J_2} \end{bmatrix}. \tag{4.24}$$

Considering the computation rules for the Kronecker product "$\bigotimes$" [Koch, 1999], Eq. (4.20) can be written as

$$\begin{aligned} Q(\varphi,\lambda) + e(\varphi,\lambda) &= (\boldsymbol{\phi}_{J_2}(\lambda) \bigotimes \boldsymbol{\phi}_{J_1}(\varphi))^T \mathrm{vec}\mathbf{D}_{J_1,J_2} \\ &= \boldsymbol{\phi}_{J_1,J_2}(\varphi,\lambda)\ \mathrm{vec}\mathbf{D}_{J_1,J_2} \end{aligned} \tag{4.25}$$

where $\boldsymbol{\phi}_{J_1,J_2}(\varphi,\lambda) = (\boldsymbol{\phi}_{J_2}(\lambda) \otimes \boldsymbol{\phi}_{J_1}(\varphi))^T$, and "vec" refers to the vec operator. which is defined as

$$\mathrm{vec}\begin{bmatrix} \boldsymbol{X} & \boldsymbol{Y} \\ \boldsymbol{U} & \boldsymbol{V} \end{bmatrix} = \begin{bmatrix} \boldsymbol{X} \\ \boldsymbol{U} \\ \boldsymbol{Y} \\ \boldsymbol{V} \end{bmatrix}. \tag{4.26}$$

In the case of 2-D global modeling, there is one grid presenting the thermospheric density expressed as

$$\mathbf{Q}(\boldsymbol{\varphi},\boldsymbol{\lambda}) = \begin{bmatrix} Q(\varphi_1,\lambda_1) & Q(\varphi_1,\lambda_2) & \cdots & Q(\varphi_1,\lambda_n) \\ Q(\varphi_2,\lambda_1) & Q(\varphi_2,\lambda_2) & \cdots & Q(\varphi_2,\lambda_n) \\ \vdots & \vdots & \ddots & \vdots \\ Q(\varphi_m,\lambda_1) & Q(\varphi_m,\lambda_2) & \cdots & Q(\varphi_m,\lambda_n) \end{bmatrix} \tag{4.27}$$

where m, n are the numbers of discrete latitude and longitude values of the thermospheric density grid.

And the tensor product needs to be computed for each grid point obtaining

$$\mathbf{TP}(\boldsymbol{\varphi}, \boldsymbol{\lambda}) = \begin{bmatrix} \boldsymbol{\phi}_{J_1,J_2}(\varphi_1, \lambda_1) & \boldsymbol{\phi}_{J_1,J_2}(\varphi_1, \lambda_2) & \cdots & \boldsymbol{\phi}_{J_1,J_2}(\varphi_1, \lambda_n) \\ \boldsymbol{\phi}_{J_1,J_2}(\varphi_2, \lambda_1) & \boldsymbol{\phi}_{J_1,J_2}(\varphi_2, \lambda_2) & \cdots & \boldsymbol{\phi}_{J_1,J_2}(\varphi_2, \lambda_n) \\ \vdots & \vdots & \ddots & \vdots \\ \boldsymbol{\phi}_{J_1,J_2}(\varphi_m, \lambda_1) & \boldsymbol{\phi}_{J_1,J_2}(\varphi_m, \lambda_2) & \cdots & \boldsymbol{\phi}_{J_1,J_2}(\varphi_m, \lambda_n) \end{bmatrix}. \tag{4.28}$$

Therefore, the functional model in B-spline modeling describing a linear adjustment system where $\hat{\mathbf{y}}$ means the corrected observations which is related to the original observations $\mathbf{y}$ by the error vector $\mathbf{e}$, and $\hat{\mathbf{x}}$ means the vector of estimated unknown parameters, is expressed based on Eq. (4.25) as

$$\hat{\mathbf{y}}_{2D} = \mathbf{A}_{2D}\hat{\mathbf{x}}_{2D} \tag{4.29}$$

with the $N \times 1$ ($N = m \cdot n$) matrix

$$\hat{\mathbf{y}}_{2D} = \text{vec } \mathbf{Q}(\boldsymbol{\varphi}, \boldsymbol{\lambda}) + \mathbf{e} = \mathbf{y}_{2D} + \mathbf{e}, \tag{4.30}$$

the $N \times K$ ($K = K_{J_1} \cdot K_{J_2}$) matrix

$$\mathbf{A}_{2D} = \text{vec } \mathbf{TP}(\boldsymbol{\varphi}, \boldsymbol{\lambda}), \tag{4.31}$$

the $K \times 1$ matrix

$$\hat{\mathbf{x}}_{2D} = \text{vec } \mathbf{D}_{J_1,J_2}. \tag{4.32}$$

In real work, the generation of the design matrix in B-spline transformation is the key procedure since it has to be arranged in the same sequence of observations in terms of latitude and longitude. Algorithm 4.1 describes how the design matrix in 2-D adjustment system is generated by several for-loops. In this algorithm, the location of observations is traversed in a latitude-first way, that is, for one fixed longitude, all grid points along the corresponding meridian are arranged followed by those corresponding to the next longitude. The way of longitude-first is feasible as well once the arrangement of observations and 2-D tensor product in terms of locations is in the same sequence.

As a consequence, the B-spline coefficients are estimated by the least-squares adjustment with the introduction of weighting matrix $\mathbf{P}_{2D}$, reading as

$$\hat{\mathbf{x}}_{2D} = (\mathbf{A}_{2D}^T\mathbf{P}_{2D}\mathbf{A}_{2D})^{-1}\mathbf{A}_{2D}^T\mathbf{P}_{2D}\mathbf{y}_{2D}. \tag{4.33}$$

Generally, the arrangement of the weighting matrix $\mathbf{P}_{2D}$ in the estimation of B-spline coefficients for thermosphere has three widely used options:

1. The first one is directly using a unit matrix with the dimension of $N \times N$, that is,

$$\mathbf{P}_{2D} = \mathbf{I}_{N\times N} \tag{4.34}$$

   stating that all the input observations in one horizontal plane keep the same weight.

2. The second one regards the inversion of the $N \times N$ variance-covariance matrix $\mathbf{K}_{2D}$ of the observations as the weighting matrix. In this case,

$$\mathbf{P}_{2D} = \mathbf{K}_{2D}^{-1}. \tag{4.35}$$

Algorithm 4.1: *DesignMatrix* − 2*D* (*LAT*,*LON*,J_1,d_1,J_2)

Input: A latitude vector **LAT**, a longitude vector **LON**, the level and degree for polynomial B-splines in latitude dependency J_1, d_1, the level for trigonometric B-splines in longitude dependency J_2

Output: The design matrix **A** in 2-D B-spline modeling

```
K_J1 = 1 : (2^J1 + d1);
K_J2 = 1 : (3 * 2^J2);
r = 0;
for i2 = 1 : length(LON) do
    for i1 = 1 : length(LAT) do
        r = r+1;
        c = 0;
        for k2 = 1 : length(K_J2) do
            for k1 = 1 : length(K_J1) do
                c = c+1;
                A(r,c) = polynomial-
                 b(J1,d1,k1 − 1,LAT(i1),min(LAT),max(LAT))*trigonometric-
                 b(J2,k2,LON(i2));        ▷ polynomial-b, trigonometric-b = functions to
                 generate polynomial and trigonometric B-splines
```

3. The last one is to set up a weighting number for each observation dependent on the location of observations, e.g. latitude. This is raised according to the sphere shape of the earth, leading to the smaller amount of observations in the polar region compared to the equator, which consequently makes it reasonable to assign the weighting number to observations based on latitude. The cosine function can be used to describe desirably this weighting relationship. Nevertheless, the cosine value in the polar region is 0 which is not the real case, thus, a small value of 0.01 is added to each weighting number for all latitudes.

Amongst these options, the first one is the easiest, and the second cannot be achieved due to the lack of variance-covariance information of observations as they are derived from the empirical thermosphere model. Whereas the third option introduces the latitude-dependent number in the weighting matrix, which can be computed by the cosine value of latitude. This is because the higher latitude, the less amount of observations, in reality, resulting in less weight in the linear squares adjustment system, which can be described desirably by the cosine function. In this study, the third option (see Algorithm 4.2) is chosen since it considers the changing of observation volume observed with geodetic techniques, in particular, only one grid point in the polar region.

Finally, the reconstructed thermospheric densities can be computed as well by means of Eq. (4.29), which exactly represents the rebuilt part of input neutral densities purely derived by the B-spline model, in other words, the difference between reconstructed $\hat{\mathbf{y}}$ and original densities $\mathbf{y}$ represents the observation part beyond the abilities of B-spline modeling with specific levels. Furthermore, the neutral density at one grid point which never appears in the grid points of observations can be estimated as well with the involvement of all B-spline coefficients, obtaining as

$$Q(\varphi', \lambda') = \boldsymbol{\phi}_{J_1,J_2}(\varphi', \lambda')\hat{\mathbf{x}}_{2D}. \tag{4.36}$$

Algorithm 4.2: *WeightingMatrix* $-$ *2D* (LAT, LON)

Input: A latitude vector **LAT**, a longitude vector **LON**
Output: The weighting matrix $\mathbf{P}_{2D}$ in 2-D B-spline modeling

```
r = 0;
for i2 = 1 : length(LON) do
    for i1 = 1 : length(LAT) do
        r = r+1;
        P(r,r) = cos(LAT(i1)) + 0.01; ▷ The addition of 0.01 is for avoiding the problem
         of singularity
```

4.2.2 Three-dimensional thermosphere modeling

It is certainly possible to introduce any vertical profile function to combine it with mathematical B-spline basis functions [Zeilhofer, 2008]. The exponential function is used for fitting the variations of vertical profiles in thermosphere-related applications. However, as a B-spline-oriented study, it is also valuable to include the additional B-spline basis functions for the third dimension, the height h, which is the way adopted for 3-D thermospheric density modeling in this thesis. Besides, the polynomial B-spline basis function is applied in the height dimension due to the characteristics at the boundaries.

The three-dimensional thermospheric density signal $Q(\phi, \lambda, h)$ can be represented as the series expansion

$$Q(\varphi,\lambda,h) + e(\varphi,\lambda,h) = \sum_{k_1=0}^{K_{J_1}-1} \sum_{k_2=0}^{K_{J_2}-1} \sum_{k_3=0}^{K_{J_3}-1} d_{k_1,k_2,k_3}^{J_1,J_2,J_3}\ \phi_{k_1,k_2,k_3}^{J_1,J_2,J_3}(\varphi,\lambda,h) \tag{4.37}$$

in terms of 3-D basis function

$$\phi_{k_1,k_2,k_3}^{J_1,J_2,J_3}(\varphi,\lambda,h) = \phi_{k_1}^{J_1}(\varphi)\ \phi_{k_2}^{J_2}(\lambda)\ \phi_{k_3}^{J_3}(h) \tag{4.38}$$

as the tensor product of of three 1-D basis functions $\phi_k^J(x)$ depending on $x \in \{\varphi, \lambda, h\}$ with unknown series coefficients $d_{k_1,k_2,k_3}^{J_1,J_2,J_3}$. $\phi_k^J(x)$ is of resolution level $J \in \mathbb{N}_0$ $(J \in \{J_1, J_2, J_3\})$ and shift $k \in \mathbb{N}_0$ $(k \in \{k_1, k_2, k_3\})$ [Schmidt, 2007b; Liang, 2017].

Compared to the 2-D B-spline modeling, the 3-D model not only represents the density variations in latitude and longitude but also includes the profiles along the height at each grid point globally. In other words, the 3-D tensor product is computed by three 1-D basis functions depending on latitude, longitude, and height. However, with a totally different variation pattern from that in 2-D model having a comparatively smooth change of numerical values of thermospheric densities, the vertical profile above one grid point on the ground presents the exponential attenuation with the increasing height. Therefore, the representation of neutral densities in height dependency is a new and key issue in B-spline modeling.

The linear adjustment system in 3-D modeling is not totally the same as that in 2-D modeling in terms of the tensor product, observation vector, and vector of B-spline coefficients since the variable of height needs to be included. We introduce the $K_{J_3} \times 1$ vector

$$\boldsymbol{\phi}_{J_3}(h) = \begin{bmatrix} \phi_0^{J_3}(h) & \phi_1^{J_3}(h) & \cdots & \phi_{K_{J_3}-1}^{J_3}(h) \end{bmatrix}^T \tag{4.39}$$

, then Eq. (4.37) can be rewritten as

$$\begin{aligned} Q(\varphi,\lambda,h)+e(\varphi,\lambda,h) &= (\boldsymbol{\phi}_{J_3}(h)\bigotimes(\boldsymbol{\phi}_{J_2}(\lambda)\bigotimes\boldsymbol{\phi}_{J_1}(\varphi)))^T \mathrm{vec}\mathbf{D}_{J_1,J_2,J_3} \\ &= \boldsymbol{\phi}_{J_1,J_2,J_3}(\varphi,\lambda,h)\ \mathrm{vec}\mathbf{D}_{J_1,J_2,J_3} \end{aligned} \tag{4.40}$$

where $\boldsymbol{\phi}_{J_1,J_2,J_3}(\varphi,\lambda,h) = (\boldsymbol{\phi}_{J_3}(h)\bigotimes(\boldsymbol{\phi}_{J_2}(\lambda)\bigotimes\boldsymbol{\phi}_{J_1}(\varphi)))^T$, and "vec" refers to the vec operator.

Specifically speaking, the observation vector $\mathbf{y}_{3D}$ is expressed as

$$\mathbf{y}_{3D} = \begin{bmatrix} \mathrm{vec}\mathbf{Q}(\boldsymbol{\varphi},\boldsymbol{\lambda},h_1) \\ \mathrm{vec}\mathbf{Q}(\boldsymbol{\varphi},\boldsymbol{\lambda},h_2) \\ \vdots \\ \mathrm{vec}\mathbf{Q}(\boldsymbol{\varphi},\boldsymbol{\lambda},h_s) \end{bmatrix} \tag{4.41}$$

where s is the number of discrete layers along the height and

$$\mathbf{Q}(\boldsymbol{\varphi},\boldsymbol{\lambda},h) = \begin{bmatrix} Q(\varphi_1,\lambda_1,h) & Q(\varphi_1,\lambda_2,h) & \cdots & Q(\varphi_1,\lambda_n,h) \\ Q(\varphi_2,\lambda_1,h) & Q(\varphi_2,\lambda_2,h) & \cdots & Q(\varphi_2,\lambda_n,h) \\ \vdots & \vdots & \ddots & \vdots \\ Q(\varphi_m,\lambda_1,h) & Q(\varphi_m,\lambda_2,h) & \cdots & Q(\varphi_m,\lambda_n,h) \end{bmatrix} \tag{4.42}$$

And the design matrix in 3-D B-spline representation is written as

$$\mathbf{A}_{3D} = \begin{bmatrix} \mathrm{vec}\mathbf{TP}(\boldsymbol{\varphi},\boldsymbol{\lambda},h_1) \\ \mathrm{vec}\mathbf{TP}(\boldsymbol{\varphi},\boldsymbol{\lambda},h_2) \\ \vdots \\ \mathrm{vec}\mathbf{TP}(\boldsymbol{\varphi},\boldsymbol{\lambda},h_s) \end{bmatrix} \tag{4.43}$$

with

$$\mathbf{TP}(\boldsymbol{\varphi},\boldsymbol{\lambda},h) = \begin{bmatrix} \boldsymbol{\phi}_{J_1,J_2,J_3}(\varphi_1,\lambda_1,h) & \boldsymbol{\phi}_{J_1,J_2,J_3}(\varphi_1,\lambda_2,h) & \cdots & \boldsymbol{\phi}_{J_1,J_2,J_3}(\varphi_1,\lambda_n,h) \\ \boldsymbol{\phi}_{J_1,J_2,J_3}(\varphi_2,\lambda_1,h) & \boldsymbol{\phi}_{J_1,J_2,J_3}(\varphi_2,\lambda_2,h) & \cdots & \boldsymbol{\phi}_{J_1,J_2,J_3}(\varphi_2,\lambda_n,h) \\ \vdots & \vdots & \ddots & \vdots \\ \boldsymbol{\phi}_{J_1,J_2,J_3}(\varphi_m,\lambda_1,h) & \boldsymbol{\phi}_{J_1,J_2,J_3}(\varphi_m,\lambda_2,h) & \cdots & \boldsymbol{\phi}_{J_1,J_2,J_3}(\varphi_m,\lambda_n,h) \end{bmatrix}. \tag{4.44}$$

It is difficult to describe the arrangement of the design matrix in 3-D modeling purely with matrix entry because only 2-D matrices can be written in the paper. Thus, algorithm 4.3 helps describe how the design matrix in 3-D adjustment system is generated. Similarly, a fixed and consistent sequence to arrange the observations and design matrix in terms of locations of grid points is needed in order to guarantee the correct B-spline coefficients to be estimated. In algorithm 4.3, on the basis of the latitude-first traverse, the longitude is traversed next for one fixed height.

As a result, the unknown B-spine coefficients in 3-D modeling are obtained with the same method in 2-D modeling as

$$\hat{\mathbf{x}}_{3D} = (\mathbf{A}_{3D}^T\mathbf{P}_{3D}\mathbf{A}_{3D})^{-1}\mathbf{A}_{3D}^T\mathbf{P}_{3D}\mathbf{y}_{3D}, \tag{4.45}$$

Algorithm 4.3: *DesignMatrix* $-$ *3D* (LAT, LON, H, J_1, d_1, J_2, J_3, d_3)

Input: A latitude vector **LAT**, a longitude vector **LON**, a height vector H, the level and degree for polynomial B-splines in latitude J_1, d_1, the level for trigonometric B-splines in longitude J_2, the level and degree for polynomial B-splines in height J_3, d_3

Output: The design matrix $\mathbf{A}_{3D}$ in 3-D B-spline modeling

```
1  K_{J_1} = 1 : (2^{J_1} + d_1);
2  K_{J_2} = 1 : (3 * 2^{J_2});
3  K_{J_3} = 1 : (2^{J_3} + d_3);
4  r = 0;
5  for i_3 = 1 : length(H) do
6      for i_2 = 1 : length(LON) do
7          for i_1 = 1 : length(LAT) do
8              r = r+1;
9              c = 0;
10             for k_3 = 1 : length(K_{J_3}) do
11                 for k_2 = 1 : length(K_{J_2}) do
12                     for k_1 = 1 : length(K_{J_1}) do
13                         c = c+1;
14                         A(r,c) = polynomial-b(J_1,d_1,k_1 - 1,LAT(i_1),min(LAT),max(LAT))
                            *trigonometric_b(J_2,k_2,LON(i_2))*polynomial-
                            b(J_3,d_3,k_3 - 1,H(i_3),min(H),max(H));   ▷ polynomial-b,
                            trigonometric-b = functions to generate polynomial and
                            trigonometric B-splines
```

which is arranged by

$$\hat{\mathbf{x}}_{3D} = \mathrm{vec}\mathbf{D}_{J_1,J_2,J_3} = \begin{bmatrix} \mathrm{vec}\mathbf{D}_{J_1,J_2}(0) \\ \mathrm{vec}\mathbf{D}_{J_1,J_2}(1) \\ \vdots \\ \mathrm{vec}\mathbf{D}_{J_1,J_2}(K_{J_3}-1) \end{bmatrix} \tag{4.46}$$

and

$$\mathbf{D}_{J_1,J_2}(k_3) = \begin{bmatrix} d_{0,0,k_3}^{J_1,J_2,J_3} & d_{0,1,k_3}^{J_1,J_2,J_3} & \cdots & d_{0,K_{J_2}-1,k_3}^{J_1,J_2,J_3} \\ d_{1,0,k_3}^{J_1,J_2,J_3} & d_{1,1,k_3}^{J_1,J_2,J_3} & \cdots & d_{1,K_{J_2}-1,k_3}^{J_1,J_2,J_3} \\ \vdots & \vdots & \ddots & \vdots \\ d_{K_{J_1}-1,0,k_3}^{J_1,J_2,J_3} & d_{K_{J_1}-1,1,k_3}^{J_1,J_2,J_3} & \cdots & d_{K_{J_1}-1,K_{J_2}-1,k_3}^{J_1,J_2,J_3} \end{bmatrix}. \tag{4.47}$$

Additionally, the weighting matrix $\mathbf{P}_{3D}$ needs to be considered seriously due to the exponential distribution of thermospheric densities in height dependency. Similarly, the latitude-dependent strategy is still applied in the weighting at one specific height. But the weighting along the height has several possibilities. The first one is a unit matrix in height dependency, which assumes the standard deviations of observations at different heights to be the same. However, due to the different magnitudes of observations dependent on height, the standard deviations of them are more likely to be at different levels, resulting in different weighting in the adjustment system. Therefore, the way of weighting can be that observations of high altitudes have more weight than those of lower altitudes. Due to the lack of precision information for original observations, there is no other choice but to set up the weighting matrix in 3-D thermosphere modeling with the precision information derived in 2-D modeling. For example, the standard deviation (STD)s of estimated observations at each altitude in 2-D B-spline transformation can be used to compute the weighting number corresponding to each height. Algorithm 4.4 describes the procedure of generating the weighting matrix of 3-D modeling, which is essentially the combination of options 2 and 3 in the weighting strategies raised in Section 4.2.1.

Algorithm 4.4: $WeightingMatrix-3D\ (LAT, LON, H)$

Input: A latitude vector **LAT**, a longitude vector **LON**, a height vector **H**
Output: The weighting matrix $\mathbf{P}_{3D}$ in 3-D B-spline modeling

```
r = 0;
for i_3 = 1 : length(H) do
    for i_2 = 1 : length(LON) do
        for i_1 = 1 : length(LAT) do
            r = r+1;
            P(r,r) = (cos(LAT(i_1)) + 0.01)/std(i_3)^2;   ▷ The addition of 0.01 is for
              avoiding the problem of singularity; std(h) corresponds to the average of
              standard deviations of estimated neutral densities at height h derived
              from 2-D modeling
```

4.2.3 Four-dimensional thermosphere modeling

On the basis of three-dimensional modeling, the representation of thermospheric densities can be extended to the context of 4-D by including temporal variations in the time domain. In this case, the tensor product is generated by the multiplication of four 1-D basis functions with exclusively trigonometric B-splines in longitude dependency.

The 4-D thermospheric density signal $\mathrm{D}(\phi, \lambda, h, t)$ can be represented as the series expansion

$$Q(\varphi, \lambda, h, t) + e(\varphi, \lambda, h, t) = \sum_{k_1=0}^{K_{J_1}-1} \sum_{k_2=0}^{K_{J_2}-1} \sum_{k_3=0}^{K_{J_3}-1} \sum_{k_4=0}^{K_{J_4}-1} d_{k_1,k_2,k_3,k_4}^{J_1,J_2,J_3,J_4} \, \phi_{k_1,k_2,k_3,k_4}^{J_1,J_2,J_3,J_4}(\varphi, \lambda, h, t) \tag{4.48}$$

in terms of 4-D basis function

$$d_{k_1,k_2,k_3,k_4}^{J_1,J_2,J_3,J_4}(\varphi, \lambda, h, t) = \phi_{k_1}^{J_1}(\varphi) \, \phi_{k_2}^{J_2}(\lambda) \, \phi_{k_3}^{J_3}(h) \, \phi_{k_4}^{J_4}(t) \tag{4.49}$$

as the tensor product of of four 1-D basis functions $\phi_k^J(x)$ depending on $x \in \{\varphi, \lambda, h, t\}$ with unknown series coefficients $d_{k_1,k_2,k_3,k_4}^{J_1,J_2,J_3,J_4}$. $\phi_k^J(x)$ is of resolution level $J \in \mathbb{N}_0$ ($J \in \{J_1, J_2, J_3, J_4\}$) and shift $k \in \mathbb{N}_0$ ($k \in \{k_1, k_2, k_3, k_4\}$).

The functional model in 4-D B-spline modeling reads as

$$\hat{\mathbf{y}}_{4D} = \mathbf{A}_{4D}\hat{\mathbf{x}}_{4D} \tag{4.50}$$

with $\hat{\mathbf{y}}_{4D}$ the corrected neutral densities with the dimension of $M \times 1$ (v is the number of time epochs and $M = m \cdot n \cdot s \cdot v$), $\mathbf{A}_{4D}$ the design matrix in spatio-temporal modeling with the dimension of $M \times O$ ($O = K_{J_1} \cdot K_{J_2} \cdot K_{J_3} \cdot K_{J_4}$), and $\hat{\mathbf{x}}_{4D}$ the B-spline coefficients with the dimension of $O \times 1$.

It has been known it is complicated to present matrices mentioned above using different variables, thus, only the algorithm to generate the design matrix in 4-D modeling is placed as shown in algorithm 4.6. The variables of four dimensions are traversed in the sequence of latitude, longitude, height, and time epoch, and the input observations are arranged in this sequence as well. In the next step, the B-spline coefficients are estimated by

$$\hat{\mathbf{x}}_{4D} = (\mathbf{A}_{4D}^T \mathbf{P}_{4D} \mathbf{A}_{4D})^{-1} \mathbf{A}_{4D}^T \mathbf{P}_{4D} \mathbf{y}_{4D}. \tag{4.51}$$

The choice of weighting matrix in spatio-temporal modeling of the thermosphere is similar to that in 3-D modeling, that is, the combination of options 2 and 3 in the weighting strategies raised in Section 4.2.1. And for the temporal dimension, the unit weighting is adopted due to the smooth variations in the time domain. Nevertheless, the different point is the average of STD values is computed with STDs covering all the time epochs for one specific height in one 4-D model as shown in algorithm 4.5.

Algorithm 4.5: $WeightingMatrix - 4D\ (LAT, LON, H, T)$

Input: A latitude vector **LAT**, a longitude vector **LON**, a height vector **H**, a time vector **T**

Output: The weighting matrix $\mathbf{P}_{4D}$ in 4-D B-spline modeling

```
r = 0;
for i4 = 1 : length(T) do
    for i3 = 1 : length(H) do
        for i2 = 1 : length(LON) do
            for i1 = 1 : length(LAT) do
                r = r+1;
                P(r,r) = (cos(LAT(i1)) + 0.01)/std(i3)^2;   ▷ The addition of 0.01 is for avoiding the problem of singularity; std(h) corresponds to the average of standard deviations of estimated neutral densities at height h derived from 2-D modeling involving the whole time period
```

Algorithm 4.6: *DesignMatrix* $-$ *4D* (LAT, LON, H, T, J_1, d_1, J_2, J_3, d_3, J_4, d_4)

Input: A latitude vector **LAT**, a longitude vector **LON**, a height vector **H**, a time vector **T**, the level and degree for polynomial B-splines in latitude J_1, d_1, the level for trigonometric B-splines in longitude J_2, the level and degree for polynomial B-splines in height J_3, d_3, the level and degree for polynomial B-splines in time J_4, d_4

Output: The design matrix $\mathbf{A}_{4D}$ in 4-D B-spline modeling

```
K_{J_1} = 1 : (2^{J_1} + d_1);
K_{J_2} = 1 : (3 * 2^{J_2});
K_{J_3} = 1 : (2^{J_3} + d_3);
K_{J_4} = 1 : (2^{J_4} + d_4);
r = 0;
for i_4 = 1 : length(T) do
    for i_3 = 1 : length(H) do
        for i_2 = 1 : length(LON) do
            for i_1 = 1 : length(LAT) do
                r = r+1;
                c = 0;
                for k_4 = 1 : length(K_{J_4}) do
                    for k_3 = 1 : length(K_{J_3}) do
                        for k_2 = 1 : length(K_{J_2}) do
                            for k_1 = 1 : length(K_{J_1}) do
                                c = c+1;
                                A(r,c) =
                                 polynomial-b(J_1,d_1,k_1 - 1,LAT(i_1),min(LAT),max(LAT))
                                 *trigonometric_b(J_2,k_2,LON(i_2))*polynomial-
                                 b(J_3,d_3,k_3 - 1,H(i_3),min(H),max(H))*polynomial-
                                 b(J_4,d_4,k_4 - 1,T(i_4),min(T),max(T));   ▷ polynomial-b,
                                 trigonometric-b = functions to generate polynomial and
                                 trigonometric B-splines
```

5 Experiment and evaluation

This chapter describes in detail the organization and implementation of the experiment, including the algorithm test using simulated data, and the computation using real density data derived based on NRLMSISE-00 thermosphere model. And the approach to evaluating the precision and accuracy of B-spline representation results is given afterwards.

5.1 Experiment design

5.1.1 Algorithm test

The correctness of the algorithms for B-spline transformation is tested using artificially generated data within the context of 1-D, 2-D and 3-D, which is allowed to achieve by the so-called "close-loop validation". Specifically speaking, a set of B-spline coefficients is estimated from the original input signal with the generation of a reconstructed signal at the same time. Then the reconstructed signal is reused as the new input signal to estimate a new set of coefficients and generate a new reconstructed signal. Basically, the new reconstructed signal and the old reconstructed signal only differ at the level of computational accuracy, i.e. 10^{-15} to 10^{-14}, which means the success of "close-loop validation" and the correctness of the algorithms. Figure 5.1 depicts the procedures of close-loop validation, which starts from the original input signal and ends with the new reconstructed signal.

In terms of how the simulated data looks like, it differs from 1-D to 3-D modeling. Firstly, the signal where all elements are 1 can be selected generally with different dimensions since it can be used directly as the so-called "new input signal" in close-loop validation. On the other hand, the harmonic signal on the basis of cosine and sine functions is chosen typically because it is a basic component included in the most of real signals in the Earth system. Furthermore, apart from the constant and harmonic signals, it is necessary to consider exponentially distributed signals as well in 3-D modeling because of the distribution characteristic of real thermospheric density along the height. Similarly, linear signals, quadratic signals, and cubic signals can also be considered in the 1-D test.

5.1.2 Thermospheric density modeling

In the experiment using real data, the thermospheric densities between 23/11/2014 and 14/03/2016 are chosen as the research dataset considering both the quiet period and storm period, i.e., St. Patrick's Day on 17–19 March 2015. Therefore, there are further mainly two-week data remarkable, which are 23/11/2014 - 30/11/2014 marked as "quiet period" and 15/03/2015 - 22/03/2015 marked as "storm period", so that the characteristics of B-spline transformation can be studied in both data pools in the changing space environment.

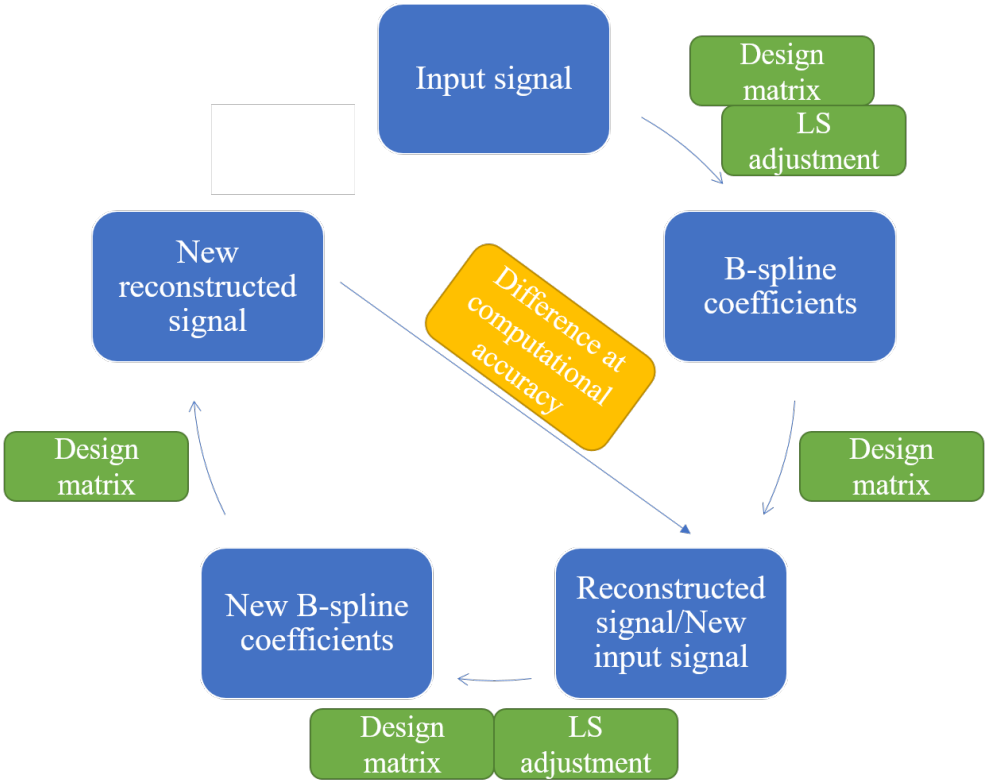

Figure 5.1: The sketch graph describing the procedures of close-loop validation.

With respect to the input data for estimating B-spline coefficients in the linear adjustment system, pre-processing is probably necessary due to the characteristic of the exponential distribution dependent on height and the extremely small number for thermospheric densities ranging from 10^{-11} to 10^{-15}. Specifically speaking, there are three different cases with respect to pre-processing of input observations.

1. For 2-D B-spline transformation where the thermospheric variations are dependent on latitude and longitude, the magnitudes of densities are the same, e.g. the neutral densities are always at the level of 10^{-12} kg/m^3 at 400 km altitude, thus, all the input densities can be multiplied by 10^{12} used for the further estimation which makes the computation easier and more efficient.

2. The condition changes in 3-D and 4-D cases due to the involvement of height-dependent variations, for example, the magnitudes of thermospheric densities range from 10^{-11} at 300 km to 10^{-15} at 1000 km. Similarly, an appropriate number, e.g. 10^{13}, can be multiplied with height-dependent thermospheric densities by which the input data involved in the adjustment system still distributes exponentially but with easier scientific notations.

3. Another method introduces the logarithmic model which firstly transforms exponential numbers E into logarithmic numbers L by

$$L = \ln(E). \tag{5.1}$$

   In this way, the exponentially distributed data is changed to the same magnitude preparing for further B-spline modeling.

In terms of 3-D and 4-D B-spline modeling, both method 2 and method 3 are possible to be deployed. The test and comparison between these two methods are performed prior to the derivation of products in Chapter 6.

In conclusion, the generated products in this study include:

1. The B-spline coefficients, the reconstructed thermospheric densities estimated in 2-D B-spline modeling within the investigation period. The spatial resolution is $2.5^\circ \times 5^\circ$ in latitude and longitude and 20 km in height.
2. The products derived from 2-D B-spline modeling are generated at each 5 min, from which a video consisting of sequentially layered figures can be provided.
3. The B-spline coefficients, the reconstructed thermospheric densities estimated in 3-D B-spline modeling within the investigation period. The spatial resolution is $2.5^\circ \times 5^\circ$ in latitude and longitude and 20 km in height.
4. The products derived from 3-D B-spline modeling are generated at each 5 min, from which a video consisting of sequentially layered figures can be provided.
5. The B-spline coefficients, the reconstructed thermospheric densities estimated in 4-D B-spline modeling within the investigation period. The spatial resolution is $2.5^\circ \times 5^\circ$ in latitude and longitude and 20 km in height. The temporal resolution is 5 min. There is no video produced because the temporal characteristic has been included in the 4-D model.

5.2 Evaluation approach

5.2.1 Comparison with model-derived densities

It is assumed that the thermospheric densities derived from the empirical NRLMSISE-00 model are error-free, thus, they are regarded as so-called "true" values and can be used to compare with density-grids represented by B-splines. Apart from the differences between estimated and input densities as shown in Eq. (5.2), the relative differences with respect to the input values are also regarded as an evaluation index, since the values of input observations differ significantly.

$$\begin{aligned} Q_{diff} &= Q_{est} - Q_{model} \\ Q_{relative} &= Q_{diff} / Q_{model} \end{aligned} \tag{5.2}$$

5.2.2 Stochastic model in least-squares adjustment

The least-squares adjustment is a key procedure to estimate B-spline coefficients and thus, the stochastic model in the adjustment including forming the weighting matrix and computing standard deviations of the estimated coefficients and reconstructed densities is an indispensable tool to evaluate the results of B-spline representation. In the least-squares adjustment model, the co-factor matrix of observations $\mathbf{Q}_{\mathbf{yy}}$ is set up which is just the inverse matrix of the weighting matrix of the observations used for adjustment, i.e., $\mathbf{P}_{\mathbf{yy}} = \mathbf{Q}_{\mathbf{yy}}^{-1}$. Besides, we define n, u as numbers of observations and estimated B-spline coefficients, respectively, $\mathbf{e} = \hat{\mathbf{y}} - \mathbf{y}$ as the difference vector between adjusted observations and original observations,

and matrix $\mathbf{A} \in \{\mathbf{A}_{2D}, \mathbf{A}_{3D}, \mathbf{A}_{4D}\}$ as the design matrix involved in the adjustment. Then, the posterior unit variance $\hat{\sigma}_0^2$, the variance-covariance matrix of estimated coefficients $\mathbf{K}_{\hat{\mathbf{x}}\hat{\mathbf{x}}}$ and reconstructed observations $\mathbf{K}_{\hat{\mathbf{y}}\hat{\mathbf{y}}}$ are expressed as

$$\begin{aligned} \hat{\sigma}_0^2 &= \frac{\hat{\mathbf{e}}^T \mathbf{P}_{\mathbf{yy}} \hat{\mathbf{e}}}{n-u} \\ \mathbf{Q}_{\hat{\mathbf{x}}\hat{\mathbf{x}}} &= (\mathbf{A}^T \mathbf{P}_{\mathbf{yy}} \mathbf{A})^{-1} \quad \hat{\mathbf{K}}_{\hat{\mathbf{x}}\hat{\mathbf{x}}} = \hat{\sigma}_0^2 \mathbf{Q}_{\hat{\mathbf{x}}\hat{\mathbf{x}}} \\ \mathbf{Q}_{\hat{\mathbf{y}}\hat{\mathbf{y}}} &= \mathbf{A} \mathbf{Q}_{\hat{\mathbf{x}}\hat{\mathbf{x}}} \mathbf{A}^T \quad \hat{\mathbf{K}}_{\hat{\mathbf{y}}\hat{\mathbf{y}}} = \hat{\sigma}_0^2 \mathbf{Q}_{\hat{\mathbf{y}}\hat{\mathbf{y}}}. \end{aligned} \tag{5.3}$$

Each element in the matrices $\mathbf{K}_{\hat{\mathbf{x}}\hat{\mathbf{x}}}$ and $\mathbf{K}_{\hat{\mathbf{y}}\hat{\mathbf{y}}}$ is related to a geographical position on the Earth. Hence, the arrangement and demonstration of them according to their positions is extremely helpful to assess the precision of modeling results and spatial dependency of the precision index.

Additionally, it is worth mentioning that, the consistency amongst the magnitudes of standard deviations of estimated B-spline coefficients and reconstructed neutral densities in the modeling with different dimensions is supposed to be guaranteed, which means the weighting strategy in height dependency needs to be considered seriously.

6 Results and discussion

In this chapter, the results for the algorithm test and B-spline modeling with model-derived dataset are presented and analyzed within the context of 2-D, 3-D, and 4-D representations. Besides, the comparison among these results is performed in terms of B-spline coefficients, represented thermospheric densities, standard deviations of them, and computational efficiency.

6.1 Algorithm test

6.1.1 One-dimensional signal

In this section, the simulated 1-D signals are represented either by polynomial or by trigonometric B-splines. As we know, the B-spline modeling can achieve the best precision when the original signal is constant, in which case, the difference between the reconstructed signal and the original signal is at the computational accuracy level. Figs. 6.1 and 6.3 show such results with the difference of 10^{-15} in the bottom figure and prove the correctness of the algorithm. Moreover, the sine function is used to generate a harmonic signal repeating 4 cycles in the time domain, which is modeled by trigonometric and polynomial B-splines of levels 5 and 3, respectively, resulting in the difference at 10^{-3} level as shown in Figs. 6.2 and 6.4. It can be seen that the use of harmonic signal results in the larger difference between the reconstructed and the original signal compared to the constant signal. This is because B-spline functions are not composed of standard harmonic functions even if they have similar shapes, thus, the standard harmonic signal cannot be reconstructed perfectly by B-spline basis functions.

6.1.2 Two-dimensional signal

Similarly, the 2-D constant signal in Fig. 6.5 is transformed to a set of B-spline coefficients via the tensor products computed by polynomial and trigonometric B-spline basis functions with the result of random difference at the 10^{-15} level. And Figs. 6.6 and 6.7 give a close-loop validation with the simulated 2-D harmonic signal. Specifically speaking, the original signal in Fig. 6.6 is used to compute the unknown B-spline coefficients and estimate the reconstructed signal, resulting in the difference at 10^{-3} level. Then the reconstructed signal in Fig. 6.6 is reused as the input signal in B-spline modeling to estimate the new B-spline coefficients as shown in Fig. 6.7, which results in the random difference at the computational accuracy level.

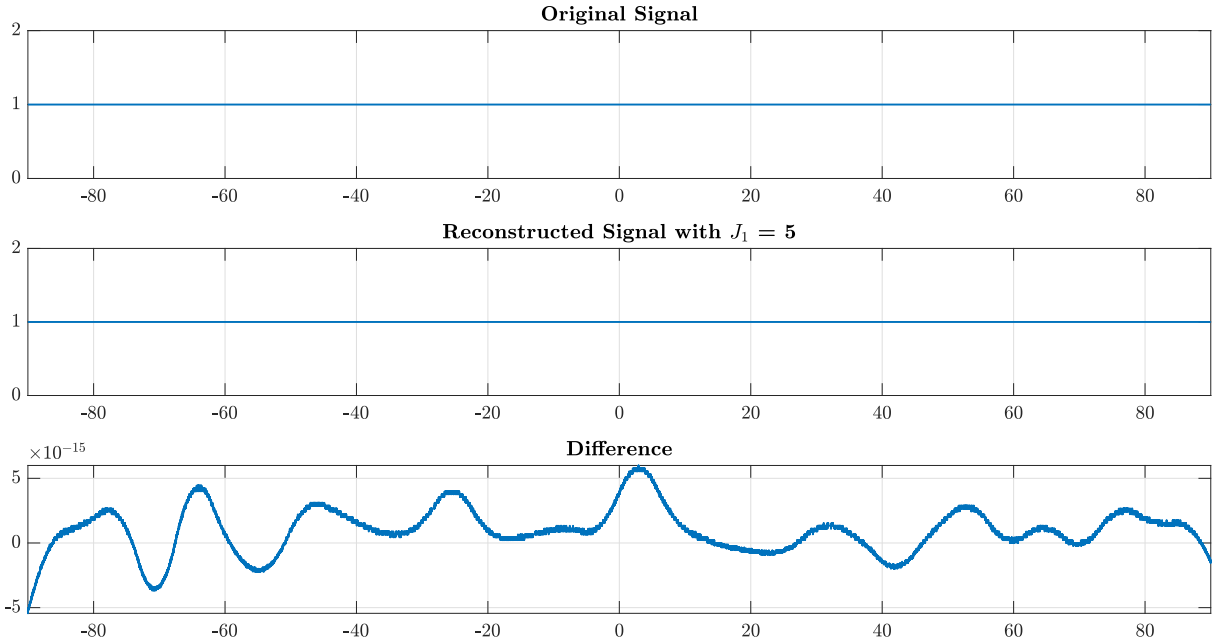

Figure 6.1: The 1-D simulation of the constant signal represented by polynomial B-splines with the resolution level of 5.

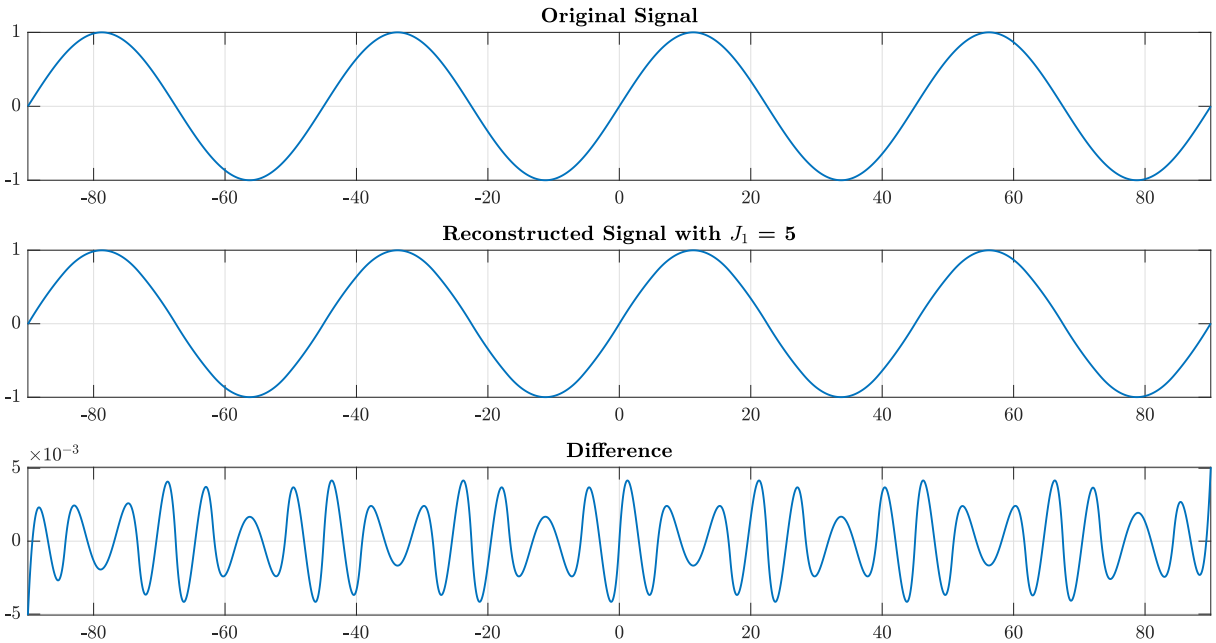

Figure 6.2: The 1-D simulation of the harmonic signal represented by polynomial B-splines with the resolution level of 5.

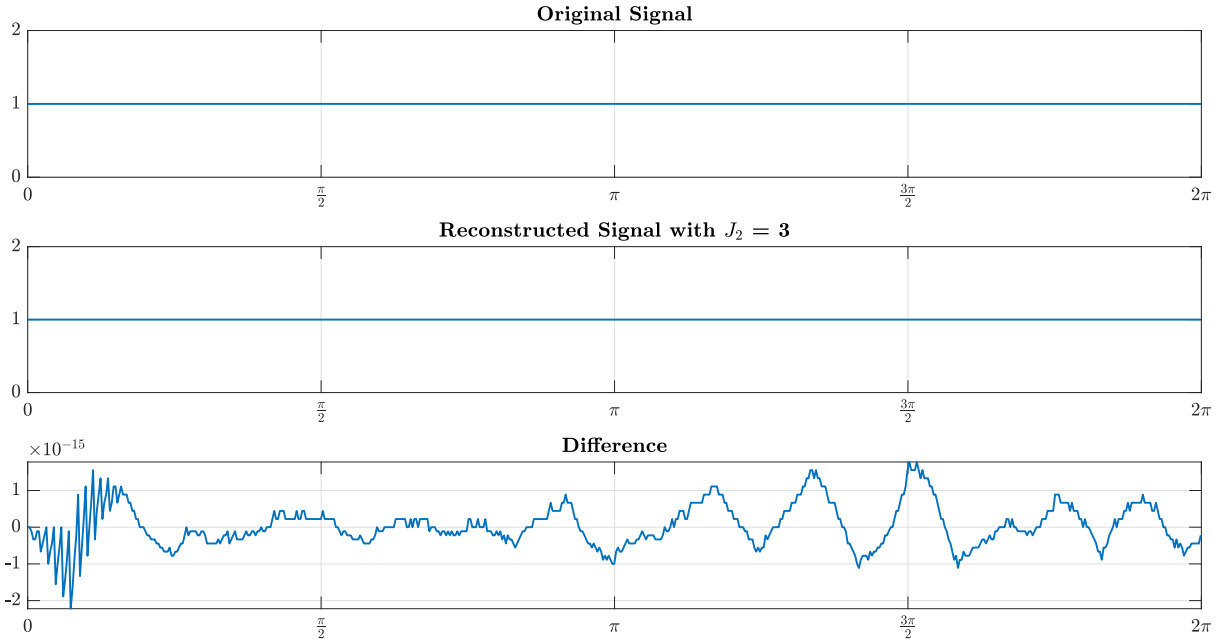

Figure 6.3: The 1-D simulation of the constant signal represented by trigonometric B-splines with the resolution level of 3.

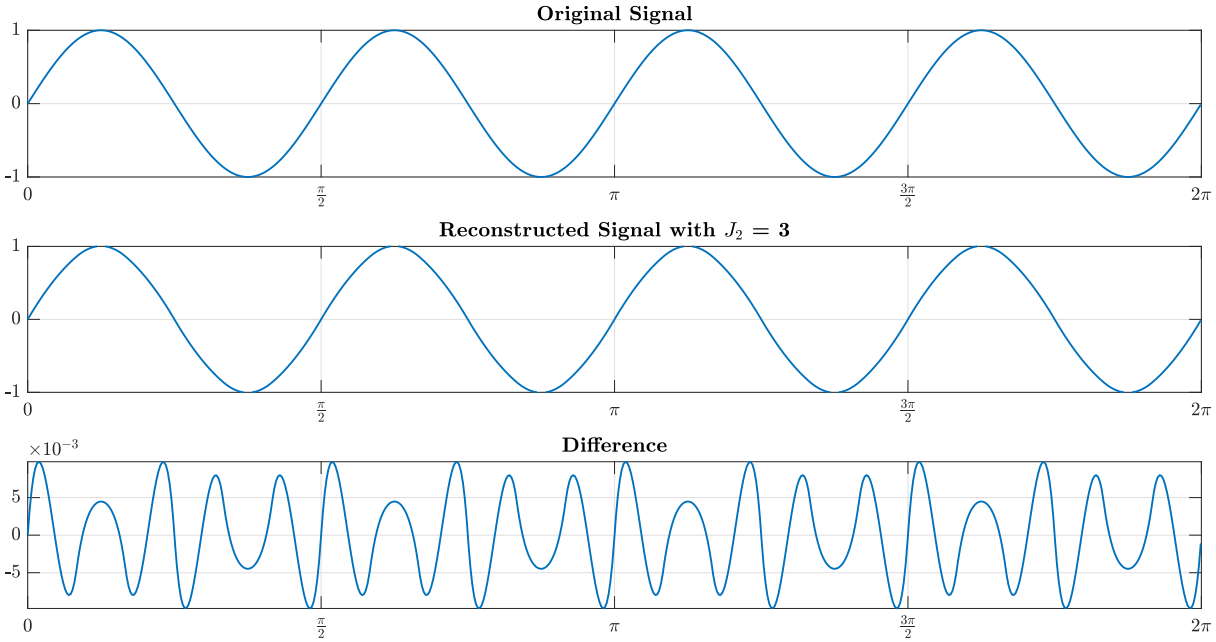

Figure 6.4: The 1-D simulation of the harmonic signal represented by trigonometric B-splines with the resolution level of 3.

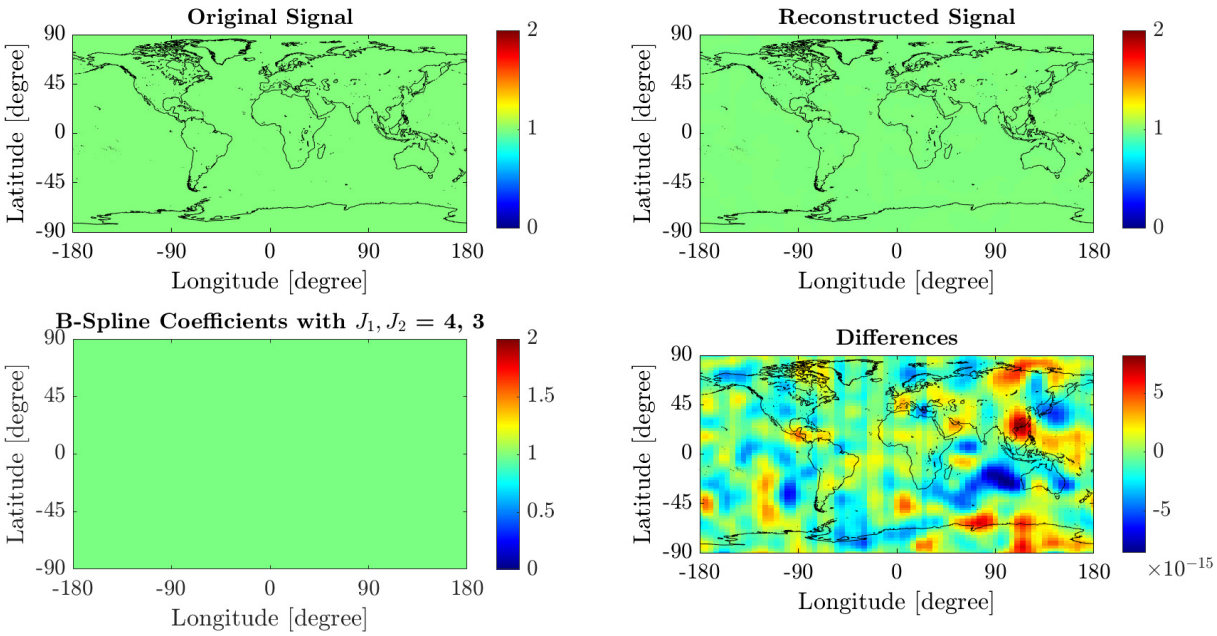

Figure 6.5: The 2-D simulation of the constant signal represented by polynomial and trigonometric B-splines with the resolution level of 4 and 3, respectively.

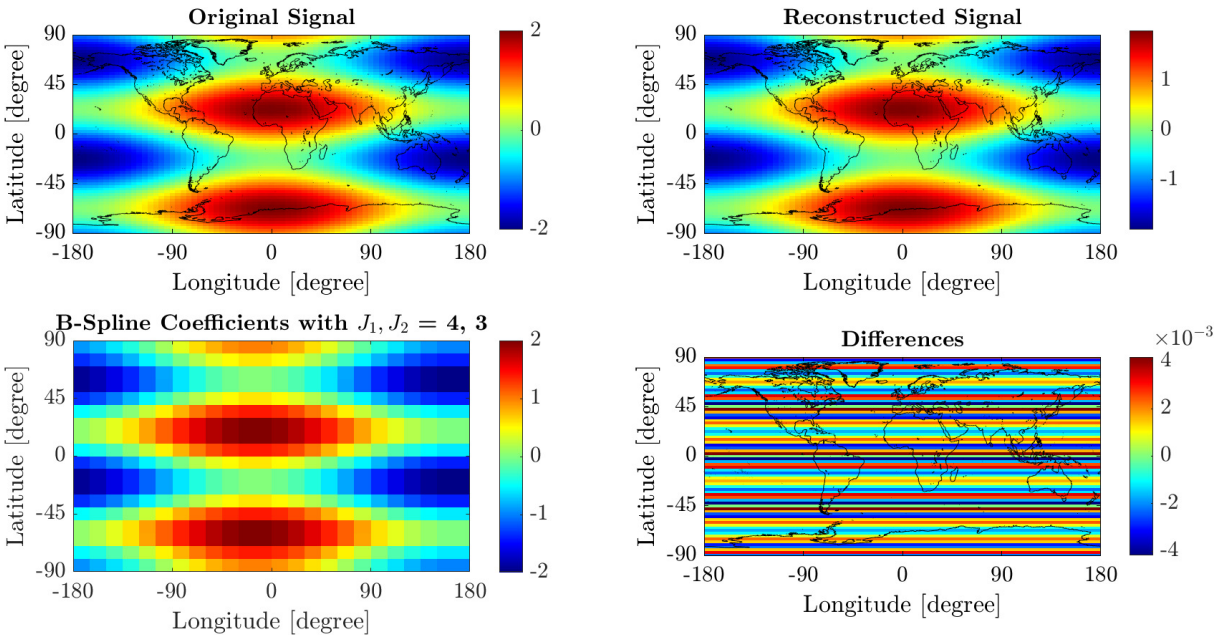

Figure 6.6: The 2-D simulation of the harmonic signal represented by polynomial and trigonometric B-splines with the resolution level of 4 and 3, respectively.

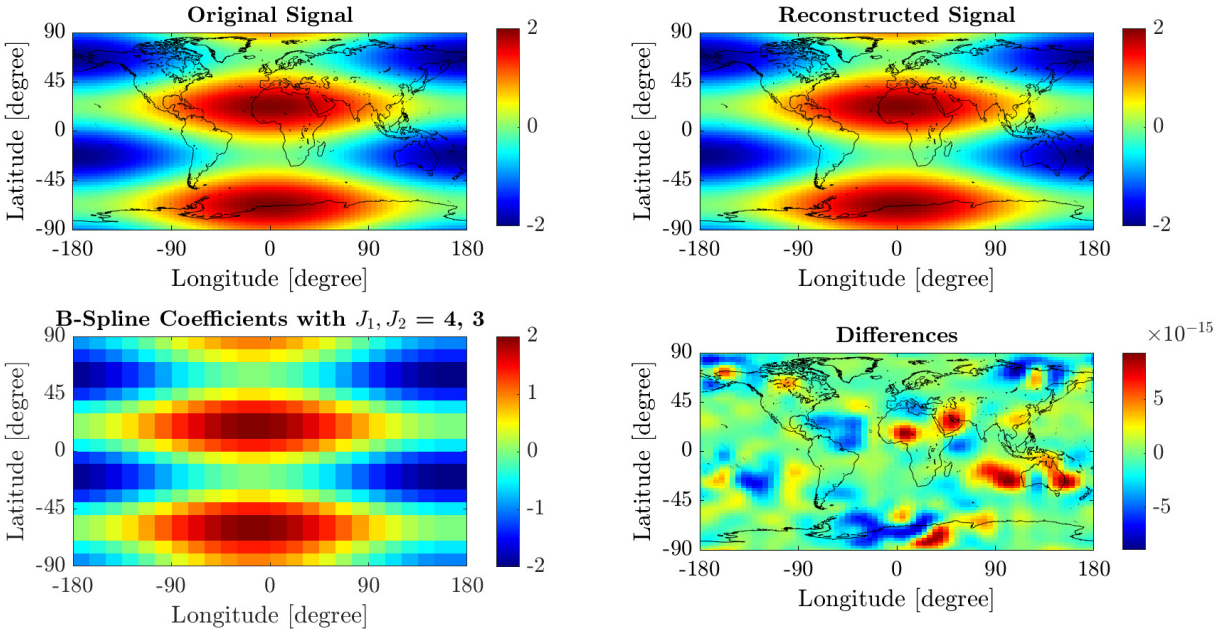

Figure 6.7: The 2-D close-loop validation of the harmonic signal represented by polynomial and trigonometric B-splines with the resolution level of 4 and 3, respectively.

6.1.3 Three-dimensional signal

Considering it is the first time to model the thermospheric density dependent on height using polynomial B-splines, there is no good reference to know the appropriate spatial resolution and level of B-splines. Therefore, a small test is set up in order to check the feasibility of B-spline representation in height dependency and how the different resolutions and levels are related to the different accuracy. The test is performed by transforming the 3-D modeling question to 1-D modeling question, i.e., modeling the 1-D profile of thermospheric densities as a function of altitude. For example, at 00:00:00 on 23/11/2014, one can select one specific grid point, for instance, (-30°, 0°) where the density profiles with different spatial intervals can be extracted as the observations. Since the height range involved in B-spline modeling is between 300 and 1000 km, 5 km, 10 km, 20 km, and 25 km can be possible spatial resolutions to be evaluated. In addition, two kinds of observations can be used, that is, logarithmic numbers of original thermospheric densities, and the multiplication of original observations with the number of 10^{13}, so that one can compare the accuracy of results derived from two kinds of input observations, and determine which one is used for performing real 3-D modeling.

Firstly, with respect to the comparison of results between two kinds of input observations, the relative differences between the reconstructed vertical profile and the original profile are presented in Figs 6.8 to 6.11. Obviously, the relative difference derived with the logarithmic model is smaller than that with the multiplication of original observations. More test examples on other locations and at other time moments are performed as well for the reliability of the test, and the same conclusion that the logarithmic model performs better is acquired. Therefore, the comparison in the following would focus on different pairs of spatial resolution of observations and resolution level of B-splines. Table 6.1 shows the test result at (-30°, 0°) at 00:00:00 on 23/11/2014 with the different selection of height interval and resolution level of B-splines as well as the average value of absolute of relative difference between B-spline represented profile and original profile. It can be observed that for one fixed height interval

Table 6.1: Test of single profile modeling at (30°, 0°) at 00:00:00 on 23/11/2014.

Height interval [km]	Resolution level J_3	Relative difference average
5	3	3.90e-04
5	4	5.79e-05
5	5	1.62e-05
5	6	1.02e-05
5	7	1.17e-06
10	3	4.04e-04
10	4	5.95e-05
10	5	1.68e-05
10	6	3.71e-06
20	3	4.43e-04
20	4	5.69e-05
20	5	9.22e-06
25	3	4.38e-04
25	4	5.82e-05

which means the number of observations along a vertical profile is fixed, the accuracy of the result improves with the increase of the resolution level of polynomial B-splines because the higher level represents the finer structure to be modeled. However, the highest level that can be used for a fixed height interval is limited due to the requirement of the numbers of observations and unknowns in least-squares estimation, and meanwhile, it needs more computational memory and time. Therefore, the aim is to find a compromise between the accuracy of vertical modeling for thermospheric densities and computational efficiency. In Table 6.1, the height interval of 20 km and the resolution level of 5 is the best choice considering the problem of computational efficiency and modeling accuracy. Nevertheless, the 3-D tensor product with the levels of 4,3,5 in latitude, longitude and height used for B-spline coefficients estimation is too large to perform the inversion of matrix in the adjustment due to the problem of memory. And the use of level 4 has reached the relative difference of 10^{-5} for a single vertical profile. As a consequence, 20 km and level 4 are adopted for modeling vertical variations of thermospheric densities in 3-D B-spline modeling.

The test described above proves the feasibility of modeling vertical variations of thermospheric density even if the single vertical profile of the thermosphere is studied each time because B-spline representation on a horizontal plane gets successful in the experiment of 2-D modeling. Extending from modeling height-dependent thermospheric densities individually at each grid point to modeling them as the third dimension in global modeling, it is reasonable to apply the height interval and resolution level selected based on the single profile test.

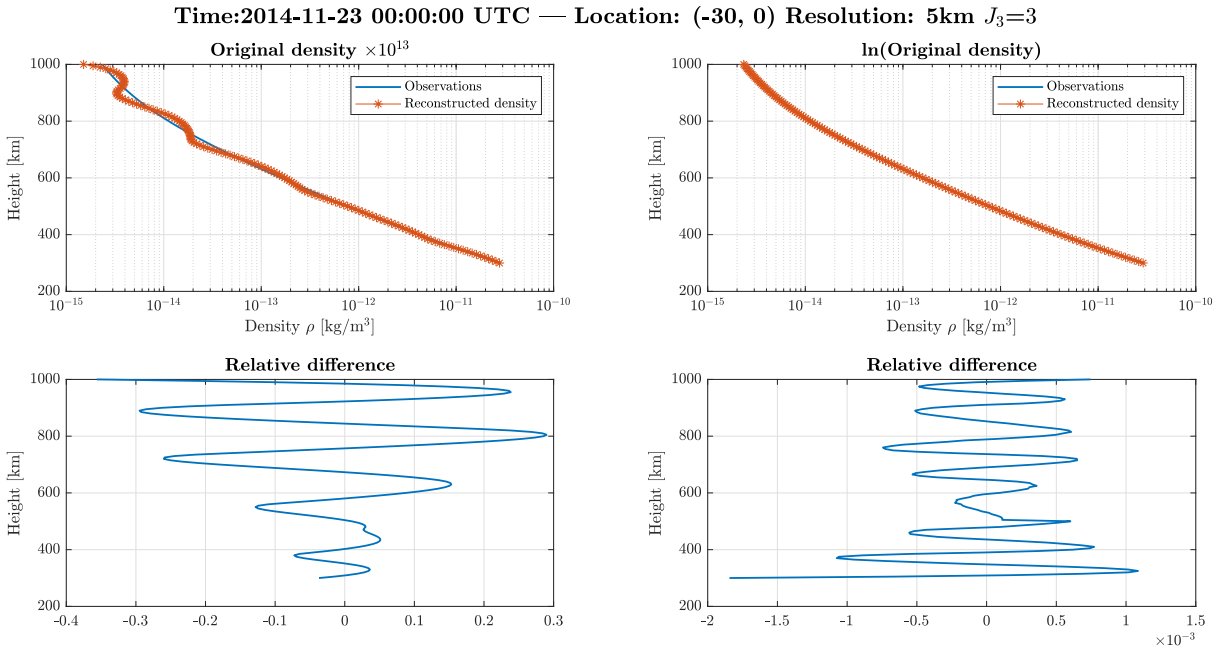

Figure 6.8: The 1-D thermospheric density with the resolution of 5 km as a function of altitude derived from the NRLMSISE-00 model and reconstructed from B-spline modeling with the resolution level of $J_3 = 3$ at (-30°, 0°) at 00:00:00 on 23/11/2014.

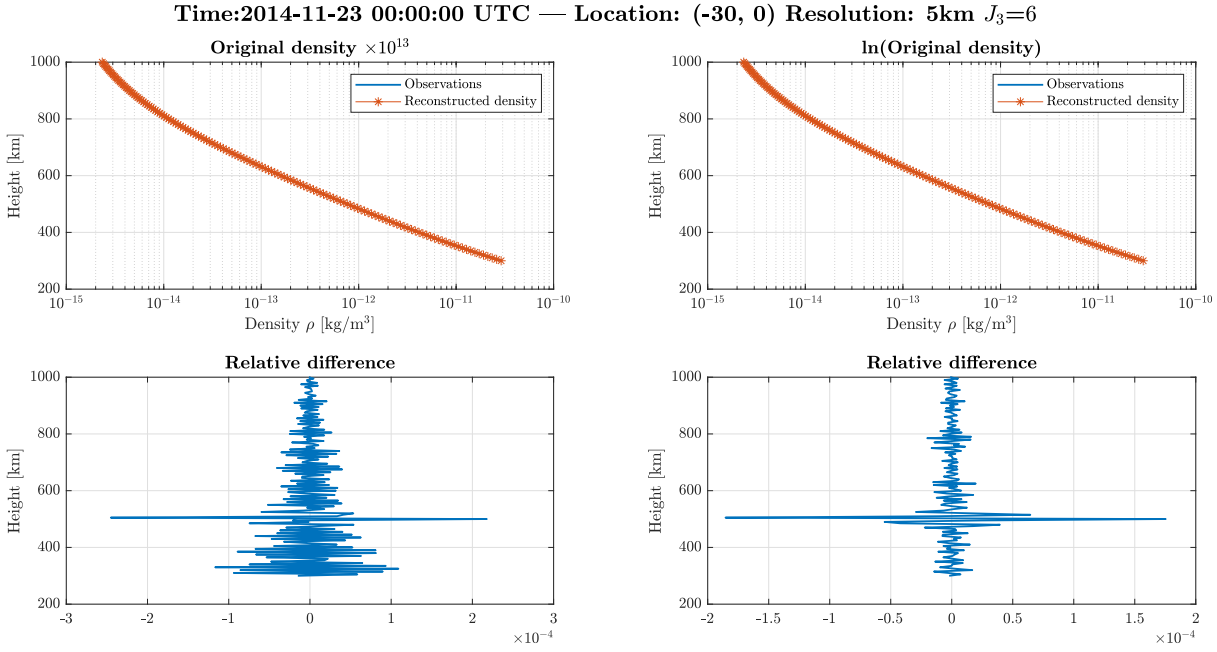

Figure 6.9: The 1-D thermospheric density with the resolution of 5 km as a function of altitude derived from the NRLMSISE-00 model and reconstructed from B-spline modeling with the resolution level of $J_3 = 6$ at (-30°, 0°) at 00:00:00 on 23/11/2014.

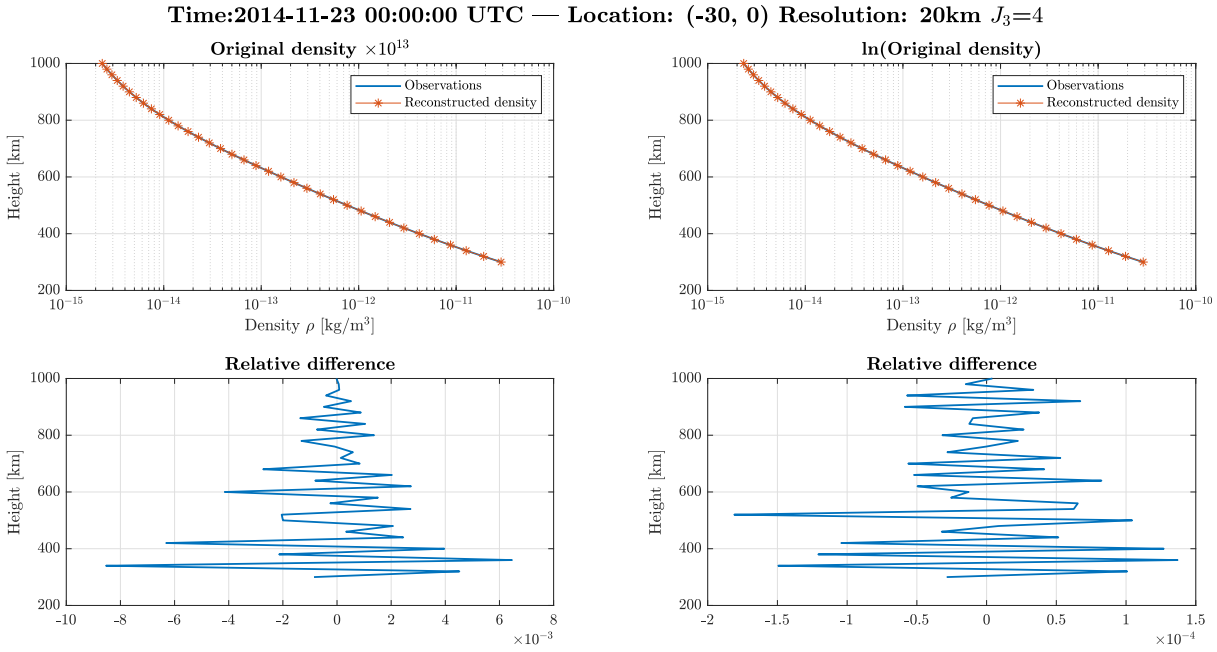

Figure 6.10: The 1-D thermospheric density with the resolution of 20 km as a function of altitude derived from the NRLMSISE-00 model and reconstructed from B-spline modeling with the resolution level of $J_3 = 4$ at (-30°, 0°) at 00:00:00 on 23/11/2014.

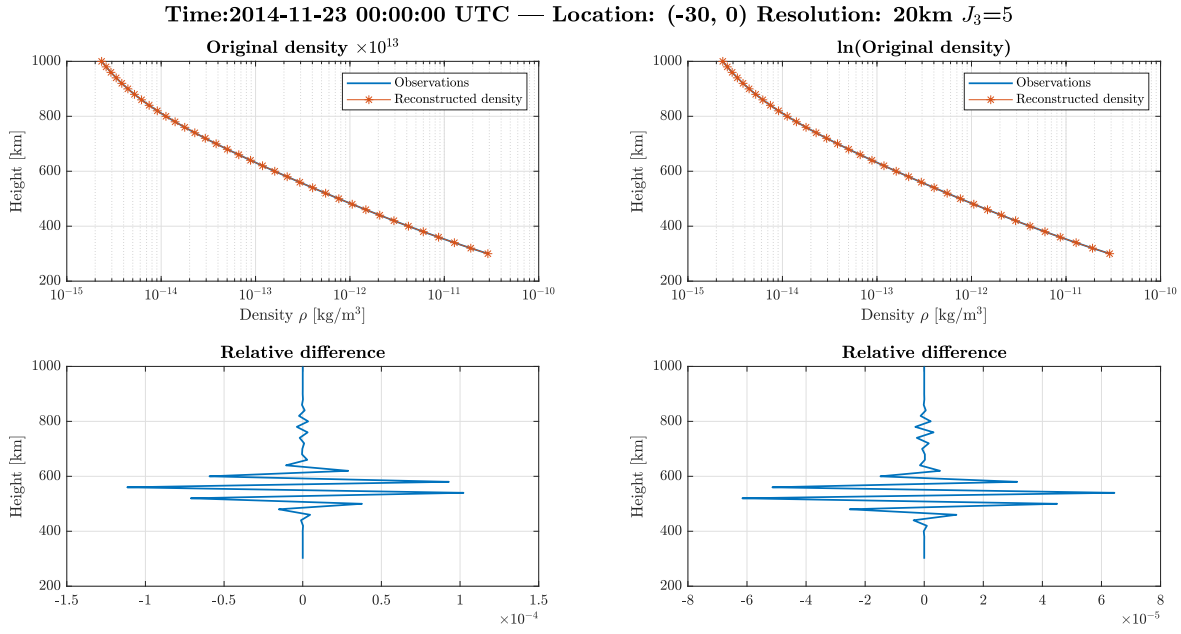

Figure 6.11: The 1-D thermospheric density with the resolution of 20 km as a function of altitude derived from the NRLMSISE-00 model and reconstructed from B-spline modeling with the resolution level of $J_3 = 5$ at (-30°, 0°) at 00:00:00 on 23/11/2014.

6.2 Two-dimensional B-spline modeling

In this section, the thermospheric density grids at 300-1000 km with the interval of 20 km are transformed into a set of B-spline coefficients which are performed individually at each discrete altitude. The following presents some examples of 2-D modeling in terms of B-spline coefficients, reconstructed neutral densities, and the related assessment of them.

Figure 6.12 presents the global thermospheric densities at 500 km at a specific epoch derived from empirical NRLMSISE-00 model, with a spatial resolution of $2.5^\circ \times 5^\circ$ in latitude and longitude. It can be seen that the neutral densities in nearly half areas are more closed to the lower end of the colorbar with the smallest density value concentrated in the Middle East area and the highest peak located in the Pacific ocean. Compared to the northern hemisphere, the density along longitude in the southern hemisphere varies more frequently, which is apparently determined by the time epoch the map is presenting. Figure 6.13 containing 9 subfigures shows the temporal change of spatial distribution of thermospheric densities within one day. Obviously, all the subfigures maintain similar spatial patterns but shift from east to west continuously from one midnight to the next midnight. The 2-D B-spline transformation is performed taking observations in Fig. 6.12 as an example. Totally, there are density grids with the number of $73 \cdot 73$ in the original density map. The grid points at -180°, however, share the same values with those at 180° in longitude due to the global characteristic of the earth, thus, $73 \cdot 72$ grid points, are in principle involved in the estimation of B-spline coefficients. According to Eqs. (4.7) and (4.15), the highest levels one can select for polynomial and trigonometric B-splines are set to $J_1 = 6$, $J_2 = 4$, respectively. Amongst those combinations of J_1 and J_2, 4 and 3 are the compromises between the resolution of neutral densities modeled by B-splines and the computational time in latitude and longitude dependency. In addition, the input observations used for parameter estimation shown in Fig. 6.12 are multiplied by 10^{12} which is the corresponding order of neutral densities at 500 km. And the pre-processed density values are used as observations for estimating B-spline coefficients in the adjustment. In order to guarantee the correctness of the final results, the estimated B-spline coefficients, and reconstructed neutral densities are multiplied by 10^{-12} after the adjustment.

Following the modeling approach described in Section 4.2.1, B-spline coefficients are estimated from original neutral densities using 2-D tensor products, which is illustrated as a global map in Fig. 6.14. 18 polynomial B-splines and 24 trigonometric B-splines are calculated in latitudinal direction and longitudinal direction, representing 18 and 24 B-spline coefficients, respectively. The distribution pattern of estimated coefficients is extremely close to that of original thermospheric densities, which is consistent with the expectation since the tensor product itself does not depend on the observation variation but exclusively depends on the location of the observation and B-spline-related parameters such as resolution level, restriction range. Moreover, the magnitudes of unknown coefficients in Fig. 6.14 are same with those of neutral densities in Fig. 6.12 because the magnitudes of the tensor product are below 1. As a consequence, it can be concluded that the variations of thermospheric densities dependent on latitude and longitude are reflected by changes in B-spline coefficients.

Since the 2-D B-spline modeling can be regarded as a linear adjustment system, the reconstructed neutral densities which have the same spatial resolution as the original observations can be easily computed from the tensor products used for unknowns estimation and estimated B-spline coefficients by multiplication of them. In Fig. 6.15 which presents reconstructed densities, it can be seen that there are no obvious differences between reconstructed ones and

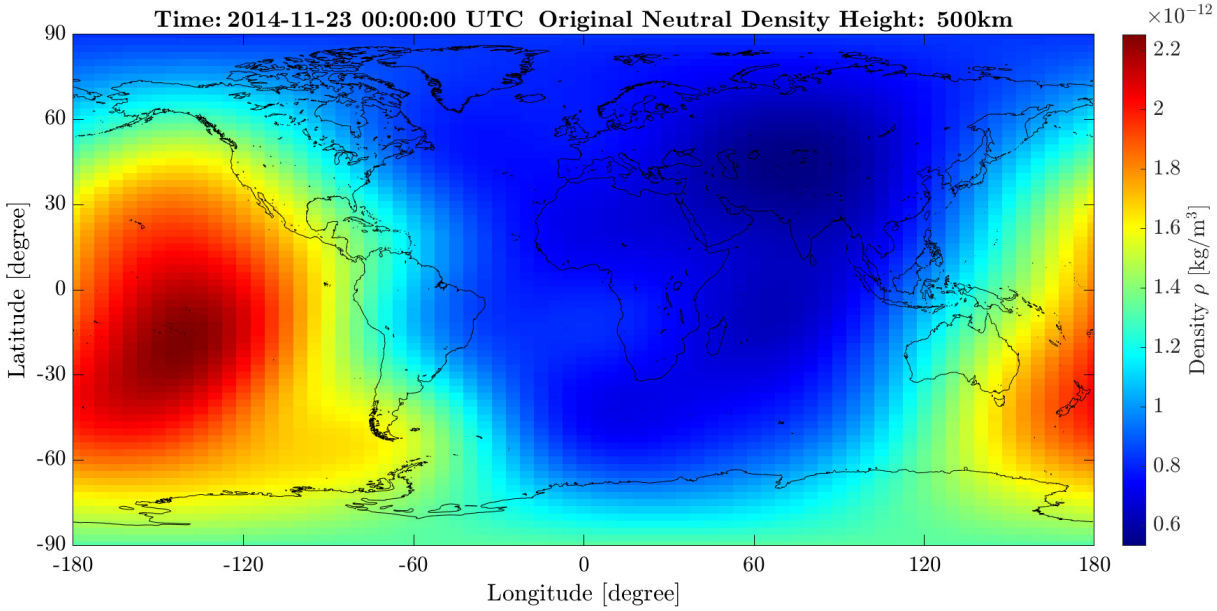

Figure 6.12: The global map presenting original neutral densities derived from the empirical NRLMSISE-00 model at 500 km at 00:00:00 on 23/11/2014 in 2-D modeling.

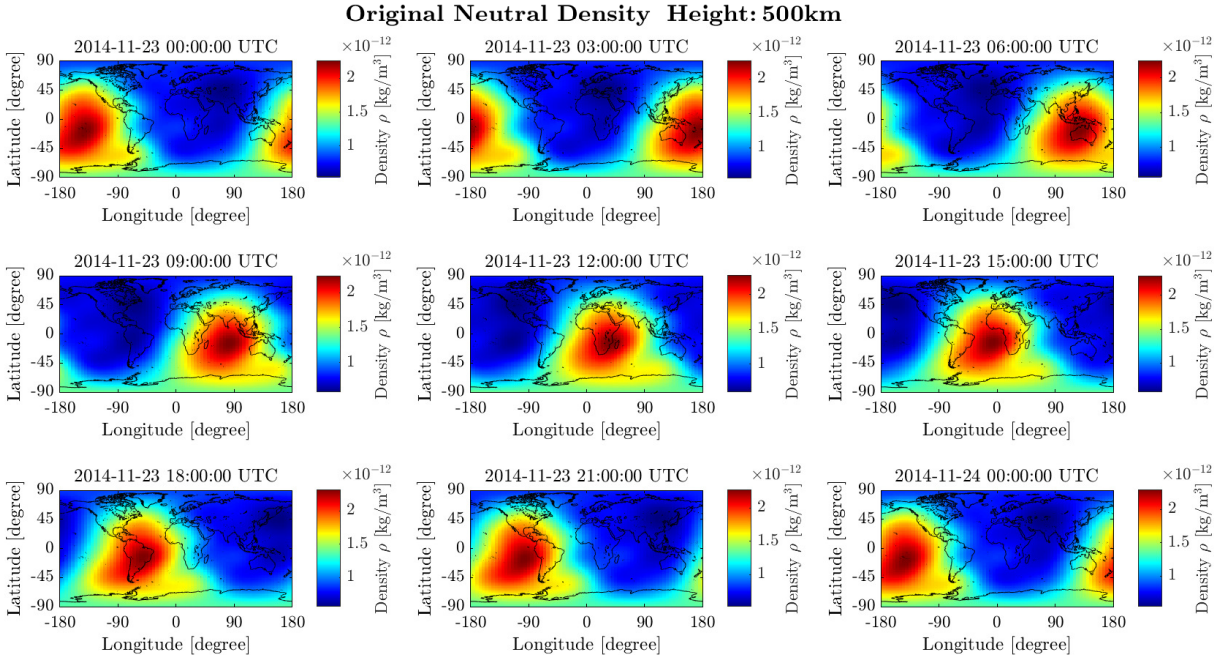

Figure 6.13: The global maps presenting original neutral densities derived from the empirical NRLMSISE-00 model at 500 km between 00:00:00 on 23/11/2014 and 00:00:00 on 24/11/2014.

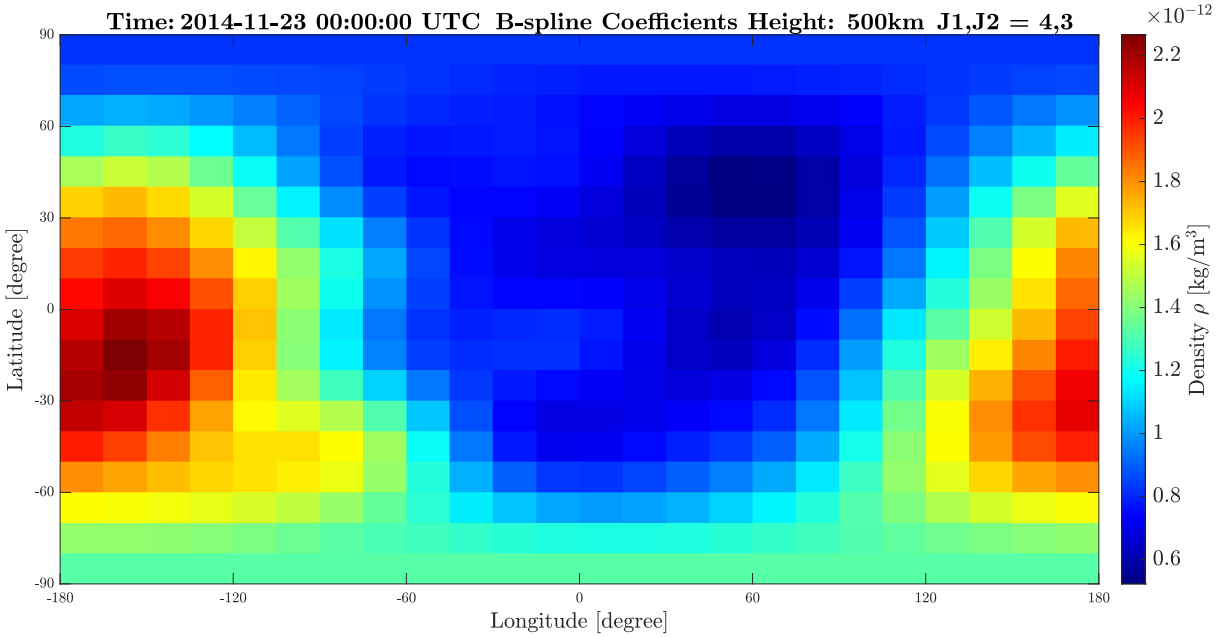

Figure 6.14: The global map presenting B-spline coefficients estimated from original neutral densities with resolution levels $J_1 = 4$, $J_2 = 3$ in latitude and longitude at 500 km at 00:00:00 on 23/11/2014 in 2-D modeling.

original ones in Fig. 6.12 visible. Therefore, the differences between them, i.e. the reconstructed minus the original, are plotted in Fig. 6.16. Besides the green color meaning nearly zero difference which accounts for a large part of the map, the chess-like structure composed of values close to the peak (red) and those close to the bottom (blue) of the colorbar can be observed in Fig. 6.16, in particular in the southern region of South America. It is a common structure observed in the difference maps of B-spline representation which is determined by the characteristics of B-splines themselves. As known, the global 2-D tensor product results in a pattern of 3-dimensional knobs instead of completely flat, and there is an overlay region between adjacent B-splines, which can cause the underestimation or overestimation of B-spline coefficients at a specific grid point. As a consequence, the differences between reconstructed data and original data result in a chess-like pattern composed of red and blue colors. Nevertheless, the region where this special pattern appears depends on the input observations but not on the geographical locations.

Furthermore, the relative differences between the estimated neutral densities and the original ones are helpful for assessing the deviations of neutral densities represented by B-splines and those derived directly from the empirical NRLMSISE-00 model. Fig. 6.17 shows the maximum relative difference value is around $1.3 \cdot 10^{-3}$, and the chess-like structure is more visible.

In terms of stochasticity of the B-spline adjustment system, the STDs of B-spline coefficients and estimated thermospheric densities are computed and illustrated in Figs. 6.18 and 6.19, respectively. Consistent with the weighting strategy used in the adjustment system, the STDs of estimated coefficients and reconstructed densities are latitude-dependent as well, and the values are symmetric with respect to the equator decreasing from high latitude to low latitude. In Fig. 6.18, the STDs are completely longitude independent, and they are 4-order smaller than the magnitude of estimated unknown coefficients in Fig. 6.14, from which one can consider the precision of unknowns estimation reaches up to the level usually found in numerical investigations. Whereas the STDs of reconstructed neutral densities in Fig. 6.19 distribute

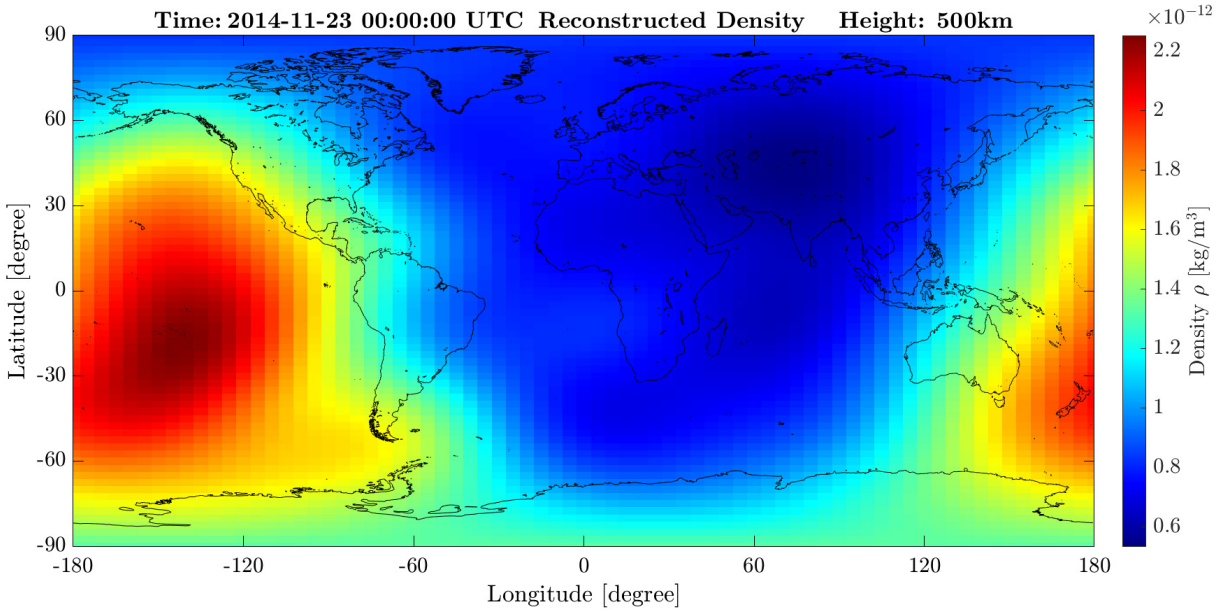

Figure 6.15: The global map presenting neutral densities reconstructed from B-spline coefficients at 500 km at 00:00:00 on 23/11/2014 in 2-D modeling.

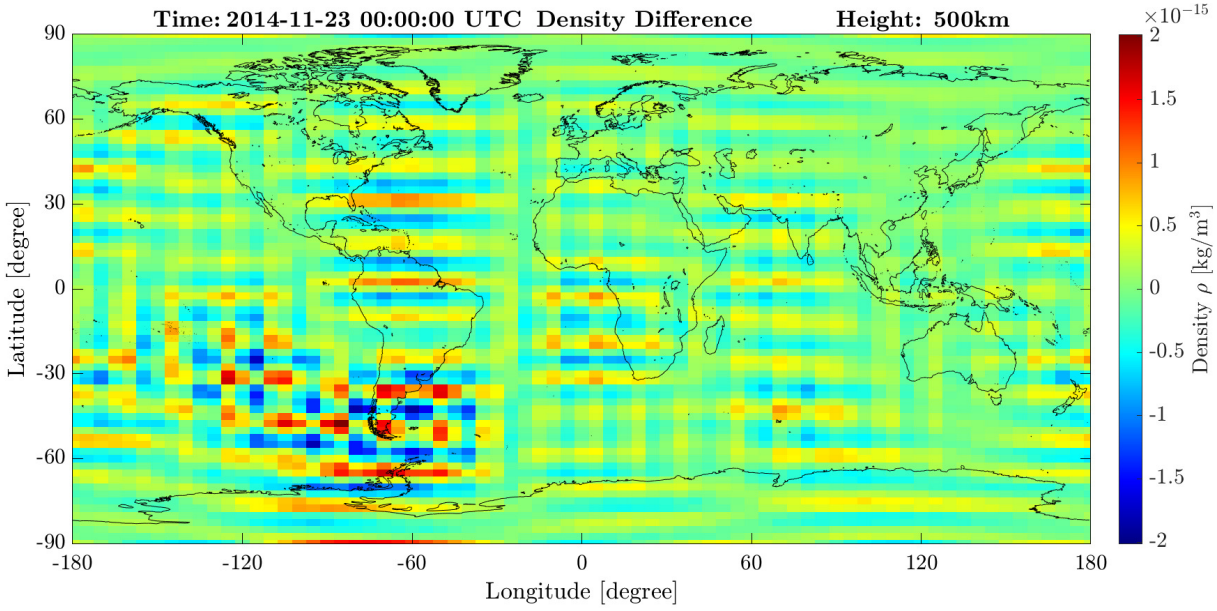

Figure 6.16: The global map presenting differences between neutral densities reconstructed from B-spline coefficients and original densities at 500 km at 00:00:00 on 23/11/2014 in 2-D modeling.

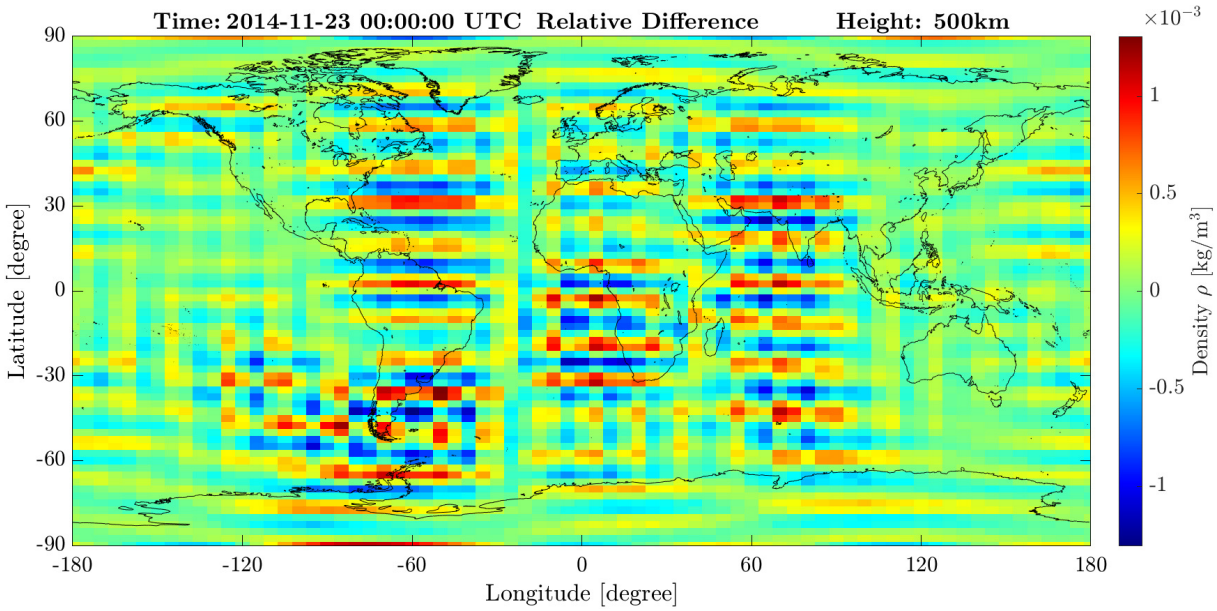

Figure 6.17: The global map presenting relative differences between neutral densities reconstructed from B-spline coefficients and original densities at 500 km at 00:00:00 on 23/11/2014 in 2-D modeling.

as a grid pattern. On one hand, the STDs of estimated densities are latitude-dependent as well with the same variation trend as STDs of B-spline coefficients. On the other hand, the STD values in Fig. 6.19 are longitude dependent regularly, in other words, there are constant STD values at one specific latitude with smaller values at some specific locations, which is determined by the structure of B-splines.

It is interesting to investigate the precision information derived in 2-D modeling at different altitudes. Due to the lack of satellites below 300 km, we only select the altitudes of 300-100 km as the investigation range in this study. For convenience, Figs. 6.20 and 6.21 only show the STDs of unknown coefficients and reconstructed thermospheric densities derived from individual 2-D B-spline representation at each 100 km. It can be seen that the STD values at all heights present the same distribution as analyzed above, but with the exponential decaying order from 10^{-14} to 10^{-18} as the height increases. This is because the original observations have the decreasing density values with increasing height, resulting in smaller differences between reconstructed neutral densities and original densities derived from the NRLMSISE-00 model. Consequently, the modeling results at higher altitudes have the smaller posterior unit standard deviation and thus, smaller STD values.

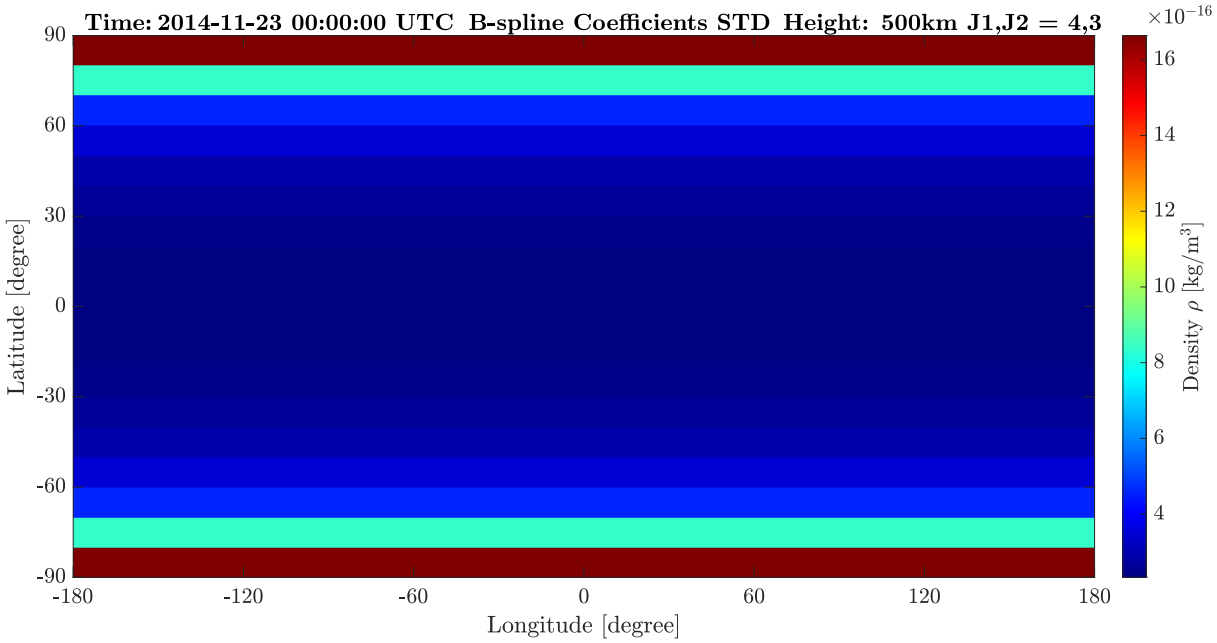

Figure 6.18: The global map presenting STDs of B-spline coefficients estimated from original neutral densities with resolution levels $J_1 = 4$, $J_2 = 3$ in latitude and longitude at 500 km at 00:00:00 on 23/11/2014 in 2-D modeling.

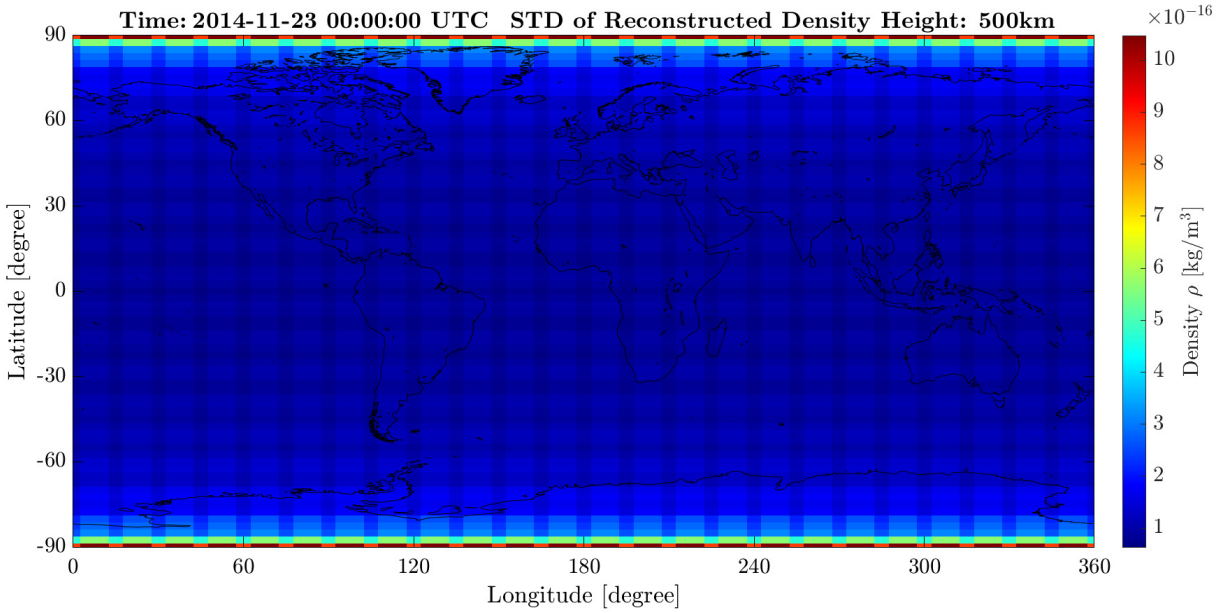

Figure 6.19: The global map presenting STDs of neutral densities reconstructed from B-spline coefficients at 500 km at 00:00:00 on 23/11/2014 in 2-D modeling.

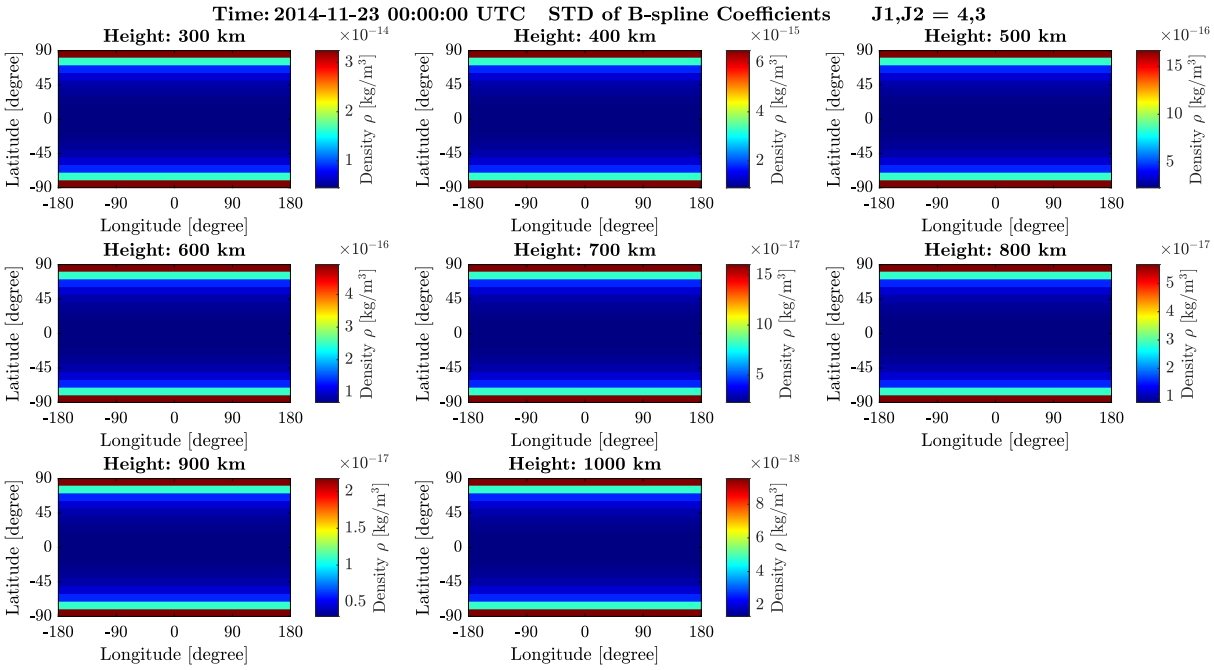

Figure 6.20: The global map presenting STDs of B-spline coefficients estimated from original neutral densities with resolution levels $J_1 = 4$, $J_2 = 3$ in latitude and longitude at 300-1000 km at 00:00:00 on 23/11/2014 in 2-D modeling.

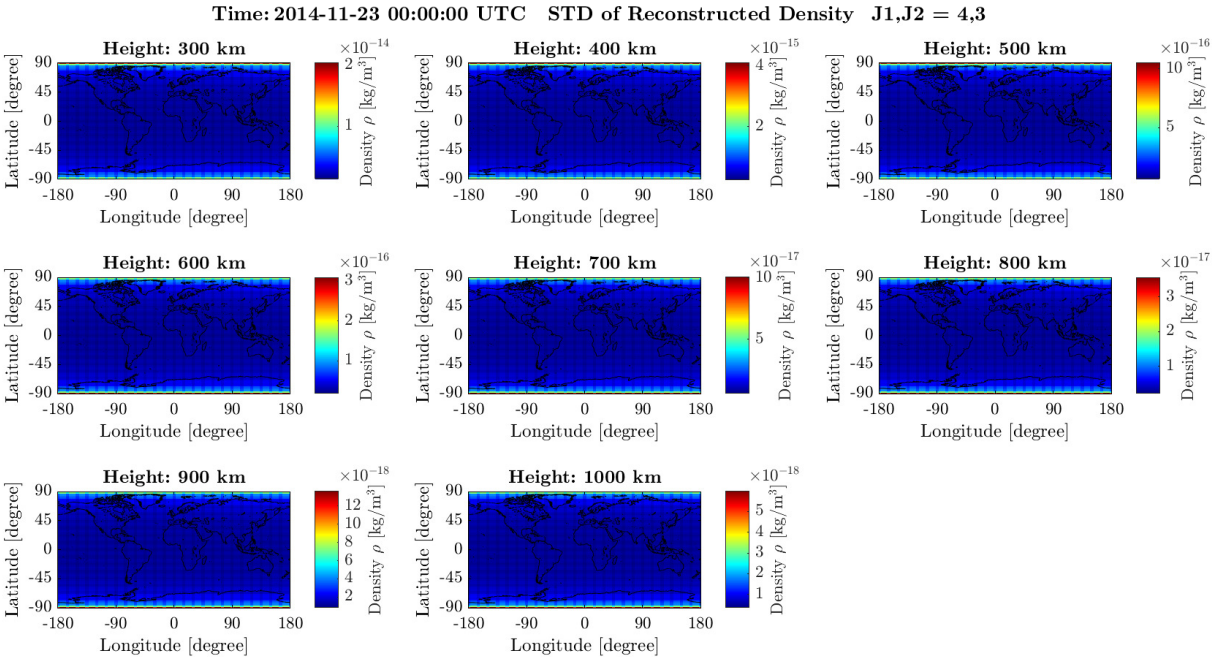

Figure 6.21: The global map presenting STDs of neutral densities reconstructed from B-spline coefficients at 300-1000 km at 00:00:00 on 23/11/2014 in 2-D modeling.

Additionally, it is worth checking the computational time needed for 2-D B-spline transformation. Since the design matrix involved in 2-D adjustment becomes completely the same if the original densities have the same spatial range and resolution, which is exactly the condition in this study, i.e., all the original thermospheric densities at all altitudes and at any epoch have the same resolution of $2.5^\circ \times 5^\circ$, the generation of 2-D B-spline products can share one design matrix $\mathbf{A}$. For the generation of 2-D tensor product matrix $\mathbf{A}$, it takes around 30 s; And for the estimation of B-spline coefficients and the computation of relative precision, it takes around 15 s for one set of observations. Therefore, taking producing 1-week products including B-spline coefficients, reconstructed neutral densities, and STDs of them at each 5 min and at each 20 km as an example, almost one-day time is needed. The products covering a period of time can be presented in the format of a video to not only show the product itself but also show changes in products over time.

Nevertheless, what we discussed above is the case that the reconstructed neutral densities maintain the same grids as the original observations, that is, they have the same spatial resolution. However, one of the most important characteristics of B-spline modeling is that the inhomogeneous data can be dealt with, which means the neutral density at any specific grid point can be computed once the B-spline coefficients have been computed in one model. Therefore, a new thermospheric density map at 500 km but with a different spatial resolution can be generated. In this case, B-spline basis functions are needed to compute the new tensor product. By multiplying the new tensor product with the estimated B-spline coefficients, the thermospheric density grid with the different resolution is computed. Fig. 6.22 shows the thermospheric density grid with the spatial resolution of $2^\circ \times 2^\circ$ using B-spline coefficients shown in Fig. 6.14.

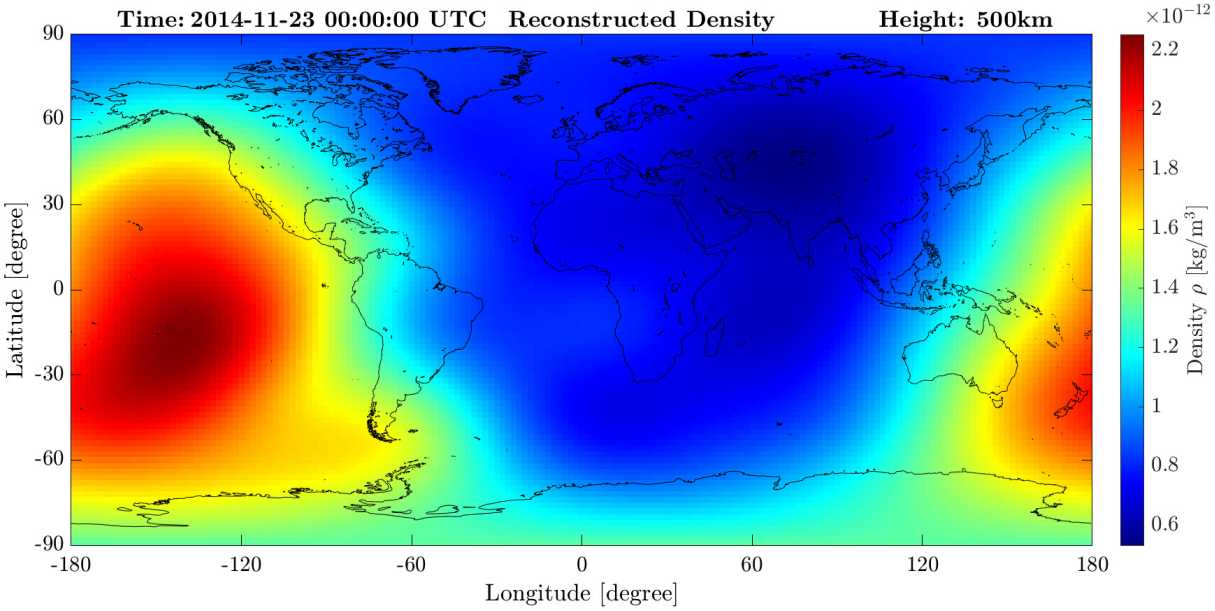

Figure 6.22: The global map presenting neutral densities reconstructed from B-spline coefficients with the resolution of $2^\circ \times 2^\circ$ at 500 km at 00:00:00 on 23/11/2014 in 2-D modeling.

It has been known that the original thermospheric densities derived from the NRLMSISE-00 model are considered error-free, thus, the superposition of random noise can be used for studying the impact of noise on B-spline modeling results. The thermospheric densities at 500 km at 00:00:00 on 23/11/2014 are still taken as an example. In Fig. 6.23, the 5% random noise is superposed into the original neutral densities derived from the empirical model.

By the same approach, the B-spline coefficients are estimated and illustrated in Fig. 6.22. Afterwards, the new thermospheric densities are reconstructed and presented in Fig. 6.24. The differences between the reconstructed densities and original densities are illustrated in Fig. 6.25, where it can be seen most of difference values is close to zero with the largest value of $2.2 \cdot 10^{-13}$. However, the largest difference is approximately equal to 10% of input observations instead of 5%. This is because a set of random numbers are generated according to Gaussian distribution with 5% of input observations as the expectation. Consequently, the maximum noise superposed into the input observations reaches 10%, which is the reason why the ends of colorbar in Fig. 6.25 reach 10% of input observations. It can be concluded that the amount of noise superimposed into the input observations is reflected by the final differences between B-spline-represented thermospheric densities and noised observations.

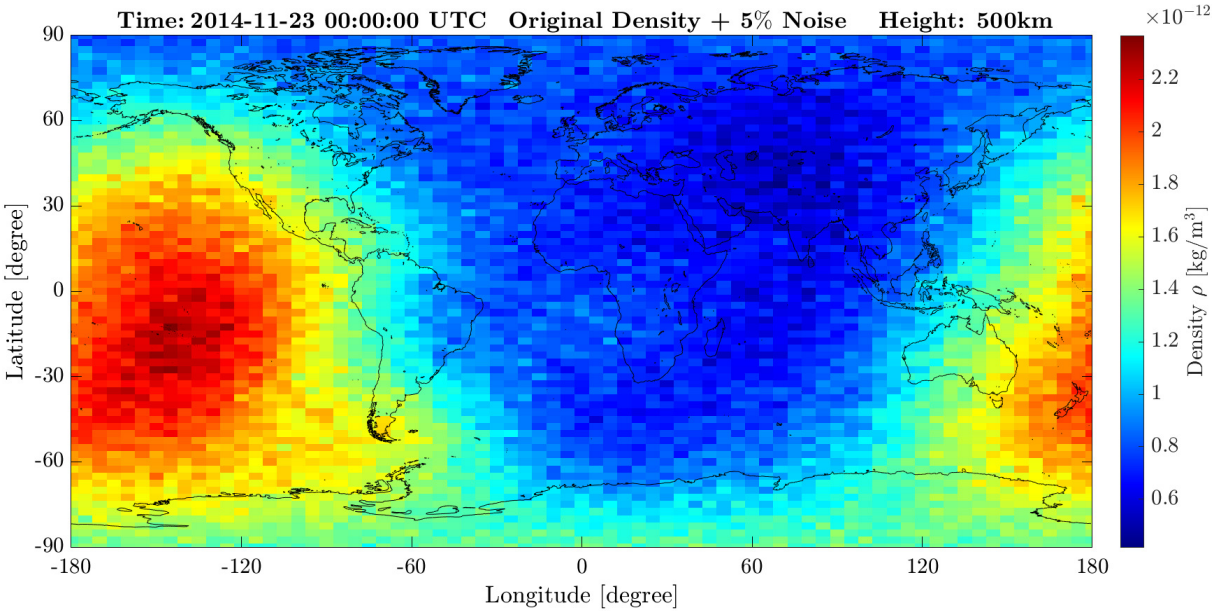

Figure 6.23: The global map presenting original neutral densities derived from the empirical NRLMSISE-00 model with 5% noise at 500 km at 00:00:00 on 23/11/2014 in 2-D modeling.

6.3 Three-dimensional B-spline modeling

In this section, the thermospheric densities with multi-layers in height dependency at a specific epoch are transformed into a set of B-spline coefficients by 3-D B-spline modeling. The logarithmic model of thermospheric density is used because it can model the exponential distribution along the height more accurately, which has been proved in Section 6.1.3. Therefore, the corresponding logarithmic numbers of thermospheric observations are involved in the linear squares adjustment but with the different tensor product as that in 2-D case.

In 3-D B-spline modeling, the selection of resolution level and observation interval dependent on height is a serious question, since it directly determines the accuracy of height-dependent profile modeling. A small test in Section 6.1.3 helps to solve this problem. The conclusion is, that the resolution level for modeling height-dependent profile is selected as 4, and the levels of B-splines in latitude and longitude maintain as 4 and 3. With respect to the resolution of observations, 20 km is decided due to the more accurate result, and the spatial resolution of $2.5^\circ \times 5^\circ$ is still assigned to observations at each layer. Still, the epoch 00:00:00 on 23/11/2014

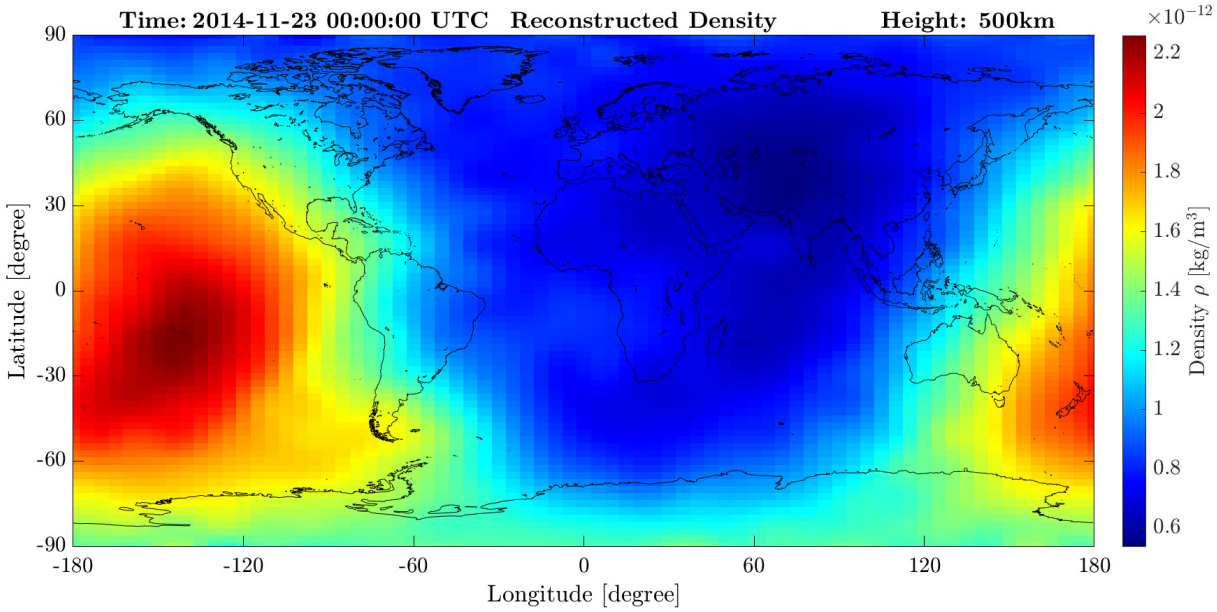

Figure 6.24: The global map presenting neutral densities reconstructed using noised original densities at 500 km at 00:00:00 on 23/11/2014 in 2-D modeling.

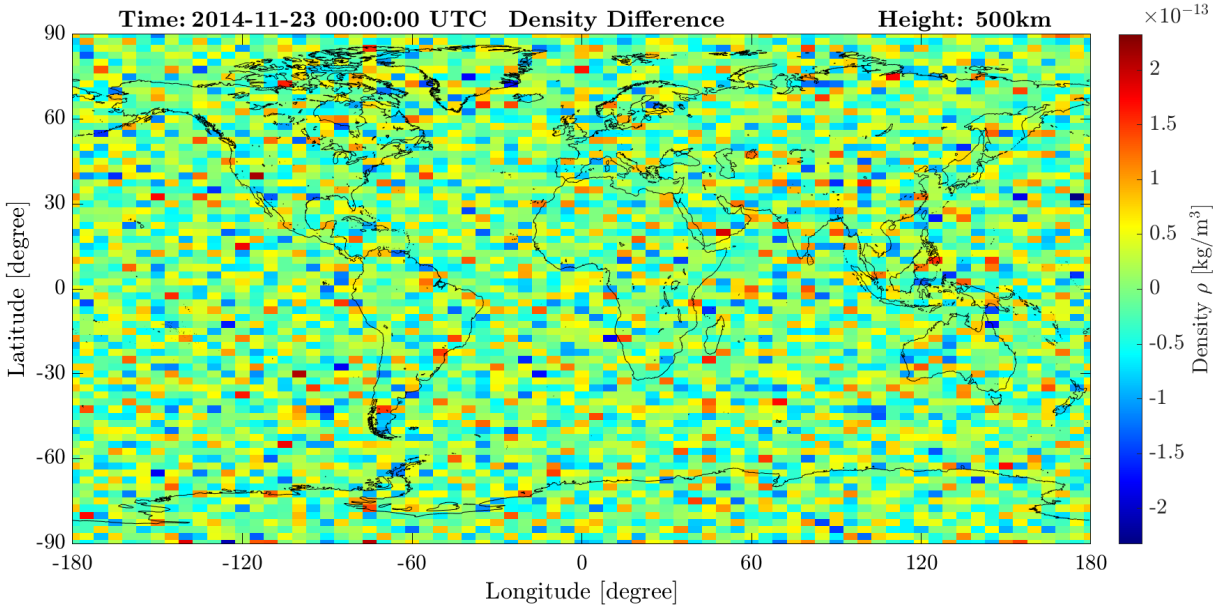

Figure 6.25: The global map presenting differences between neutral densities reconstructed from B-spline coefficients and original densities with 5% noise at 500 km at 00:00:00 on 23/11/2014 in 2-D modeling.

is taken as the example to show the modeling result in 3-D case. Fig. 6.26 presents the part of observations at 00:00:00 on 23/11/2014 used for 3-D B-spline representation due to the limitation of the figure space. Nevertheless, the estimated B-spline coefficients in the static 3-D case are arranged and exhibited in the form of multi-maps that corresponds to different altitudes of B-splines in height dependency as shown in Fig. 6.27. There is no simple correspondence between original observations in Fig. 6.26 and the estimated B-spline coefficients in terms of height due to the different intervals among B-splines, which is different from 2-D modeling in which the map presenting B-spline coefficients and the map of observations have one-to-one correspondence. Therefore, all the B-spline coefficients derived in the static 3-D modeling are supposed to be used to estimate the reconstructed density at any position. Similarly, all the neutral densities with the same positions as original observations are computed and illustrated in Fig. 6.28.

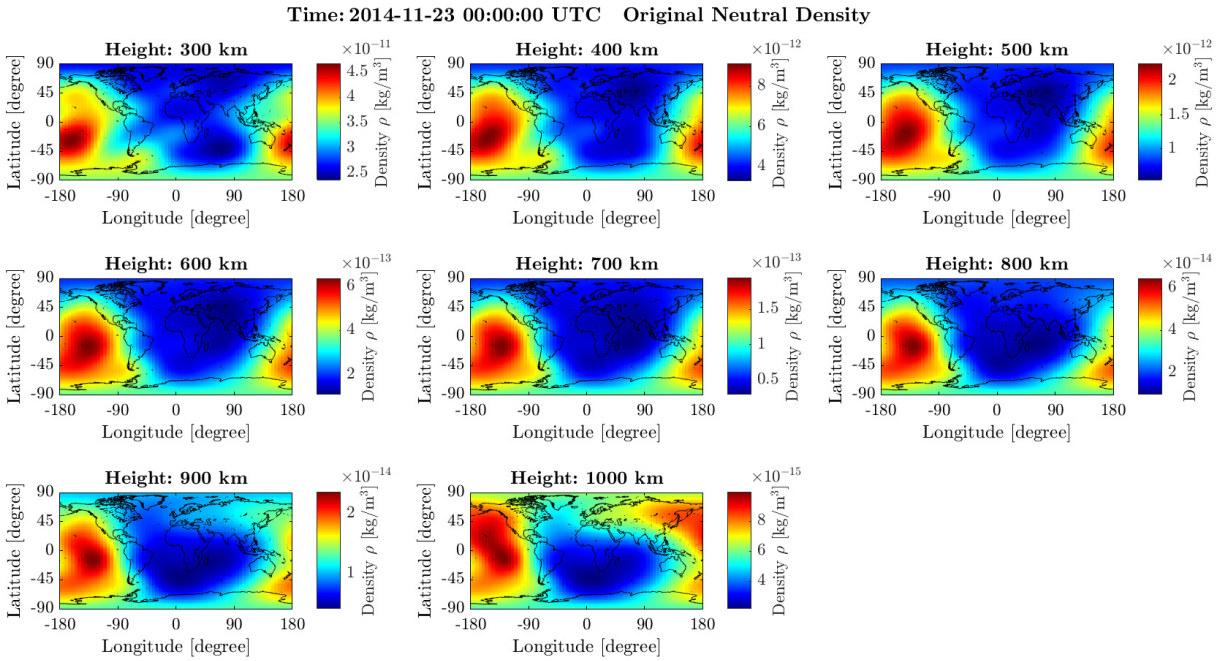

Figure 6.26: The global map presenting original neutral densities derived from the empirical NRLMSISE-00 model at 300-1000 km at 00:00:00 on 23/11/2014 in 3-D modeling.

In Fig. 6.29 which shows the differences between the neutral densities reconstructed from estimated B-spline coefficients (Fig. 6.28) and the original densities at different altitudes. It can be seen that most of difference values are close to zero and show the characteristic of randomness. With the increase of altitude, the difference values are changing smaller which is consistent with the trend in 2-D modeling.

Again, it is meaningful to compute the relative differences between neutral densities estimated from 3-D B-spline modeling and original densities as observations, which can be used for the comparison of performance between 3-D and 2-D, since products of them have the same height interval between 300 km and 1000 km. As can be seen in Fig. 6.30, the relative differences at all altitudes (also including those not shown in the figure) are at the level of 10^{-3}. Compared with the result at 500 km shown in Fig. 6.17 where the relative differences ranging from -1.3^{-3} to 1.3^{-3} are derived in the individual B-spline modeling at 500 km, the result at the same altitude but derived by 3-D representation has larger relative differences. The same condition can also be observed in products at other altitudes. This is because more constraints are applied in 3-D modeling, that is, B-splines along latitude, longitude and height together represent

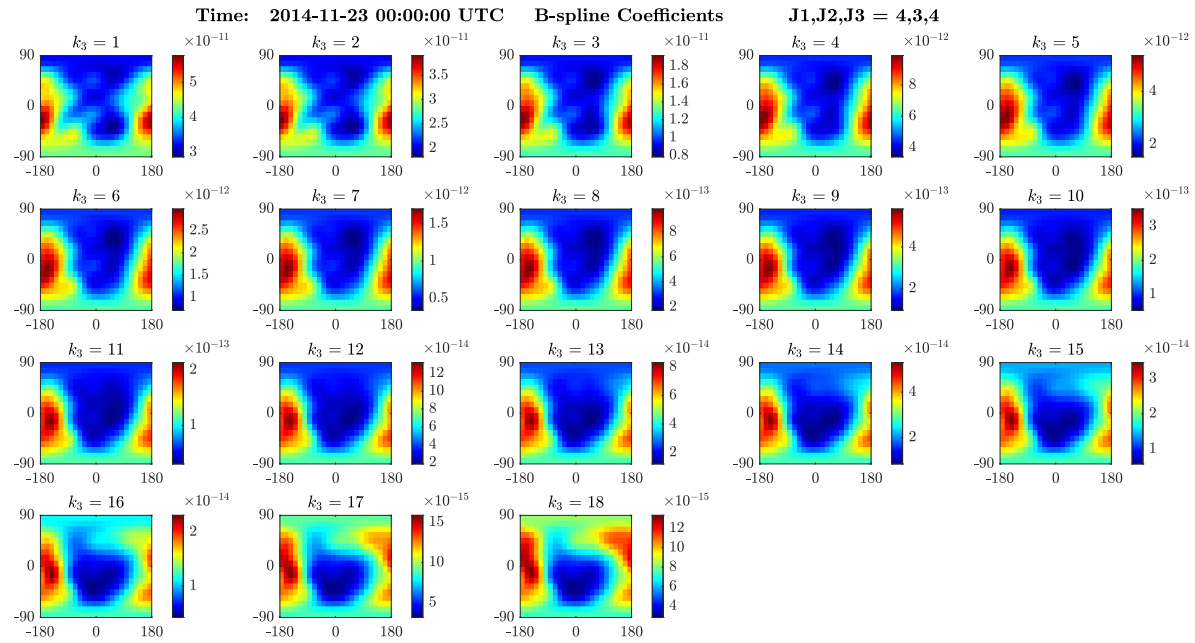

Figure 6.27: The global maps presenting B-spline coefficients estimated from original neutral densities with resolution levels $J_1 = 4$, $J_2 = 3$, $J_3 = 4$ in latitude, longitude, and height at 00:00:00 on 23/11/2014 in 3-D modeling.

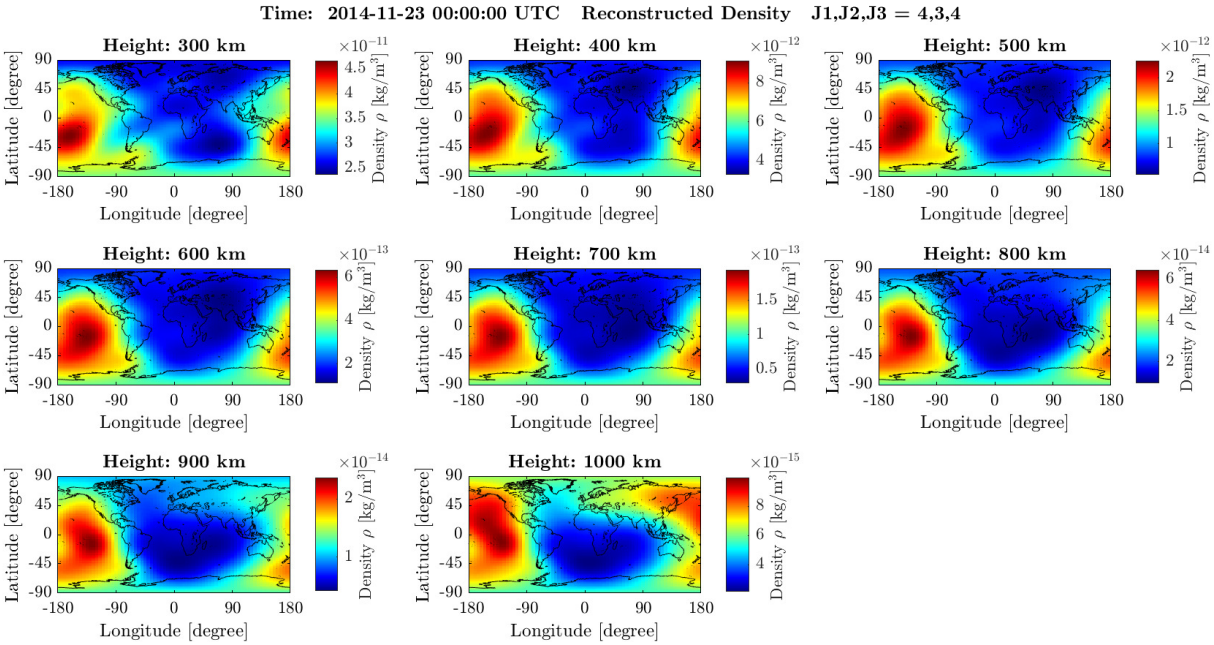

Figure 6.28: The global map presenting neutral densities reconstructed from B-spline coefficients at 300-1000 km at 00:00:00 on 23/11/2014 in 3-D modeling.

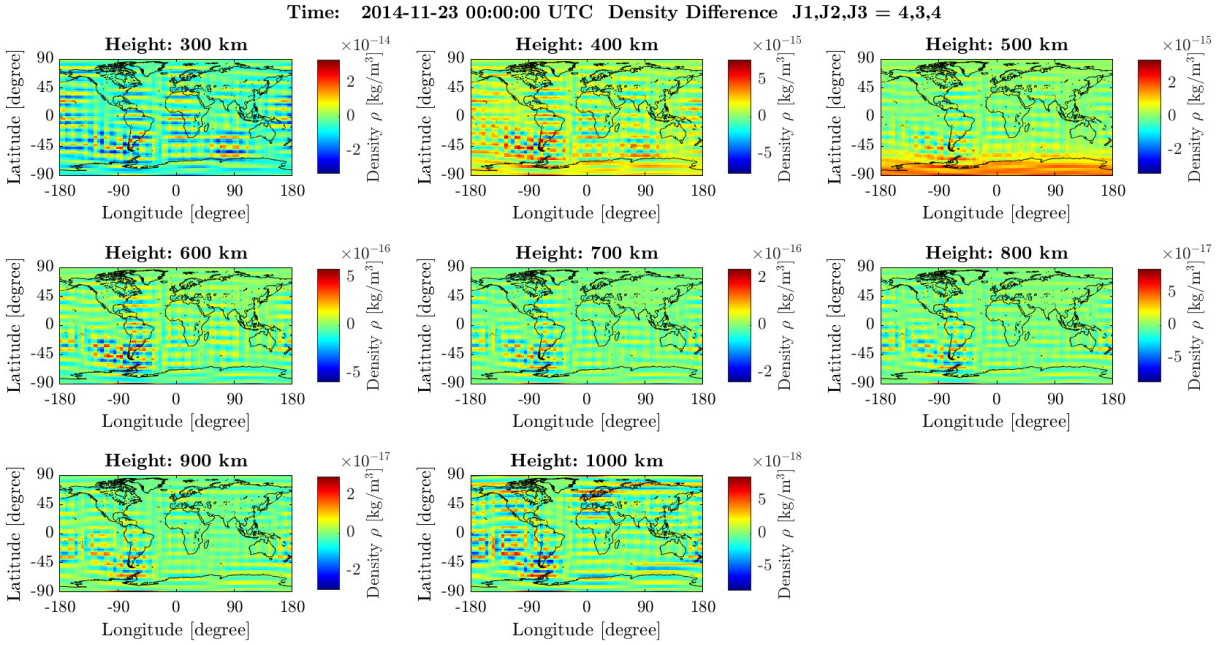

Figure 6.29: The global maps presenting differences between neutral densities reconstructed from B-spline coefficients and original densities at 300-1000 km at 00:00:00 on 23/11/2014 in 3-D modeling.

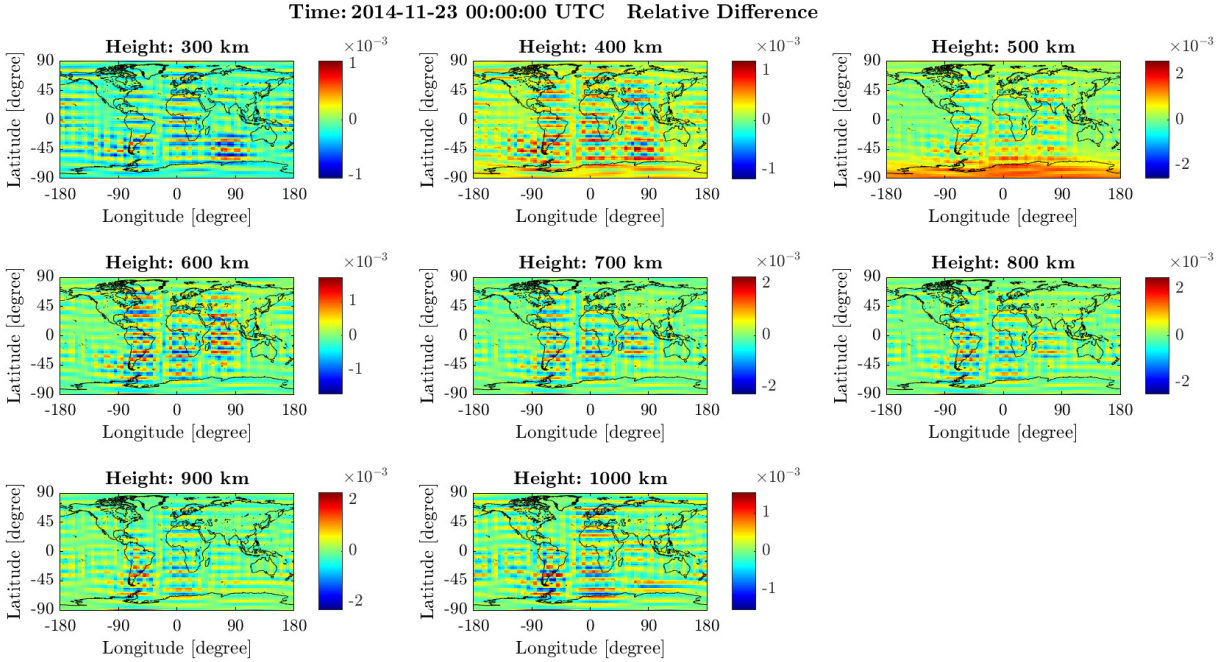

Figure 6.30: The global maps presenting relative differences between neutral densities reconstructed from B-spline coefficients and original densities at 300-1000 km at 00:00:00 on 23/11/2014 in 3-D modeling.

variations of thermospheric density. Therefore, it is difficult to reach the same accuracy as the modeling in the horizontal plane in 3-D modeling due to the additional constraints in height dependency.

When it comes to the standard deviations of estimated B-spline coefficients and of reconstructed neutral densities, they are presented as the format of maps in Figs. 6.31 and 6.32. There are in total 18 maps representing $k_3 = 1, 2, ..., 18$ to show STD values of B-spline coefficients ranging from 10^{-15} to 10^{-18}, which means the STD values decrease with respect to the increase of height. For each layer, the STD values are completely latitude-dependent reducing from high-latitude to low-latitude, which is consistent with the distribution in 2-D case. In addition, the orders of STD values decrease exponentially, which can be influenced by the weighting matrix applied in the adjustment. In other words, the setup of weighting matrix in3-D modeling in particular dependent on height has an impact on the values of STD of estimated unknowns and thermospheric densities. And for the STDs of estimated densities, they distribute latitude-dependent and longitude-dependent, which is also similar to that in the result of 2-D modeling.

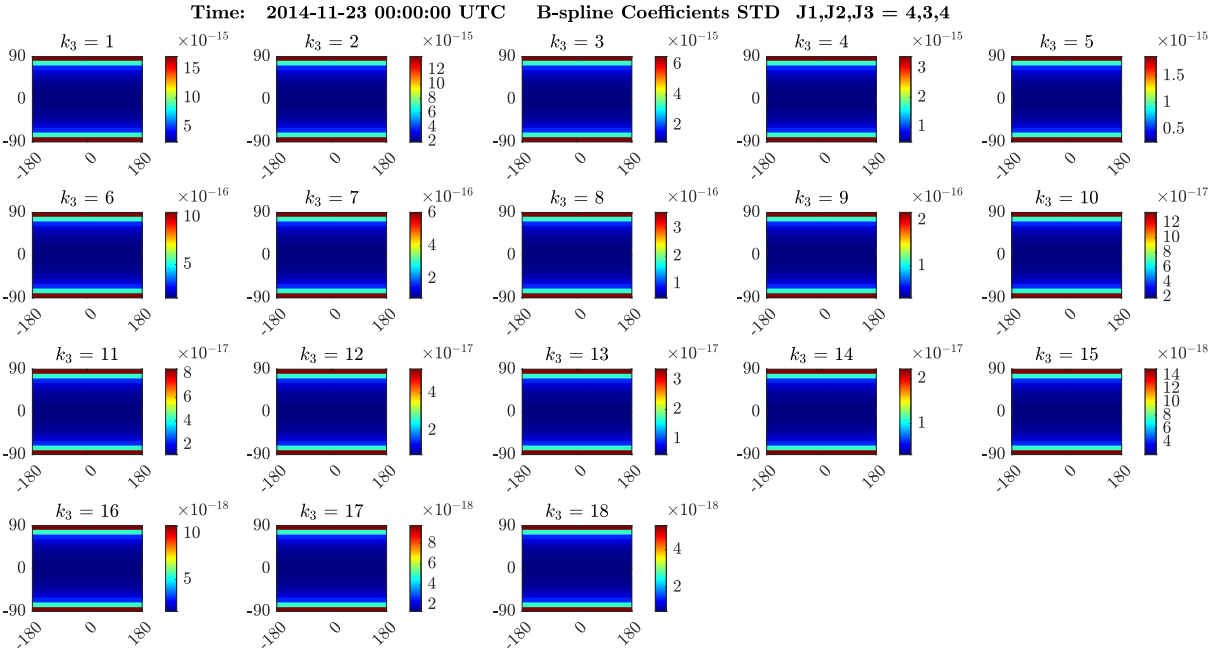

Figure 6.31: The global maps presenting STDs of B-spline coefficients estimated from original neutral densities with resolution levels $J_1 = 4$, $J_2 = 3$, $J_3 = 4$ in latitude, longitude and height at 300-1000 km at 00:00:00 on 23/11/2014 in 3-D modeling.

However, when comparing the STDs of estimated B-spline coefficients and neutral densities in 3-D modeling with those in 2-D modeling, it can be found that the STD values derived from 3-D modeling are smaller than those from 2-D modeling by a factor of 2. This is because even if there are additional constraints along the height, the weighting factor as a function of height is computed based on the STD values derived in 2-D modeling. Specifically speaking, for a specific epoch, the average value of STD values with a specific altitude is computed so that a set of average values are acquired which are used for computing the weighting factor corresponding to each altitude. For example, the average STD at 500 km is a, then the weighting factor corresponding to 500 km used in 3-D modeling is $\frac{1}{a^2}$.

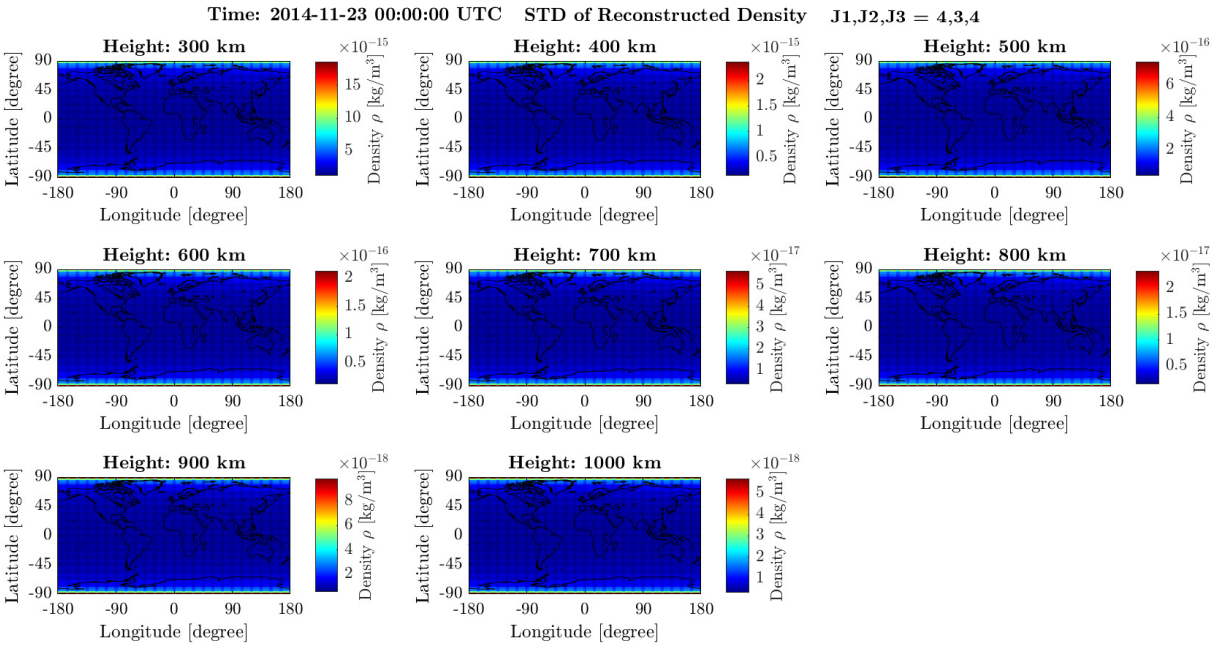

Figure 6.32: The global maps presenting STDs of neutral densities reconstructed from B-spline coefficients at 300-1000 km at 00:00:00 on 23/11/2014 in 3-D modeling.

As for the computational efficiency in 3-D B-spline transformation, it takes around 3 days to generate the global tensor product. And for the estimation of unknown coefficients and reconstructed thermospheric densities, it takes around 1 day to produce them covering a one-week data period.

6.4 Four-dimensional B-spline modeling

According to the analysis of "64 GPS-week data" in terms of the frequency spectrum, the shortest period that can be detected in Fourier analysis is 4h. Therefore, a sequence of 4-D B-spline models with the time interval of 1 h is appropriate to be modeled since 1 h is below the minimum repeating period and does not bring burden to the computational time. It means 13 time epochs are involved in the representation of one 4-D modeling with the time interval of 5 min. However, even if only a short term in the temporal dimension is added in the transformation with B-splines, it takes much longer time to generate the tensor product computed by four B-spline basis functions. The duration for generation of 4-D tensor product is too long to perform 4-D B-spline representation globally. The best solution is that we still keep the completeness of observation in height dependency because it is the most crucial part of thermosphere modeling. Nevertheless, the regional thermospheric densities are used as observations instead of global ones. In this study, the region with latitudes (-15°, 15°) and longitudes (30°, 90○) is selected and it still has the resolution of 2.5° × 5°. Therefore, there are $13 \cdot 13$ observations at a specific height and epoch.

The new issue is to choose the appropriate resolution level in the temporal dimension. 3 is the best one due to the number of time epochs involved in one 4-D B-spline modeling. For the height dependency, it remains at 4 as the resolution level, and the levels in latitude and longitude are adjusted to 3 and 3 due to the change of the modeling region. Besides, the

logarithmic model is used in 4-D modeling due to the involvement of height dimension in it.

Due to the limitation of thesis space, only the results at the first epoch in 4-D modeling are illustrated in the following. Figure 6.33 presents the input observations derived from NRLMSISE-00 model at different altitudes. It can be seen that the spatial distribution of thermospheric densities in this region differs from altitudes, which is likely to happen due to the contraction of the region compared to the global earth. The 4-D neutral densities are transformed into a series of B-spline coefficients, and obviously, the coefficients when $k_4 = 1$ correspond to the first epoch as shown in Fig. 6.34. Still, there are 18 subfigures corresponding to 18 B-splines along the height, from which and 4-D tensor product, the reconstructed neutral densities are estimated and shown in Fig. 6.35.

In Fig. 6.36 which shows the differences between reconstructed densities derived from 4-D modeling and original densities, the difference values range from 10^{-15} to 10^{-20}. Due to the regional characteristics, the difference values do not distribute completely randomly, and they are much smaller compared to values in 2-D and 3-D modeling. This is because the 4-D B-spline representation is performed within the context of regional modeling instead of global modeling, meaning fewer observations being constrained by similar number of B-splines, which consequently results in better accuracy for B-spline modeling. The relative differences shown in Fig. 6.37 also prove it with the level of 10^{-4} or 10^{-5}.

Furthermore, the standard deviations of B-spline coefficients and reconstructed neutral densities in 4-D modeling are presented in Figs. 6.38 and 6.39. It is worth mentioning, that the weighting matrix used in 4-D modeling is computed based on the average STD values concerning all the time epochs involved in one 4-D adjustment, which means the weighting matrix used for different observations is different. For the example presented in this study, the STD values of estimated B-spline coefficients and reconstructed densities decrease with the increasing height from 10^{-15} to 10^{-19}, which are smaller than values in 2-D and 3-D modeling due to the regional modeling. For STDs of estimated neutral densities, they have larger values at the edge of the region compared to the central zone. This is caused by the ”end-interpolating” characteristic of polynomial B-splines.

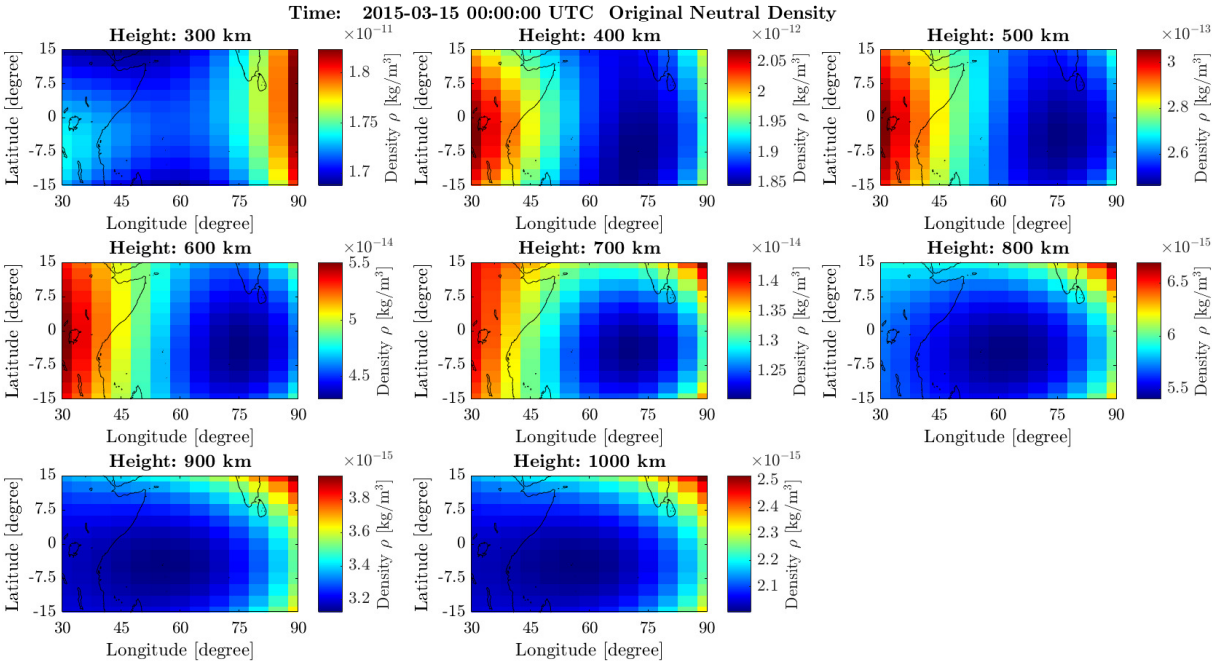

Figure 6.33: The regional map presenting original neutral densities derived from the empirical NRLMSISE-00 model at 300-1000 km at 00:00:00 on 15/03/2015 in 4-D modeling.

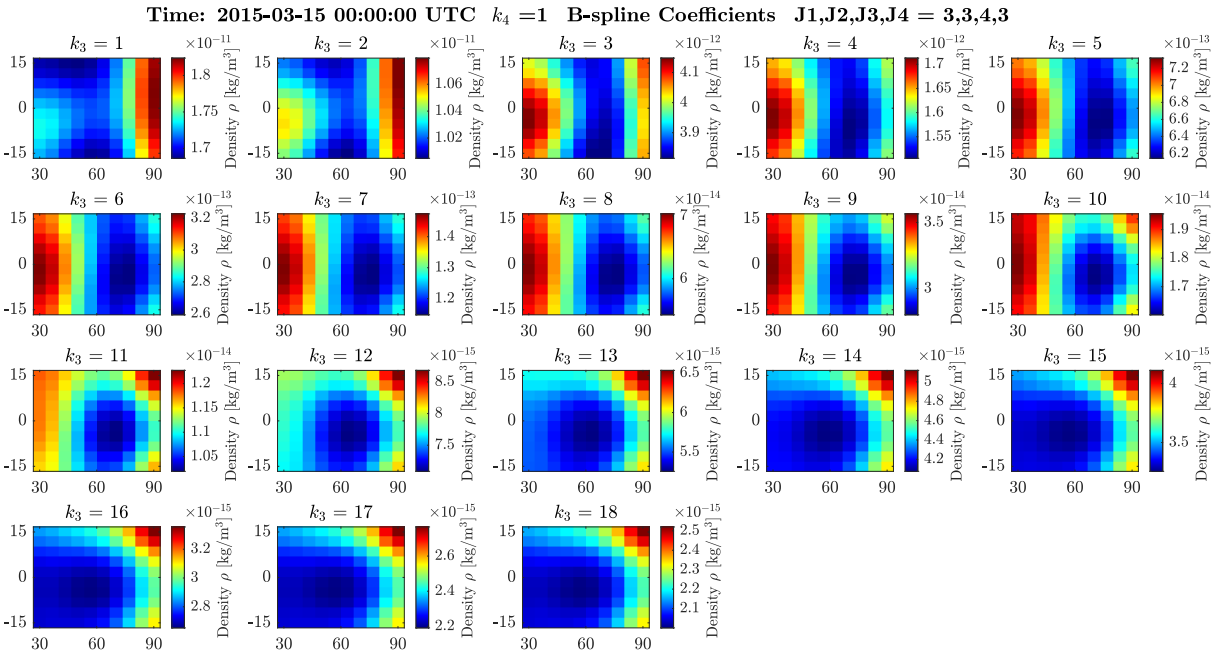

Figure 6.34: The regional maps presenting B-spline coefficients estimated from original neutral densities with resolution levels $J_1 = 3$, $J_2 = 3$, $J_3 = 4$, $J_4 = 3$ in latitude, longitude, height and time at 00:00:00 on 15/03/2015 in 4-D modeling.

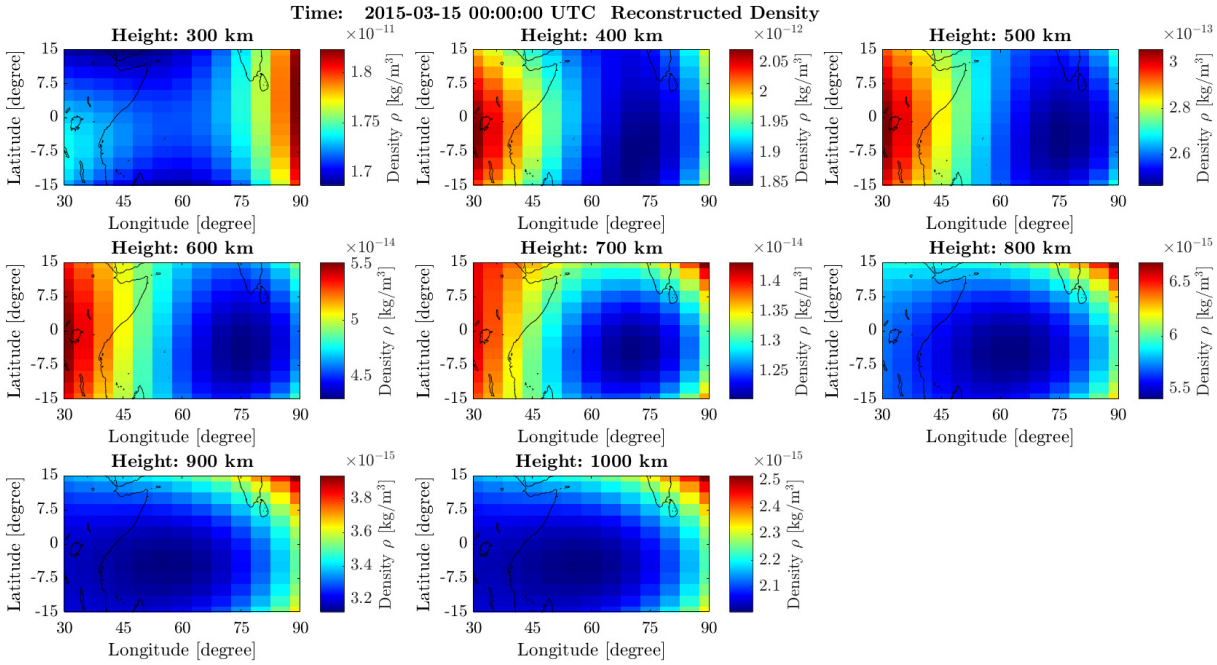

Figure 6.35: The regional map presenting neutral densities reconstructed from B-spline coefficients at 300-1000 km at 00:00:00 on 15/03/2015 in 4-D modeling.

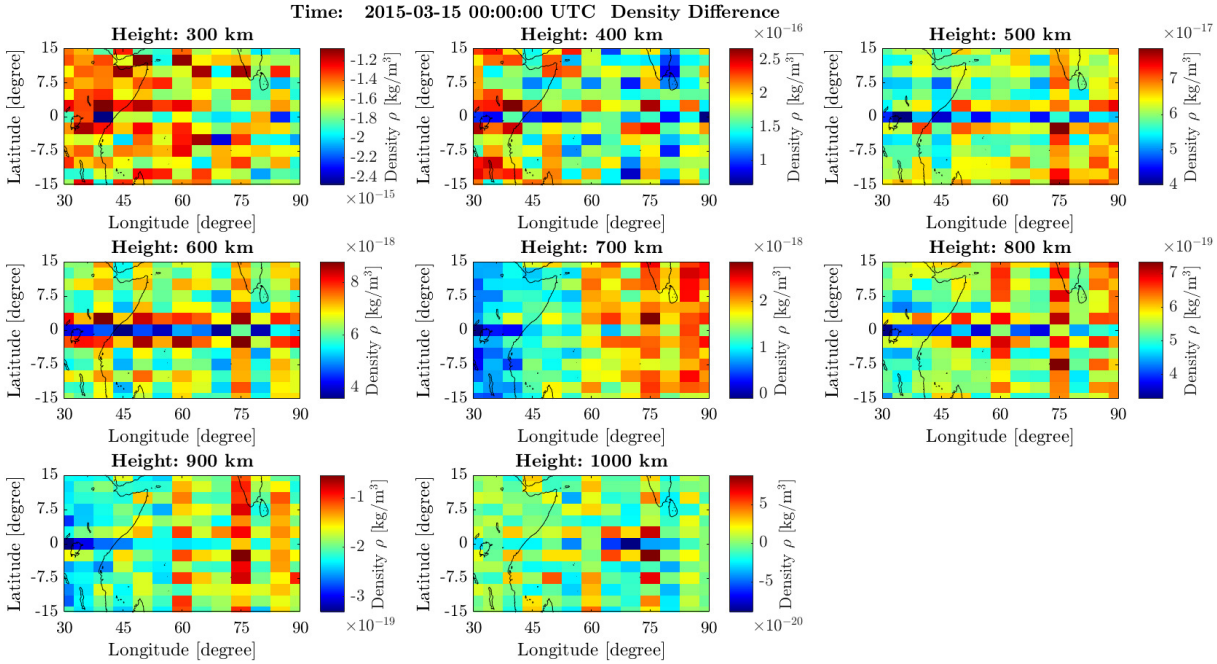

Figure 6.36: The regional maps presenting differences between neutral densities reconstructed from B-spline coefficients and original densities at 300-1000 km at 00:00:00 on 15/03/2015 in 4-D modeling.

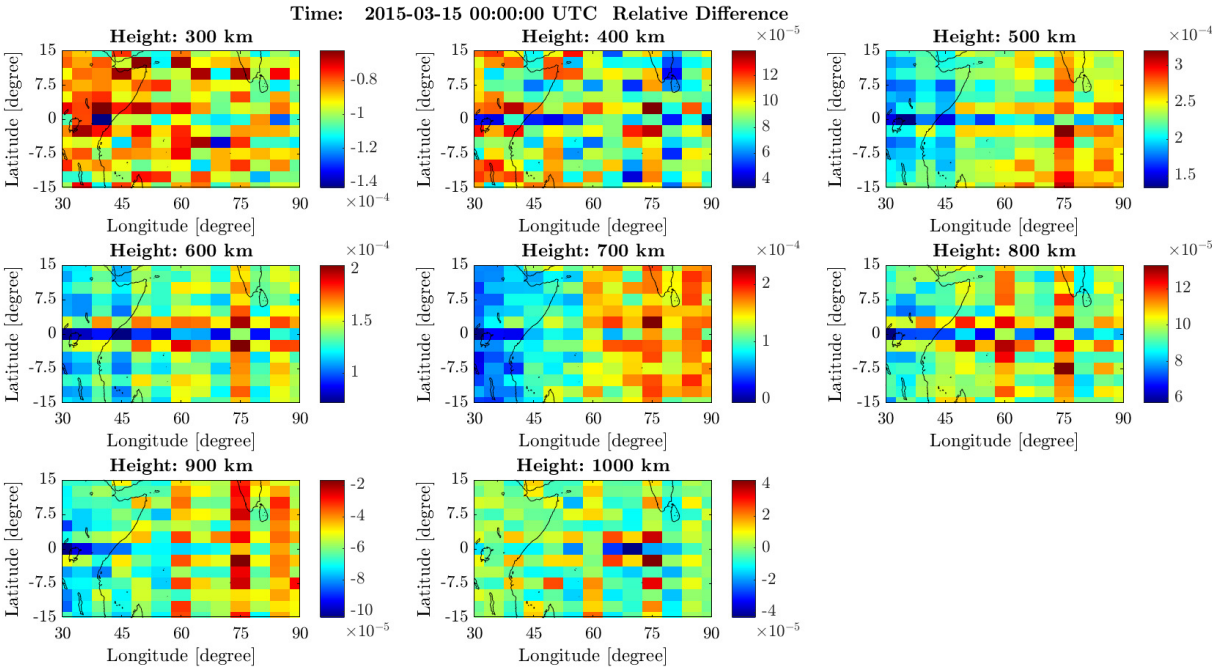

Figure 6.37: The regional maps presenting relative differences between neutral densities reconstructed from B-spline coefficients and original densities at 300-1000 km at 00:00:00 on 15/03/2015 in 4-D modeling.

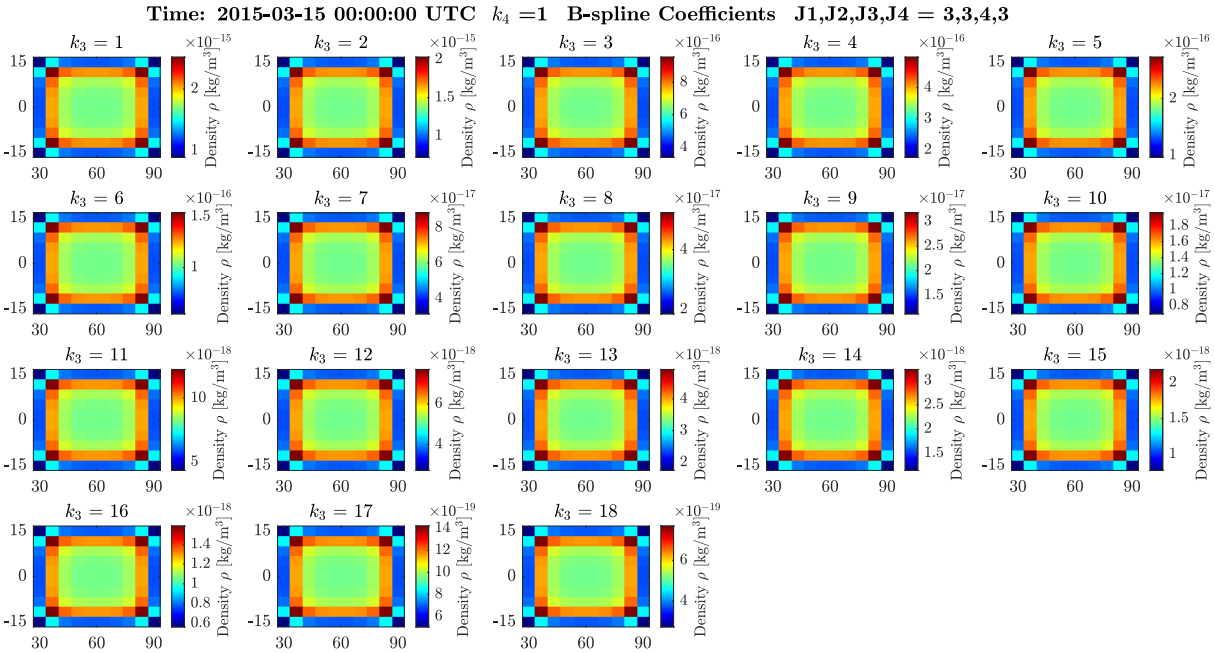

Figure 6.38: The regional maps presenting STDs of B-spline coefficients estimated from original neutral densities with resolution levels $J_1 = 3$, $J_2 = 3$, $J_3 = 4$, $J_4 = 3$ in latitude, longitude, height and time at 300-1000 km at 00:00:00 on 15/03/2015 in 4-D modeling.

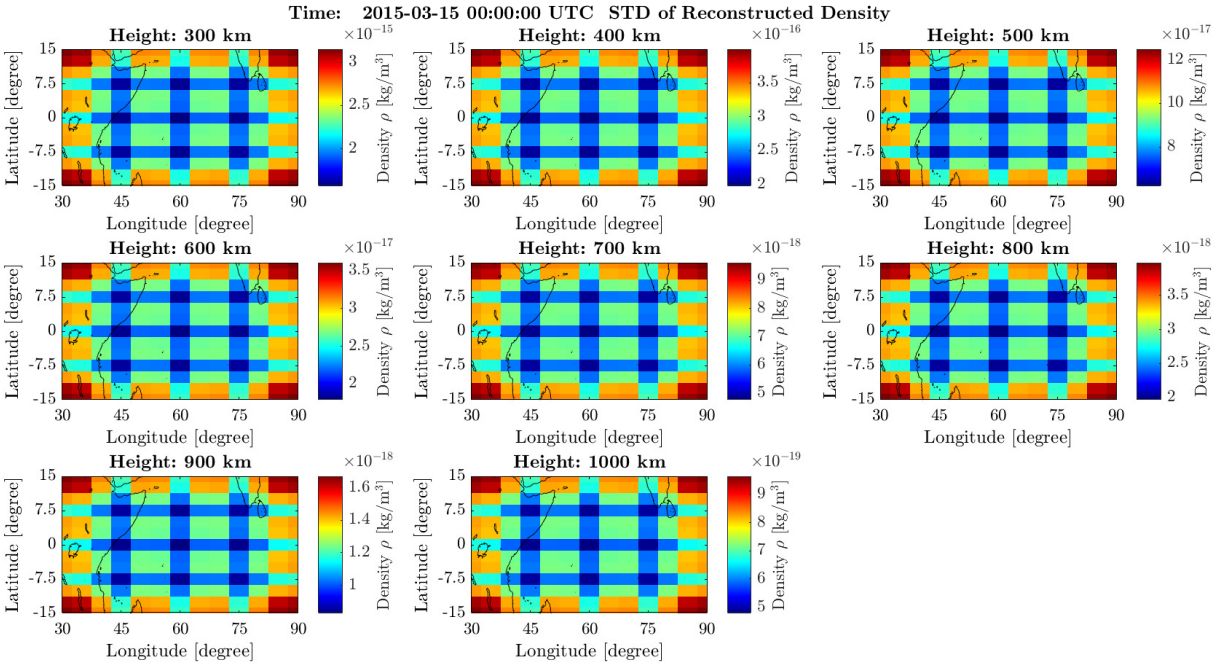

Figure 6.39: The regional maps presenting STDs of neutral densities reconstructed from B-spline coefficients at 300-1000 km at 00:00:00 on 15/03/2015 in 4-D modeling.

7 Conclusion and outlook

The precise modeling of the thermosphere is of great importance since the thermospheric drag depending on the neutral density is the main error source in the POD of LEO satellites. Usually, the thermospheric density is computed from empirical thermosphere models such as the NRLMSISE-00 model which, however, has limited accuracy. In order to improve the thermospheric density obtained from the empirical model and further improve the accuracy of POD for LEO satellites, new observations from geodetic tracking techniques such as SLR can be incorporated. In this process, the numerical integration of the satellite orbit is performed together with the estimation of a set of model parameters such as the time-dependent scale factors of the neutral density. In this study, the transformation of the thermospheric density with B-spline basis functions is applied because the B-spline coefficients are convenient to absorb new observations, and meanwhile, they can handle inhomogeneous data even with large gaps.

The characteristics of the empirical NRLMSISE-00 model are investigated firstly in the pre-analysis part. Starting from the determination of spatial resolution of thermospheric density grids, the derivation of the empirical model-based observations, the spectral content in the NRLMSISE-00 model is investigated by applying the CFT in the investigation period 23/11/2013 - 14/03/2016. It can be observed that the typical exponential decay appears along one single vertical profile of the thermospheric density grid. And the annual, semi-annual, daily and sub-daily periods are detected clearly in the time series of the neutral density.

In the next step, the artificially simulated data such as the constant signal, and the harmonic signal is generated for verifying the correctness and feasibility of algorithms related to B-spline representation by means of close-loop validation. Afterwards, the B-spline representation is applied to the thermosphere modeling within the context of 2-D, 3-D and 4-D. Importantly, the resolution levels of B-splines are chosen according to the characteristics of original observations and computational efficiency. Finally, the related products including B-spline coefficients and reconstructed thermospheric densities are generated, and the precision and accuracy of modeling results are evaluated based on the difference between estimated neutral densities and model-derived densities, and STD values of B-spline coefficients and reconstructed neutral densities.

The modeling results show, the use of the B-spline expansions achieves good performance in terms of thermosphere modeling. The relative difference of 10^{-3} for the estimated neutral densities is acquired in 2-D and 3-D representation. But the 3-D B-spline transformation outperforms the 2-D since the STD values of 3-D modeling are smaller than those of 2-D modeling by a factor of 2. With respect to the spatial distribution of STDs of B-spline coefficients and the estimated neutral densities, they are latitude-dependent and height-dependent with values decreasing from the polar region to the equator and from lower altitudes to high altitudes but always with values of 4-order smaller than the original observations. It is worth mentioning that the weighting matrix used in 3-D representation is on the basis of the result of 2-D representation due to the exponential distribution of the thermospheric density dependent on height. In principle, the results of 4-D modeling perform worse than those of 2-D and

3-D modeling due to the additional constraints in temporal dependency, which however is not shown in this thesis because only the regional modeling is performed within the context of 4-D.

In addition, one of the most important challenges in this study is the handling of height-dependent modeling due to its exponential decay in the vertical dimension, which is solved desirably, on one hand, by the serious choice of vertical sampling interval and the level of B-splines in height based on the pre-test of modeling the single vertical density profile, and on the other hand, by the introduction of the logarithmic model and appropriate weighting strategy dependent on the altitude.

In conclusion, the use of B-splines is a good choice to model the thermospheric density because the deviations of reconstructed neutral densities from original densities are small, and there are only random differences. The ability of B-spline modeling is determined by the resolution levels in different dimensions, hence, the higher levels, the lower differences. The estimated B-spline coefficients can be used to compute the neutral density at any geographical location. Besides, the compactly supported B-spline functions allow for the appropriate handling of the heterogeneous data distribution and the incorporation of new observations.

From the perspective of B-spline representation applied in thermosphere modeling, the 4-D experiment can be extended to the global case in the future. And the weighting strategy used in the least-squares adjustment can be considered probably in different ways. Furthermore, the spatial gaps can be added to the input observations in order to compare the performance of B-spline transformation starting with different input observations. Besides, the improvement of the neutral density computed from the empirical thermosphere model can be performed through the POD of LEO satellites by combining new information from geodetic observing techniques, while the B-spline coefficients provide good background information in this process. Additionally, the empirical thermosphere model NRLMSIS 2.0 can be considered the basic model to evaluate the performance of the new thermosphere model.

Bibliography

Bloßfeld, M. (2015). *The key role of Satellite Laser Ranging towards the integrated estimation of geometry, rotation and gravitational field of the Earth*. Dissertation, Technische Universität München, München.

Bowman, B., Marcos, F., Huang, C., Lin, C., and Burke, W. (2008). A new empirical thermospheric density model jb2008 using new solar and geomagnetic indices. *AIAA/AAS Astrodynamics Specialist Conference and Exhibit*.

Brouwer, D. (1937). On the accumulation of errors in numerical integration. *The Astronomical Journal*, 46:149–153.

Bruinsma, S. (2015). The DTM-2013 thermosphere model. *Journal of Space Weather and Space Climate*, 5:A1.

Butcher, J. C. (1996). A history of runge-kutta methods. *Applied numerical mathematics*, 20(3):247–260.

Dierckx, P. (1984). Algorithms for smoothing data on the sphere with tensor product splines. *Computing*, 32(4):319–342.

Doornbos, E. (2012). *Thermospheric density and wind determination from satellite dynamics*. Springer Science & Business Media.

Doornbos, E., Klinkrad, H., Scharroo, R., and Visser, P. (2007). Thermosphere density calibration in the orbit determination of ers-2 and envisat. In *Proceedings of envisat symposium, Montreux, ESA SP-636*. Citeseer.

Emmert, J. T., Drob, D. P., Picone, J. M., Siskind, D. E., Jones Jr, M., Mlynczak, M., Bernath, P., Chu, X., Doornbos, E., Funke, B., et al. (2021). Nrlmsis 2.0: A whole-atmosphere empirical model of temperature and neutral species densities. *Earth and Space Science*, 8(3):e2020EA001321.

Flanagan, H. P. (2015). *Improved Atmospheric Density Estimation for ANDE-2 Satellites using Drag Coefficients Obtained from Gas-Surface Interaction Equations*. PhD thesis, University of Kansas.

Fleming, E. L., Chandra, S., Barnett, J., and Corney, M. (1990). Zonal mean temperature, pressure, zonal wind and geopotential height as functions of latitude. *Advances in Space Research*, 10(12):11–59.

Goss, A., Schmidt, M., Erdogan, E., Görres, B., and Seitz, F. (2019). High-resolution vertical total electron content maps based on multi-scale b-spline representations. In *Annales geophysicae*, volume 37, pages 699–717. Copernicus GmbH.

Goss, A., Schmidt, M., Erdogan, E., and Seitz, F. (2020). Global and regional high-resolution vtec modelling using a two-step b-spline approach. *Remote Sensing*, 12(7):1198.

Hedin, A. E. (1987). Msis-86 thermospheric model. *Journal of Geophysical Research: Space Physics*, 92(A5):4649–4662.

Hedin, A. E. (1991). Extension of the msis thermosphere model into the middle and lower atmosphere. *Journal of Geophysical Research: Space Physics*, 96(A2):1159–1172.

Jekeli, C. (2005). Spline representations of functions on a sphere for geopotential modeling. Technical report, Ohio State University. Division of Geodetic Science.

Koch, K.-R. (1999). *Parameter estimation and hypothesis testing in linear models*. Springer Science & Business Media.

Liang, W. (2017). *A regional physics-motivated electron density model of the ionosphere*. PhD thesis, Technische Universität München.

Limberger, M. (2015). *Ionosphere modeling from GPS radio occultations and complementary data based on B-splines*. PhD thesis, Technische Universität München.

Lyche, T. and Schumaker, L. L. (2000). A multiresolution tensor spline method for fitting functions on the sphere. *SIAM Journal on Scientific Computing*, 22(2):724–746.

Meyling, R. G. and Pfluger, P. R. (1987). B-spline approximation of a closed surface. *IMA journal of numerical analysis*, 7(1):73–96.

Panzetta, F., Bloßfeld, M., Erdogan, E., Rudenko, S., Schmidt, M., and Müller, H. (2018). Towards thermospheric density estimation from slr observations of leo satellites: a case study with ande-pollux satellite. *Journal of Geodesy*, 93.

Picone, J., Hedin, A., Drob, D., and Aikin, A. (2002). Nrlmsise-00 empirical model of the atmosphere: Statistical comparison and scientific issues. *Journal of Geophysical Research*, 107.

Qian, L., Burns, A. G., Emery, B. A., Foster, B., Lu, G., Maute, A., Richmond, A. D., Roble, R. G., Solomon, S. C., and Wang, W. (2014). The ncar tie-gcm: A community model of the coupled thermosphere/ionosphere system. *Modeling the ionosphere–thermosphere system*, pages 73–83.

Rudenko, S., Schmidt, M., Bloßfeld, M., Xiong, C., and Lühr, H. (2018). Calibration of empirical models of thermospheric density using satellite laser ranging observations to near-earth orbiting spherical satellites. In *International symposium on advancing geodesy in a changing world*, pages 119–127. Springer.

Schmidt, M. (2007a). Wavelet modelling in support of iri. *Advances in Space Research*, 39(5):932–940.

Schmidt, M. (2007b). Wavelet modelling in support of iri. *Advances in Space Research*, 39(5):932–940.

Schmidt, M., Dettmering, D., Mößmer, M., Wang, Y., and Zhang, J. (2011). Comparison of spherical harmonic and b spline models for the vertical total electron content. *Radio Science*, 46(06):1–8.

Schmidt, M., Dettmering, D., and Seitz, F. (2015). *Using B-Spline Expansions for Ionosphere Modeling*, pages 939–983. Springer Berlin Heidelberg, Berlin, Heidelberg.

Schumaker, L. L. and Traas, C. (1991). Fitting scattered data on spherelike surfaces using tensor products of trigonometric and polynomial splines. *Numerische Mathematik*, 60(1):133–144.

Stollnitz, E., DeRose, A., and Salesin, D. (1995). Wavelets for computer graphics: a primer.1. *IEEE Computer Graphics and Applications*, 15(3):76–84.

Vallado, D. A. (2001). *Fundamentals of astrodynamics and applications*, volume 12. Springer Science & Business Media.

Walker, D. M. (1987). Non-gravitational perturbations and satellite geodesy: A. milani, a. m. nobili and p. farinella, adam hilger, bristol (1987). 125 pp. u.k. £20. *Planetary and Space Science*, 35(11):1475.

Wu, C.-C., Liou, K., Lepping, R. P., Hutting, L., Plunkett, S., Howard, R. A., and Socker, D. (2016). The first super geomagnetic storm of solar cycle 24:"the st. patrick's day event (17 march 2015)". *Earth, Planets and Space*, 68(1):1–12.

Xiong, C., Lühr, H., Schmidt, M., Bloßfeld, M., and Rudenko, S. (2018). An empirical model of the thermospheric mass density derived from champ satellite. In *Annales geophysicae*, volume 36, pages 1141–1152. Copernicus GmbH.

Zeilhofer, C. (2008). Multi-dimensional b-spline modeling of spatio-temporal ionospheric signals. *123, A, DGK, München*.

Zeitler, L., Corbin, A., Vielberg, K., Rudenko, S., Löcher, A., Bloßfeld, M., Schmidt, M., and Kusche, J. (2021). Scale factors of the thermospheric density: A comparison of satellite laser ranging and accelerometer solutions. *Journal of Geophysical Research: Space Physics*, 126(12):e2021JA029708.